
National Laser Users' Facility and External Users' Programs

Under the facility governance plan implemented in FY08 to formalize the scheduling of the Omega Laser Facility as a National Nuclear Security Administration (NNSA) User Facility, Omega Facility shots are allocated by campaign. The majority of the FY14 target shots were allocated to the Inertial Confinement Fusion (ICF) Campaign conducted by integrated teams from the national laboratories and LLE and the High-Energy-Density (HED) Campaigns conducted by teams led by scientists from the national laboratories.

The Fundamental Science Campaigns accounted for 26.9% of the shots taken in FY14. Nearly half of these were dedicated to university fundamental science under the National Laser Users' Facility (NLUF) Program, and the remaining shots were allotted to the Laboratory Basic Science (LBS) Program, comprising peer-reviewed fundamental science experiments conducted by the national laboratories and by LLE, including the Fusion Science Center (FSC).

The Omega Laser Facility is also used for several campaigns by teams from the Commissariat à l'Énergie atomique et aux énergies (CEA) of France and the Atomic Weapons Establishment (AWE) of the United Kingdom. These programs are conducted at the facility on the basis of special agreements put in place by DOE/NNSA and participating institutions.

The facility users during this year included 11 collaborative teams participating in the NLUF Program; 16 teams led by Lawrence Livermore National Laboratory (LLNL) and LLE scientists participating in the LBS Program; many collaborative teams from the national laboratories conducting ICF experiments; investigators from LLNL and Los Alamos National Laboratory (LANL) conducting experiments for high-energy-density-physics programs; and scientists and engineers from CEA.

In this section, we briefly review all the external user activity on OMEGA during FY14.

FY14 NLUF Program

FY14 was the second of a two-year period of performance for the NLUF projects approved for the FY13–FY14 funding and OMEGA shots. Eleven NLUF projects (see Table 140.V) were allotted Omega Laser Facility shot time and conducted a total of 265 target shots at the facility. This NLUF work is summarized in the following section.

In response to a DOE-issued solicitation in late FY14 for FY15–FY16 experiments, 23 proposals were received. The proposals were to be reviewed by a technical evaluation panel in October 2014 so that DOE may decide which proposals can be accepted and receive shots at the Omega Facility.

Study of Fast-Electron Transport into Imploded High-Density Plasmas Using Cu-Doped CD Shell Targets

Principal Investigators: F. N. Beg (University of California, San Diego) and M. S. Wei (General Atomics)

Co-investigators: R. B. Stephens (General Atomics); C. McGuffey, B. Qiao, and H. Sawada (University of California, San Diego); A. A. Solodov, W. Theobald, C. Stoeckl, J. A. Delettrez, R. Betti, F. J. Marshall, and C. Mileham (LLE); M. H. Key, P. K. Patel, and H. S. McLean (LLNL); T. Yabuuchi, T. Iwawaki, and H. Habara (ILE); and J. J. Santos and D. Batani (University of Bordeaux, France)

Lead Graduate Student: L. C. Jarrott (University of California, San Diego)

Understanding the generation of fast electrons inside the cone and its subsequent transport into hot dense plasmas is crucial to the success of the cone-guided fast-ignition (FI) scheme of inertial confinement fusion. In our prior work, we developed a new platform that measured, for the first time, the spatial map of fast-electron transport in the vicinity of the core of an imploded shell in joint OMEGA and OMEGA EP experiments. In this University of California San Diego (UCSD)-led NLUF project, we use the same platform to investigate several methods of improving coupling efficiency into an imploded CH/CD

Table 140.V: NLUF proposals approved for shots at the Omega Laser Facility for FY13–FY14.

Principal Investigator	Institution	Project Title
F. N. Beg	University of California, San Diego	Systematic Study of Fast-Electron Energy Deposition in Imploded Plasmas with Enhanced OMEGA EP Laser Contrast and Intensity
R. P. Drake	University of Michigan	Experimental Astrophysics on the OMEGA Laser
T. Duffy	Princeton University	Dynamic Compression of Earth and Planetary Materials Using OMEGA
W. Fox	University of New Hampshire	Dynamics and Instabilities of Magnetic Reconnection Current Sheets in High-Energy-Density Plasmas
P. Hartigan	Rice University	Astrophysical Dynamics in the Laboratory: Mach Stems and Magnetized Shocks
R. Jeanloz	University of California, Berkeley	Journey to the Center of Jupiter, Recreating Jupiter's Core on OMEGA
H. Ji	Princeton University	Study of Particle Acceleration and Fine-Scale Structures of Collisionless Magnetic Reconnection Driven by High-Energy Petawatt Lasers
R. D. Petrasso	Massachusetts Institute of Technology	Studies of Laboratory Astrophysics, Inertial Confinement Fusion, and High-Energy-Density Physics with Nuclear Diagnostics
B. Qiao	University of California, San Diego	Dynamics of High-Energy Proton Beam Focusing and Transition into Solid Targets of Different Materials
A. Spitkovsky	Princeton University	Generation of Collisionless Shocks in Laser-Produced Plasmas
R. B. Stephens	General Atomics	Investigation of the Dependence of Fast-Electron Generation and Transport on Laser Pulse Length and Plasma Materials

shell attached to a re-entrant gold cone target. The shell has an outer diameter of 870 μm , consisting of a 15- μm -thick outer CH ablator and a 23- μm -thick inner CD layer. *A Cu dopant (at ~1% atomic number density of CD) is added to the CD layer of the shell, which makes it possible to characterize fast-electron transport via its induced Cu K-shell fluorescence radiation.*

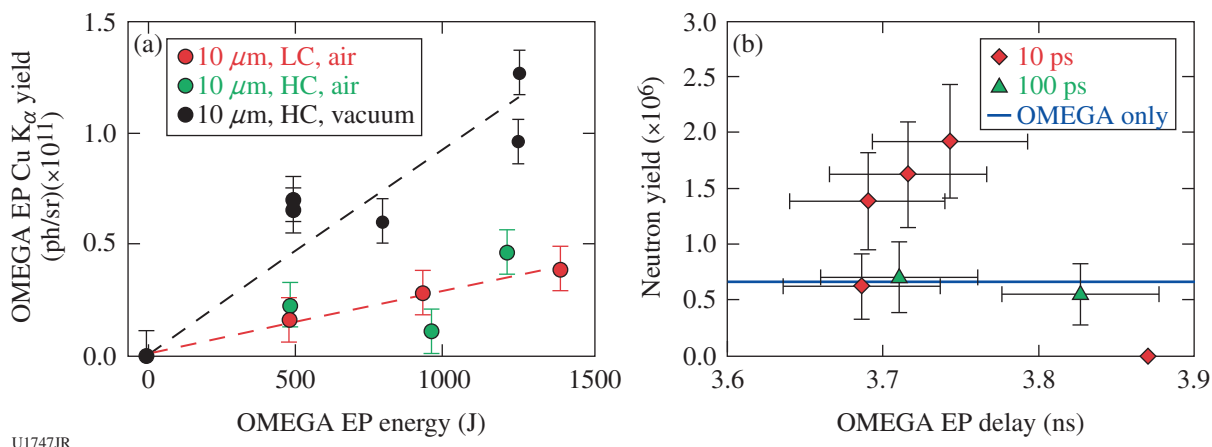
Fifty-four OMEGA beams (with a total energy of ~18 kJ) were used to compress the shell. The 10-ps OMEGA EP Beamline 2 was tightly focused at the inner cone tip with various time delays relative to the OMEGA driver chosen to be before and after breakout on the inner cone tip. In this experiment, air was evacuated from the shells and the driver pulse shape was modified because radiation–hydrodynamic simulations predicted increased density at the instant of cone-tip breakout.

The breakout timing was measured by the active shock breakout (ASBO) diagnostics for this new configuration. A zinc Von Hamos (ZVH) x-ray spectrometer tuned to measure the Cu K shell and ionic line emission provided spatially integrated Cu K_{α} yield measurements. As seen in Fig. 140.42, *the total Cu K_{α} yield increased significantly (up to a factor of 3.5) in the joint shots compared to the OMEGA-only implosion shots.* Fast-electron energy coupling to the compressed core was found to increase

with the OMEGA EP beam energy. Neutron yield from D–D fusion, measured by a liquid crystal neutron time-of-flight detector, was also found to increase with OMEGA EP energy by a factor of up to 2.9, compared to those from only the implosion.

While the ZVH provided the total yield of Cu K_{α} , a monochromatic spherical crystal imager (SCI) (centered at 8048 eV with a 6-eV bandwidth) gave unprecedented spatial information about where the fast electrons deposit their energy. Figures 140.43(a)–140.43(c) show data from joint shots at three delays. *They clearly show that fast electrons penetrated through the cone (wall and tip) into the compressed shell, producing strong Cu K_{α} emission from the region of the imploded high-density plasmas.* The brightness, characteristic shape, and size change as a function of delay. The spatially resolved SCI data indicate that nearly all of the enhancement in Cu K_{α} yield is a result of emission from within 150 μm of the cone tip's position.

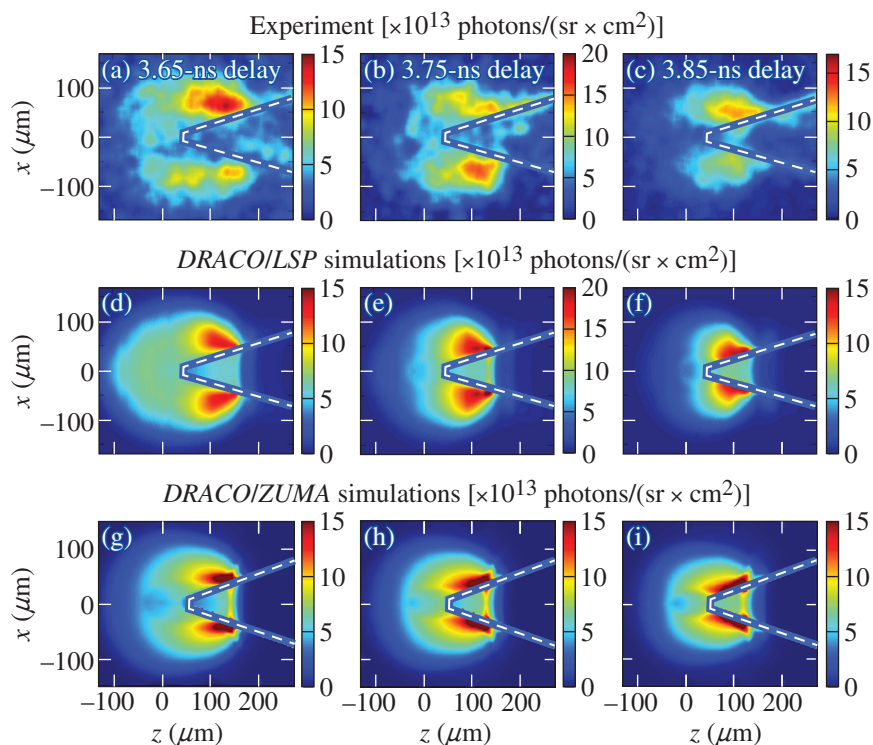
A comprehensive hierarchy of simulation tools was used to model the entire process from the implosion (2-D radiation–hydrodynamics code *DRACO*), cone pre-plasma (2-D radiation–hydrodynamics code *HYDRA*), electron generation, and finally, electron-beam transport particle-in-cell (PIC) code *LSP*. Diagnostic capabilities were implemented into the final transport steps



U1747JR

Figure 140.42

(a) Cu K_{α} yield from the zinc Von Hamos (ZVH) spectrometer showed enhancement with OMEGA EP in all three configurations investigated. The cone tip's diameter was either 10 or 40 μm , the OMEGA EP contrast was high (HC) or low (LC, prior to upgrade), and the shells had residual air or were evacuated with corresponding reduced driver picket. (b) D–D neutron yield was enhanced with the high-contrast, high-intensity (10-ps) OMEGA EP in joint shots prior to tip breakout.



U1748JR

Figure 140.43

[(a)–(c)] Cu K_{α} images showing the emission from the vicinity of the cone tip at various delays with the OMEGA EP beam energy at ~ 500 J. The dotted line is added to visualize the cone position. [(d)–(f)] Simulated data using a series of codes reproduce the emission around and in front of the cone tip at the same delays. [(g)–(i)] Simulated data with the hybrid particle-in-cell (PIC) code *ZUMA* allowed for comparison to data over a wide range of source position, divergence, and energy.

to emulate the generation of Cu K_{α} photons, taking into account temperature effects on emission and crystal response caused by the shifting and broadening of the Cu K_{α} spectral line at plasma temperatures increasing above the order of 150 eV (using the code *PrismSPECT3D*), opacity, and 2-D projection for direct comparison to the experimental images. Figures 140.43(d)–140.43(f) show simulated data at the same three delays, reproducing several of the features as functions of time, including decrease in size, close-

ness to the walls, and decreased signal in the forward direction because of heating. Transport studies were also carried out with the hybrid PIC code *ZUMA* for rapid comparison over a wide range of electron source parameters. These simulations were also able to reproduce the characteristics of the SCI data, as shown in Figs. 140.43(g)–140.43(i), and further identified the parameters that were most important in determining the energy-deposition spatial profile and total coupling.

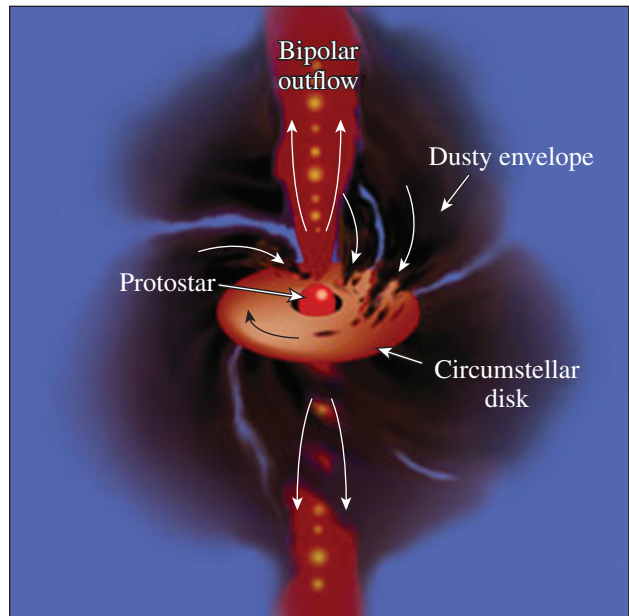
In summary, the FY14 UCSD-led NLUF fast-electron transport experiment used the cone-in-Cu-doped-shell platform developed previously to investigate two methods for improving the coupling from OMEGA EP to an imploded core: mitigation of pre-plasma in the cone by increasing the cone tip's diameter and optimization of the implosion. The changes led to Cu K_{α} yield enhancement by as much as a factor of 3.5. The increased yield from the core region along with the enhanced neutron yield gives two independent figures of merit showing increased energy coupling to the high-density core. This platform identified the crucial parameters to the coupling of energy to the core, and the data validated modeling codes and tests of new target designs so that coupling to the core can be improved—a critical step forward in the evaluation of fast-ignition laser fusion.

Laboratory Astrophysics Investigation into the Structure of Accretion Shocks

Principal Investigator/Project Director and Technical Point of Contact: Professor R. P. Drake
 Co-Principal Investigator: C. C. Kuranz (University of Michigan)
 Co-investigators: S. Ross (LLNL); C. K. Li and A. Zylstra (MIT); S. Klein and M. Trantham (University of Michigan); and D. H. Froula, G. Fiksel, and P.-Y. Chang (LLE)

This work involves the design and implementation of laboratory astrophysics experiments on OMEGA to study accretion shocks at the surface of young stars. In the current model of accretion, material from the accretion disk surrounding the young star funnels to the stellar surface along magnetic-field lines (see Fig. 140.44). By understanding the structure of these accretion shocks, we hope to give astronomers the tools to better calculate accretion rates and, thereby, develop better models for the evolution of young stars—much like the Sun some five billion years ago.

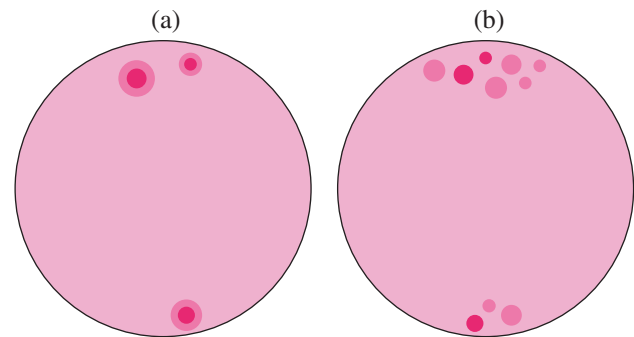
Since the material is supersonic, it creates a shock and a region of heated plasma when it hits the stellar surface. By studying the spectra of young stars, astronomers can tell that a small fraction (on average 1%) is covered by very hot plasma (roughly 3 MK) and a slightly larger fraction (on average 5%) is covered by less hot plasma (roughly 2 MK). But what do these fractions tell us about the accretion process? Are the 3-MK hot spots and the 2-MK hot spots caused by independent accretion streams with different densities or are the 2-MK hot spots just heated regions surrounding the 3-MK hot spots? Figure 140.45 illustrates the dilemma. By understanding the structure of accretion shocks, we hope to determine which of these scenarios is more likely and, thereby, enable astronomers to make more-accurate studies of accretion rates.



U1750JR

Figure 140.44

A diagram of an accreting protostar system. The protostar is surrounded by an active accretion disk and the star-disk system generates bipolar outflows. There is a gap between the inner edge of the disk and the surface of the star; material bridges this gap by flowing along magnetic-field lines. Credit: Thomas Greene, American Scientist, July–August (2001).

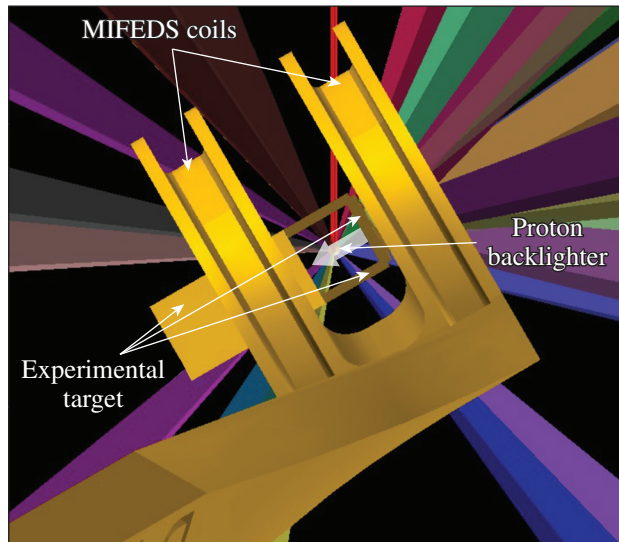


U1751JR

Figure 140.45

(a) Is the 2-MK plasma (shown in medium pink) associated with the 3-MK plasma (shown in dark pink) or (b) are the 2-MK and 3-MK hot spots independent? Understanding which of these scenarios applies has implications when trying to calculate an accretion rate.

Our experiment involves creating a plasma flow by rear-irradiating a thin acrylic cone with seven OMEGA full-power beams (see Fig. 140.46). This plasma (the “accreting flow”) travels roughly 3 mm and impacts a solid block (the “stellar surface”). We impose a magnetic field parallel to the plasma flow with a magneto-inertial fusion electrical discharge system (MIFEDS)



U1752JR

Figure 140.46

The experimental target has three pieces: a magneto-inertial fusion electrical discharge system (MIFEDS) structure, which imposes a magnetic field on the experiment; an experimental target, which is aligned inside the MIFEDS structure; and a proton backlighting capsule. For reference, the experimental target is 3 mm × 3 mm × 8 mm.

device and image the experiment with proton radiography to capture the magnetic distortion caused by the impact.

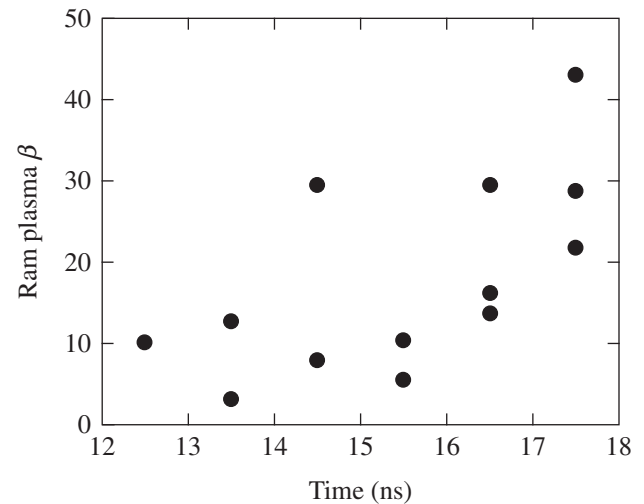
Previous experience with plasma jets generated in this fashion demonstrates that we have plasma $\beta \approx 5$ to 50, where β is the ratio of ram pressure to magnetic pressure. This is similar (to an order of magnitude) to the plasma β present on young stars with low magnetic fields. Figure 140.47 shows plasma β versus time for a magnetic field of 7 T and plasma parameters from Thomson-scattering data from five shots in April 2012.

Structure of Molybdenum and Iron Oxide Under Dynamic Compression on OMEGA

Principal Investigator: T. Duffy (Princeton)

Co-investigators: R. Smith and F. Coppari (LLNL); J. Wang and J. Wicks (Princeton); and T. R. Boehley (LLE)

During FY14, we carried out a series of experiments as part of our long-term effort to constrain the structure and properties of key materials of interest in geophysics and high-pressure science. This year we focused on molybdenum (Mo), a high-pressure standard material, and iron oxide, a key constituent of the deep mantle and core of terrestrial planets. The OMEGA laser was used to ramp or shock compress these materials to as high as 1 TPa of pressure, and the powder x-ray diffraction image plate (PXRDIP) diagnostic was used to record x-ray diffraction patterns. Active shock breakout



U1753JR

Figure 140.47

The plasma β (ratio of ram pressure to magnetic pressure) for jets made by the method employed for Fig. 140.46. These data are from OMEGA shots in April 2012.

(ASBO) was used to measure free surface and interface velocities from which pressure in the sample could be determined.

Molybdenum is an important body-centered-cubic (bcc) transition metal that has been extensively studied at high pressure but significant unanswered questions and discrepancies remain. The nature of the stable phase along the Hugoniot above 210 GPa is uncertain. There is also a large discrepancy between static and shock-wave experiments and theoretical calculations regarding the pressure at which Mo melts on the Hugoniot and the slope of the melting curve with pressure. In our experiments, Mo was shock compressed between 250 and 450 GPa. Between 250 to 380 GPa, we observed a diffraction peak consistent with the strong (110) reflection of bcc molybdenum. Other possible phases, such as the hexagonal-close-packed and face-centered-cubic structures, are not consistent with the observed diffraction pattern. Our results agree well with the most-recent sound velocity measurements and theoretical calculations for Mo and enable us to rule out a phase transition at 210 GPa. At 390 GPa, the diffraction pattern changes, with the strong, textured (110) peak replaced by a weak, untextured broad feature. This is consistent with partial melting of Mo beginning near 390 GPa. Our melting results are in agreement with theoretical calculations and demonstrate that the melting temperature of Mo increases strongly with pressure. This work shows that direct structural determinations by x-ray diffraction on dynamically compressed materials on OMEGA can provide key insights into material behavior along the Hugoniot.

Iron oxide (FeO) is an important material for modeling Earth and planetary interiors. Understanding its properties and measuring its equation of states at multi-megabar pressures are crucial to building reliable geophysical models. FeO shows a complex polymorphism below 200 GPa, and experimental data on its structure and density exist only up to 300 GPa. In our experimental campaigns on OMEGA, we ramp-compressed FeO from 350 to 750 GPa and measured the high-pressure polymorph in a totally unexplored pressure regime. The d spacings reported in Fig. 140.48 as a function of pressure show that the stable structure in this pressure regime is the B2 phase, which has never been measured experimentally to such a high pressure. These data will allow us to experimentally determine the stress–density relation for B2–FeO and its equation of state and will provide an experimental benchmark to theoretical simulations.

Dynamics of Magnetic-Reconnection Current Sheet in High-Energy-Density Plasmas

Principal Investigator: W. Fox and A. Bhattacharjee (Princeton, Plasma Physics Laboratory)

Co-investigators: G. Fiksel, P. M. Nilson, S. X. Hu, and D. Haberberger (LLE)

We have developed and conducted experiments on OMEGA EP to study the phenomenon of magnetic reconnection. Magnetic reconnection occurs when regions of opposite directed magnetic fields in a plasma can interact and relax to a

lower-energy state; it is an essential plasma physics process in many systems that governs the storage and explosive release of magnetic energy in systems such as the earth's magnetosphere, the solar corona, and magnetic-fusion devices. The energy liberated in this way can produce heat flows and enable the acceleration of a large number of particles to high energies.

These experiments on OMEGA EP used an externally applied magnetic field of the order of 12 T as the seed field for reconnection. With an externally applied field, the fields undergoing reconnection are under experimental control, so it is possible to conduct experiments with variable fields and topologies. In our first experiment, we conducted the “zero-field” case, in which the plumes can interpenetrate and drive the Weibel instability,¹ which is also very interesting as a mechanism to produce unmagnetized shocks in astrophysical blast waves.

We have now also successfully *magnetized* and collided the counterpropagating plasmas and observed reconnection of the fields as the plumes collided.² Figures 140.49(a)–140.49(d) shows a sequence of proton radiography images of the collision and interaction of the magnetized plasmas. The results are qualitatively different than the unmagnetized case and show the formation of a pair of magnetized “ribbons” propagating toward one another. These ribbons are regions of a deficit of protons to the film and indicate regions of strong magnetic field—magnetized plasma—which has steered the

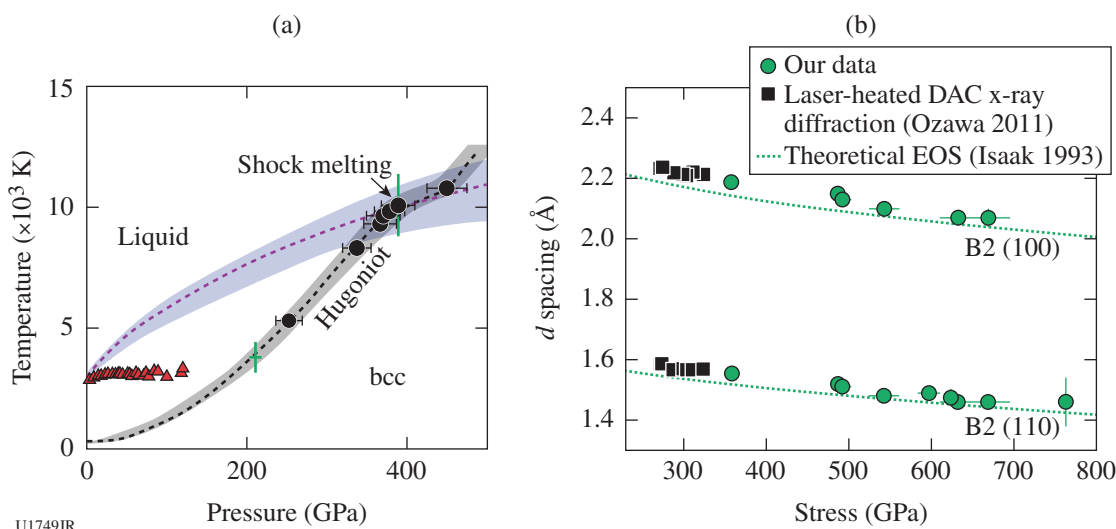
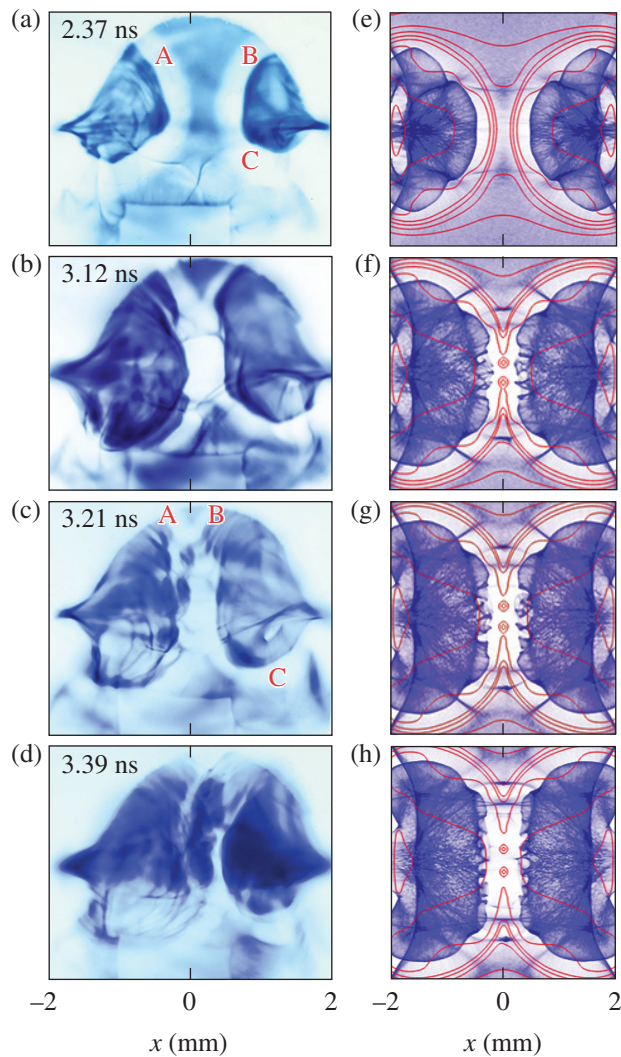


Figure 140.48

(a) Phase diagram of molybdenum (Mo). Black circles represent our experimentally measured shock pressures. The black and purple dashed lines show the calculated Hugoniot temperatures and melting curve for Mo. Our results are consistent with theoretical calculations that melting begins on the Hugoniot near 390 GPa and require a steeper melting curve than suggested from diamond anvil cell (DAC) data (red triangles). (b) Experimentally determined d spacings for FeO as a function of pressure as obtained in our ramp-compression experiments. Green circles represent our data, which are compared with static compression experiments (black squares) and theoretical simulations (green dotted lines). Our data show that the B2 phase of FeO is stable at least up to 750 GPa.

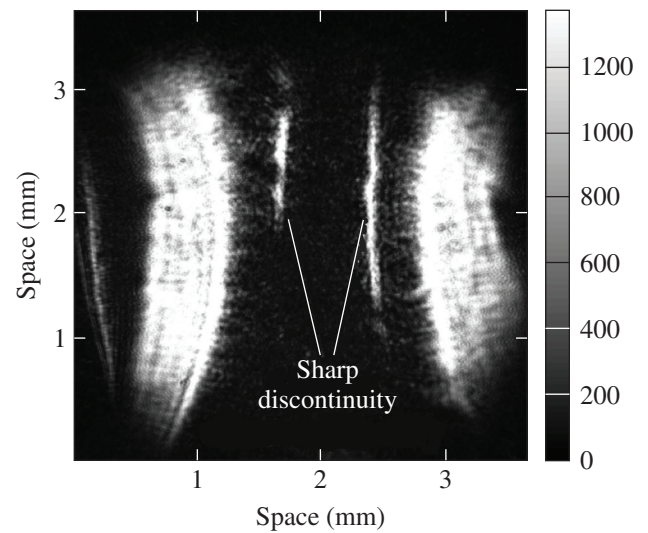


E23014JR

Figure 140.49 Proton radiography data and associated particle-in-cell simulations post-processed with a virtual proton radiography diagnostic for comparison. The white areas [(e)–(h)] indicate regions of strong magnetic fields (~30 T). As the two plumes expand and collide, the magnetic fields are brought together and reconnect. (From Ref. 1.)

diagnostic proton beam off-film. The successful formation of these pairs of ribbons is non-trivial: it was found that it was essential to add a third, “background” plasma source, triggered before the blowoff forms the two primary targets, to fill the experimental volume with a diffuse low-density plasma. In Fig. 140.49 a sequence of images from both the experiments and associated particle-in-cell simulations show the ribbons propagating toward one another and colliding at the midplane, generating bubble-like structures as the regions of oppositely magnetized plasmas interact and drive the reconnection of the magnetic fields.

Finally, in our most-recent results, we added the angular filter refractometry (AFR) diagnostic based on the new fourth-harmonic optical probe beam on OMEGA EP. This diagnostic measures density structures; in particular, transition bands occur in the image at specific values of the plasma density gradients (see Fig. 140.50 for an example). We are presently working to unfold these measurements to provide the plasma density in the reconnection region. Additionally, we observe very narrow AFR features that indicate steep density jumps at the edges of the plumes, coincident with where the magnetic fields are compressing, likely indicating formation of a shock. Similar features in the magnetic fields and density gradients are observed in our particle-in-cell simulations; we are investigating the specific mechanisms for shock formation.



U1756JR

Figure 140.50 Angular filter refractometry image of two colliding magnetized plumes. The transition bands correspond to specific values of the plasma density gradient. A sharp density jump is formed at the edge of the plumes and coincident with the magnetic-field ribbons.

Astrophysical Dynamics in the Laboratory: Mach Stems and Magnetized Shock Waves

Principal Investigator: P. Hartigan (Rice University)
 Co-investigators: J. Foster and P. Rosen (AWE); C. Kuranz (University of Michigan); G. Fiksel (LLE); A. Frank (University of Rochester); B. Blue (General Atomics); A. Liao (Rice University); and P. Graham (AWE)

Supersonic flows are associated with a wide variety of astrophysical phenomena, including stellar winds, jets from young stars and black holes, and interacting binary systems; they are pervasive throughout both the interstellar and intergalactic

media. All of these types of objects have magnetic fields of sufficient strength to affect how the systems evolve dynamically. In the past year we have been using the MIFEDS system on OMEGA to explore different experimental designs with the goal of creating a platform that we can use to study strongly magnetized, high-Mach-number shock waves in a controlled laboratory environment.

While highly magnetized plasmas are the norm in most astrophysical contexts, the densities in the laboratory are much larger, so that when magnetic fields are compressed by strong shock fronts, the fields tend to diffuse out of the compressed material, which limits the effects that fields have on the flow dynamics. This problem can be particularly acute when magnetic fields are applied externally, for example, through the application of Helmholtz coils. One way to eliminate the problem of magnetic diffusion is simply to drive a supersonic flow into a wire that carries a strong current. With this type of setup, the current in the wire continues to generate the field, which can then be compressed by the supersonic flow.

Numerical simulations of this configuration are shown in Fig. 140.51. Using the MIFEDS coils on OMEGA, we are able to achieve a magnetic-field strength of ~ 20 T at the surface of the wire. The importance of this field dynamically is determined by the parameter σ , which is the ratio of the ram pressure ρv^2 to the magnetic pressure $B^2/8\pi$. The simulations [Fig. 140.51(a)] show that the magnetic case should create a well-known morphology of a bow shock, where incident material is decelerated, and a mag-

netopause that defines the boundary of the compressed magnetic field around the wire. A plot [Fig. 140.51(b)] of the equilibrium position of the bow shock and magnetopause reveals that even when σ is as large as ~ 50 , the position of the bow shock in the magnetized case should be displaced by a measureable offset ($\sim 30 \mu\text{m}$) compared with the nonmagnetic case.

Our first laser shots using this configuration were completed in mid-October 2014. In Fig. 140.52 we show the magnetic images (green) superposed upon the nonmagnetic ones (red). A clear offset exists between the bow shock in the two cases, in the sense that the magnetic field from the wire maintains the bow shock at a larger distance from the wire surface. We have also obtained streaked optical pyrometer data for each shot and will be analyzing these to better quantify how the velocities varied in the experiment. This work shows great promise for producing a platform with which we will be able to study supersonic magnetic phenomena.

Journey to the Center of Jupiter, Recreating Jupiter's Core on OMEGA

Principal Investigator: R. Jeanloz (University of California, Berkeley)

Co-investigators: M. Millot (LLNL); and P. Loubeyre and S. Brygoo (CEA)

Our experimental documentation of He/H₂ phase separation, the insulator-metal transition in the vicinity of the predicted plasma phase transition (PPT), and the transport of dense hydrogen is significantly different from predictions by

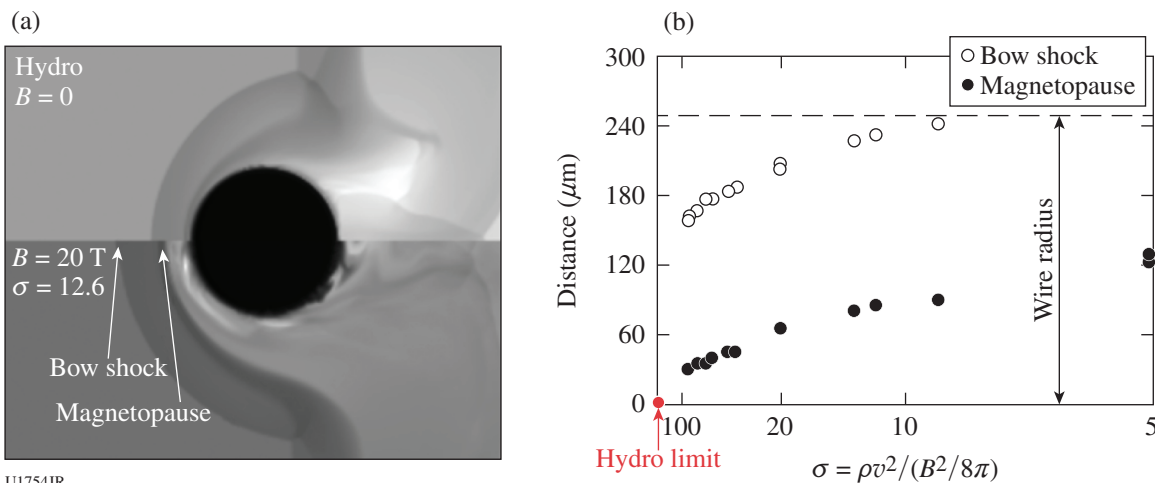


Figure 140.51 Numerical simulations of a supersonic flow moving past a current-carrying wire. (a) The flow is incident from the left and produces a bow shock and a magnetopause in the magnetic case (bottom half) as compared with the nonmagnetic case (top half). (b) Predicted offset of the bow shock (open circles) and magnetopause (solid circles) relative to the wire plotted as a function of the ratio σ of the ram pressure and magnetic pressure at the wire surface. Even a relatively small field produces a measureable magnetosphere.³

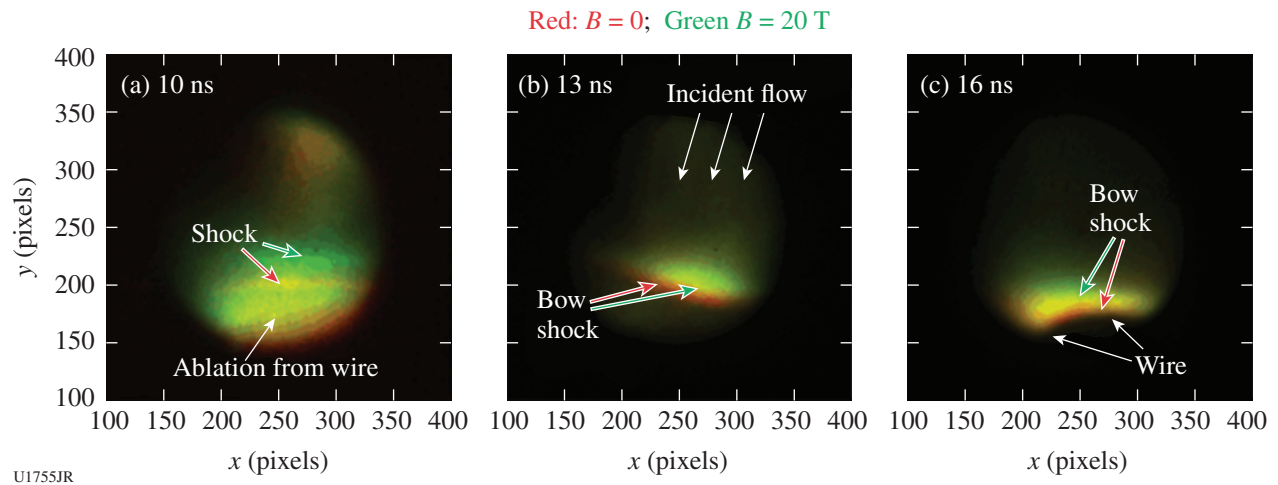


Figure 140.52

Optical images of the bow shock that forms around a wire. Left to right shows a time sequence of images as the flow moves from the top of the frame past the wire at the bottom. At early times there is significant ablation from the wire in response to irradiation from the laser drive. The color offset between the red and green shocks clearly demonstrates the effect of the magnetic field.

first-principles calculations. It also reveals the rich quantum nature of hydrogen up to tenfold compression and provides thermodynamic constraints on the hydrogen phase diagram that is otherwise based mainly on theory.

A few years ago, we launched a new capability to explore H_2 , He, and H_2/He mixtures at the Omega Laser Facility. The first step of our work was used to benchmark new techniques; produce new data to test structure and evolution models for Saturn and Jupiter; and extend the Hugoniot of hydrogen, deuterium, and helium as determined by several groups on different platforms: gas gun, Z, and lasers. Using diamond-anvil high-pressure cells (at room temperature) to tune the initial density of hydrogen to that of a cryogenic liquid, we established these techniques by comparing to previous data and validated our sample metrology, Hugoniot, reflectivity, and temperature measurements. The second step has been to significantly extend the Hugoniot, temperature, and transport measurements off the principal Hugoniot by changing the precompression of the sample.

We have now collected shock data with precompressed samples at initial pressures in the range 0.15 GPa to 9 GPa, (0.7 to $4\times$ the cryogenic fluid density), giving access to a broad new range of warm-dense-matter conditions for hydrogen and helium systems (Fig. 140.53). This led to several significant discoveries: (a) the maximum compression of the Hugoniot depends strongly on initial density, which provides a stringent test of existing equation-of-state models, and allows for the determination of several derivatives such as the specific heat, Grüneisen coefficient, adiabatic exponent, thermal coefficient

of expansion, etc.;⁴ (b) the reflectivity of hydrogen changes abruptly in the vicinity of the predicted plasma phase transition, with this transition from electrically insulating to conducting states appearing related to the recently observed maximum in the melting curve; and (c) the electrical conductivity of hydrogen deduced from reflectivity data differs from values predicted with current models at the highest densities examined.

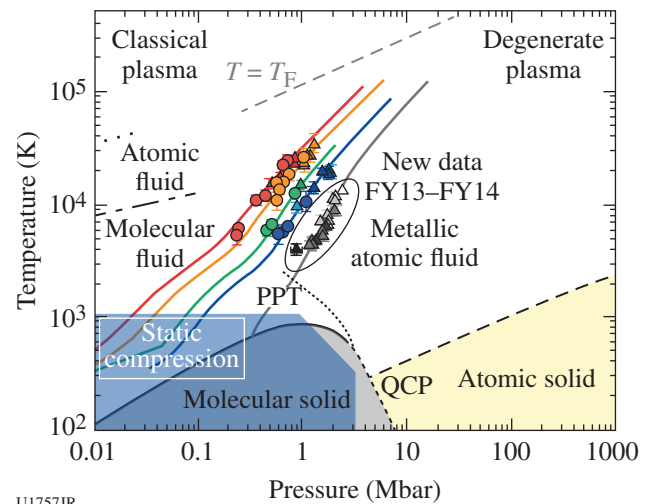


Figure 140.53

Pressure-temperature phase diagram of hydrogen with new data (gray and black symbols) at 6-GPa precompression together with lower precompression data (symbols) and predictions from density functional molecular dynamics (DFT-MD) numerical simulations. New data at 9-GPa precompression are being analyzed (not shown). PPT: plasma phase transition; QCP: quantum critical point.

Magnetic-Reconnection Experiments in Laser-Driven, High-Energy-Density Plasmas

Principal Investigator: H. Ji (Princeton)

In FY14, the team led by Princeton University carried out experiments on magnetically driven reconnection in laser-driven high-energy-density (HED) plasmas using a novel magnetic-field-generation technique. A schematic of the experimental setup on OMEGA EP is shown in Fig. 140.54. The main interaction target is comprised of two parallel copper plates, connected with two copper wires. Two OMEGA EP 2.5-kJ, 1-ns laser pulses pass through the laser entrance holes on the front plate and are focused on the back foil, generating a beam of superthermal hot electrons. The hot electrons stream onto the front plate and build up an electrical potential between the plates. This, in turn, drives large currents in both wires and creates magnetic reconnection because anti-parallel magnetic-field lines exist in the middle plane. Ultrafast proton radiography was utilized to probe the reconnection process at various times with high spatial and temporal resolutions. To characterize the magnetic-field generation around the wire, targets with double plates connected with a single wire were also used.

The experiments successfully demonstrate a large external field source on OMEGA EP and provide a solid platform toward

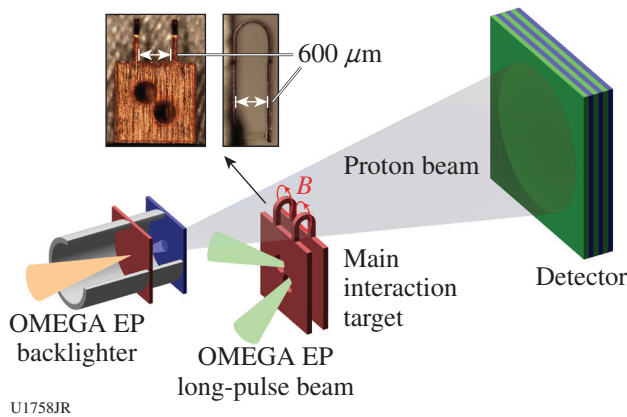


Figure 140.54 Experimental setup for the recent reconnection experiments on OMEGA EP based on a novel field-generation technique. The main target is comprised of two copper plates connected with two wires. Target parameters are well characterized before the experiment. Two OMEGA EP long-pulse beams pass through the holes on the first plate to reach the second plate, where hot electrons are released to charge up the first plate and form electric currents through the coils. Energetic protons generated by the OMEGA EP short-pulse beam are used to probe the reconnection process.

realizing magnetic reconnection in magnetically driven HED systems. Figure 140.55 shows the experimental results. Figure 140.55(a) is an example proton image for the single-wire case, taken at $t = t_0 + 3.101$ ns for 20-MeV protons, where t_0 is the arrival time of the long-pulse drive beams at the copper foil surface. The image is high quality, showing the location of the copper plate and the wire. In particular, a light bubble is formed when incident protons are deflected by the azimuthal magnetic field around the wire. The results show ~ 500 -T magnetic fields at a distance of $40 \mu\text{m}$ from the wire surface. Energetically, the generated magnetic energy by the coil is of the order of 1% of the total energy of two incidental lasers. Figure 140.55(b) shows an example proton image for the two-wire case, taken at $t = t_0 + 4.088$ ns for 20-MeV protons. Besides the features of copper plate and copper wire, two light bubbles and a jet-like feature in the center are observed. Detailed analysis on the cause of the jet is underway.

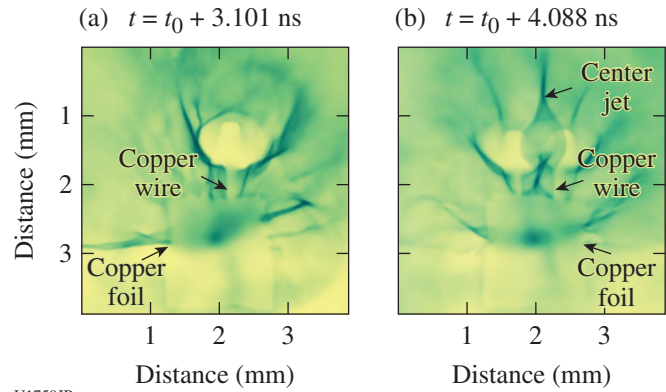


Figure 140.55 (a) A proton radiograph of a single-wire case where the light bubble is caused by magnetic fields around the wire deflecting incident protons. (b) A proton image for the two-wire case.

Studies of High-Energy-Density Plasmas, Inertial Confinement Fusion Implosions, and Nuclear Science for Astrophysics

Principal Investigators: R. D. Petrasso and C. K. Li (MIT)
 Co-investigators: F. H. Séguin, J. A. Frenje, and M. Gatu Johnson (MIT); T. C. Sangster, V. Yu. Glebov, D. D. Meyerhofer, and R. Betti (LLE); and O. L. Landen (LLNL)

MIT work in FY14 included a wide range of experiments applying proton radiography, charged-particle spectrometry, and neutron-spectrometry methods developed by MIT and collaborators to the study of high-energy-density physics (HEDP) and inertial confinement fusion (ICF) plasmas. In FY14 eight papers,^{5–12} one MIT Ph.D. thesis,¹³ one MIT M.Sc. thesis,¹⁴

and one MIT senior thesis¹⁵ about NLUF-related research were published; there were also many invited and contributed talks presented at conferences. Two additional papers have been submitted for publication.^{16,17} The students also won numerous awards, including the 2014 *Marshall N. Rosenbluth Outstanding Doctoral Thesis Award*, given to Dr. M. Manuel for NLUF work.^{18–20} This award has never before been given for HEDP research. In addition, recent Ph.D. M. Rosenberg has accepted a position at LLE.

Among recent publications are two *Physical Review Letters*^{5,6} by MIT students who presented analyses of OMEGA data, shedding new light on the important topic of kinetic/multi-ion effects in plasmas. Most ICF simulations are carried out with single average-ion, radiation–hydrodynamic codes, but we now know that deviations from hydrodynamic conditions are prevalent during the early stages of implosions when strongly shocked, low-density plasmas are affected by kinetic physics related to long ion mean free paths. Reference 5 discusses a series of NLUF experiments on OMEGA that provide clear evidence of a transition from hydrodynamic-like to strongly kinetic behavior in shock-driven ICF implosions as the initial equimolar D³He gas density was decreased (illustrated in Fig. 140.56). References 6 and 7 discuss OMEGA experiments that lead to the first kinetic mix mechanisms in shock-driven ICF implosions; an important aspect of these data is illustrated in Fig. 140.57. These results are very important for testing non-

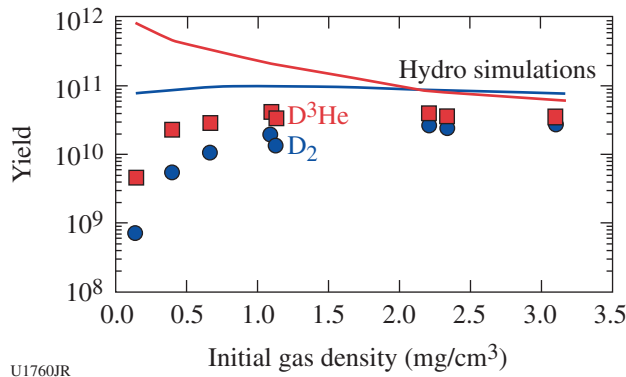


Figure 140.56 Comparison of measured (markers) and 2-D hydrocode-simulated (lines) D–D (blue) and D–³He (red) yields as a function of initial D³He gas density in shock-driven implosions on OMEGA. As the initial gas density decreases, plasma conditions become increasingly “kinetic” and the measured yields strongly deviate from hydrodynamic predictions. Ion kinetic effects—the escape of ions out of the hot-plasma region and the reduction in fusion reactivity caused by the depletion of high-energy-tail ions—are responsible for this trend. (This figure is from Ref. 5.)

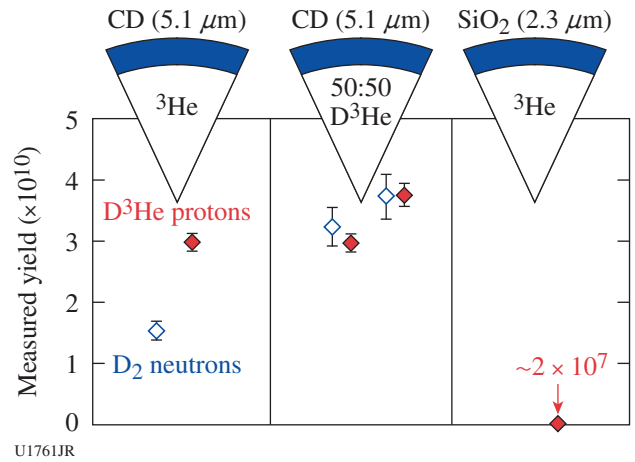


Figure 140.57 Measured D–³He yields (solid red) from 30-kJ OMEGA implosions of CD shells filled with ³He gas are similar to D–³He yields from implosions of CD shells filled with 50:50 D³He gas. Implosions of glass shells filled with ³He gas produce yields that are three orders of magnitude lower, ruling out D₂ contamination of the gas as an explanation for this result. The observed D–³He yields require the amount of shell deuterium mixed into the ³He gas to be ~10% of the ³He gas density. Ion diffusion is one mechanism that can generate such levels of mix in shock-driven implosions. (This figure is from Ref. 6.)

benchmarked ion diffusion models and codes that have recently been developed for high-energy-density (HED) plasmas.

Another publication in *Physical Review Letters*¹⁰ describes how monoenergetic proton radiography²¹ was used on OMEGA (as illustrated in Fig. 140.58) for the first observations of the structures, dynamics, and self-generated fields of pairs of laser-generated, high-Mach-number plasma jets that collide at various angles. Proton radiography has great sensitivity to fields, unlike x ray or other optical diagnostics.²² The observed self-generated magnetic fields, largely azimuthal around the colliding jets and generated by the well-known $\nabla T_e \times \nabla n_e$ Biermann battery effect near the periphery of the laser spots, were demonstrated to be “frozen in” the plasma and advected along the jet streamlines of the electron flow. For comparison to the proton radiographs, Fig. 140.58 shows electron flow streamlines predicted by an analytic model²³ and a plasma simulation using the 2-D hydrodynamic code *DRACO*²⁴ for the 180° collision case. The radiographs of collisions of noncollinear jets are relevant, for example, to the asymmetric structures and dynamics of the collisions in jet-driven, differentially rotating quasi-planar disk associated with accretion disks and outflows in astrophysics.

Results of other recent NLUF work will soon be submitted for publication. Topics will include implementation of a new

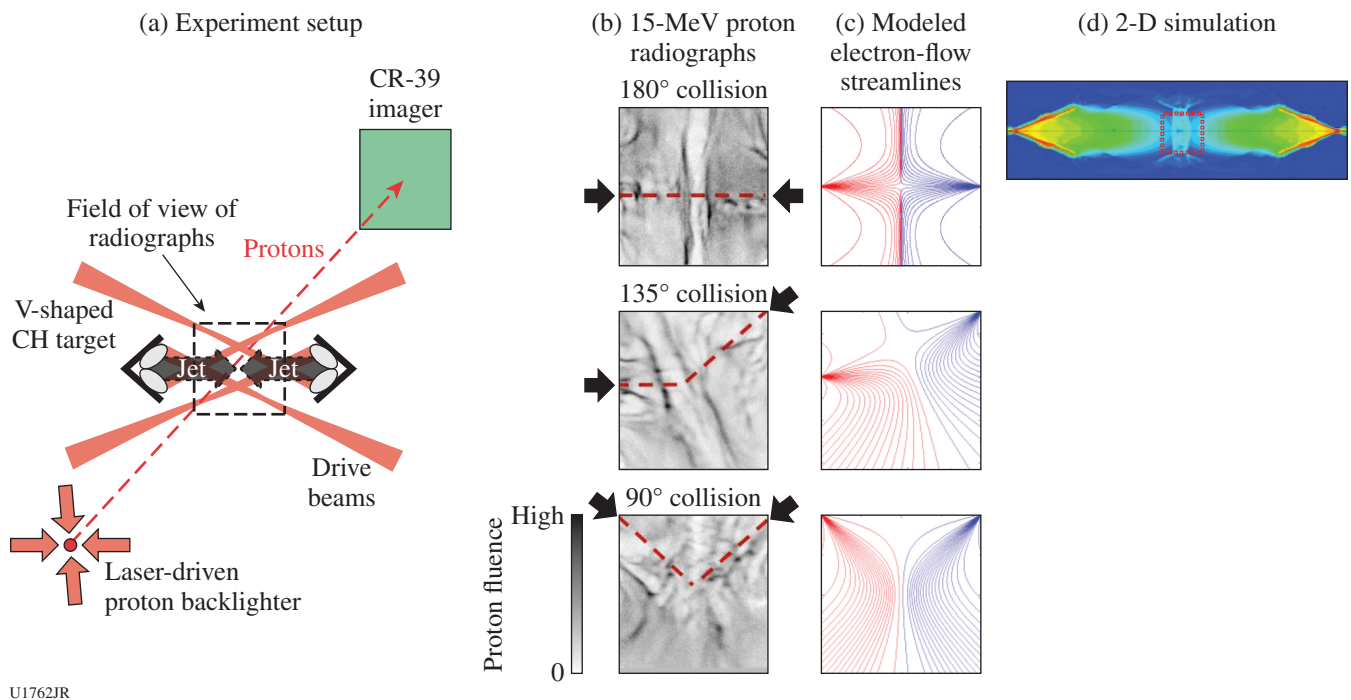


Figure 140.58

(a) A proton radiography setup on OMEGA and (b) recorded images of plasma jets colliding at various angles. (c) The images are compared to an analytic model of electron-flow streamlines and (d) to a 2-D *DRACO* simulation of the head-on collision case. The backlighter (D^3He -gas-filled, thin-glass-shell capsule imploded by 30 OMEGA laser beams and producing 3- and 14.7-MeV protons) was positioned 1 cm from the jet collision region. Each jet was formed by the collision of two plasma bubbles generated by laser beams incident on a V-shaped target (a). The angle between the two jets, determined by the positions of the two V-shaped targets, was either 180° (head-on), 135° , or 90° , as seen in the radiographs (b). The relative timing between backlighter and V-shaped-target drive was adjusted to sample the jets' propagation and collision at 4.7 ns from the onset of the drive on the V-shaped targets. (These results are from Ref. 12.)

multiple particle temporal diagnostic (multi-PTD) for probing kinetic and multi-ion-fluid effects; charged-particle stopping in weakly to moderately coupled plasmas; ion–electron equilibration in plasmas; hohlraum physics; nuclear reactions relevant to stellar and big-bang nucleosynthesis, and new work on magnetic reconnection.

Dynamics of High-Energy Proton-Beam Focusing and Transition into Solid Targets of Different Materials

Principal Investigator: B. Qiao (University of California, San Diego)

Co-investigators: C. McGuffey, J. Kim, and F. N. Beg (University of California, San Diego); M. S. Wei, P. Fitzsimmons, M. Evans, and R. B. Stephens (General Atomics); J. Fuchs and S. N. Chen (LULI, France); P. M. Nilson, D. Canning, and D. Mastro Simone (LLE); and M. E. Foord and H. S. McLean (LLNL)

The Proton Dynamics NLUF project, led by the University of California, San Diego, studied proton generation in the

regime of a kilojoule, multipicosecond (multi-ps) laser driver. High-current applications, such as proton fast ignition, may prefer this regime, but the focusing and transport of such high-current beams in materials have not been explored. A curved chemical vapor deposition (CVD) diamond target was shot with an OMEGA EP backlighter (BL) (1250 J in 10 ps) to focus protons into a Cu foil. Al ($13\text{-}\mu\text{m}$) or Ag ($7\text{-}\mu\text{m}$) transport layers were deposited on the front side of the Cu foil to investigate the material's dependence on transport of the intense proton beam.

The Cu K_α (8.048-keV) emission was imaged with the spherical crystal imager (SCI), as shown in Figs. 140.59(d)–140.59(f) for three target types [Figs. 140.59(a)–140.59(c)]. For the case of freestanding, separated foils, the Cu K_α signal was weak and diffuse over the entire Cu foil. This confirmed that the inherently diverging electron beam from the interaction contributed minimally to the Cu K_α signal at this standoff distance. For the case in which the gap was filled by a wedged structure [Fig. 140.59(b)], however, the signal was increased on the wedge center plane [Fig. 140.59(e)]. The emission is

greatest in the center, not at the edges of the wedge connection vertices, and no signal enhancement is observed in the region directly in contact with the wedge walls. This suggests that the signal is caused by *focused*, free-streaming particles within the vacuum gap rather than particles transporting through the wedge. For the case with a cone filling the gap [Figs. 140.59(c) and 140.59(f)], the effect was even clearer, with an $8\times$ higher peak signal than the freestanding case. Cu K_α yields are plotted in Fig. 140.59(g). These data indicate beam focusing in one dimension by the wedge and in two dimensions by the cone. This focusing effect has been studied in detail by our group using a subpicosecond laser²⁵ and particle-in-cell simulations,²⁶ while this result demonstrates that structures are still effective for focusing in the kilojoule, multipicosecond regime.

Two-dimensional particle-in-cell simulations are underway to further study the accelerating and focusing dynamics relevant to the OMEGA EP experiment. Two cases are being run: the freestanding target case and a conical enclosure case. In the

freestanding case, protons are initially focused because of the curvature of the target; however, a significant fraction of them diverge away. In the case with the cone, a strong focusing field is observed to persist along the cone's inner surface [Fig. 140.59(h)] with a strength comparable to the focusing field from the curved target, which confines the protons and increases their density. These simulations will continue to run for at least 30 ps as the protons continue to move. A diagnostic plane at the end of the cone collects individual particle information, including energy, which will be used to calculate the predicted Cu K_α yield from both electrons and protons for comparison to the experiment.

The proton and ion spectra were also measured continuously for energies down to 0.4 MeV, using a Thomson parabola spectrometer (TPIE) in-line with the axis of the curved target. In Fig. 140.60, the source spectrum from the curved foil is shown in black. This spectrum is in agreement with previous measurements using radiochromic film (RCF).²⁷ The cone cases (red)

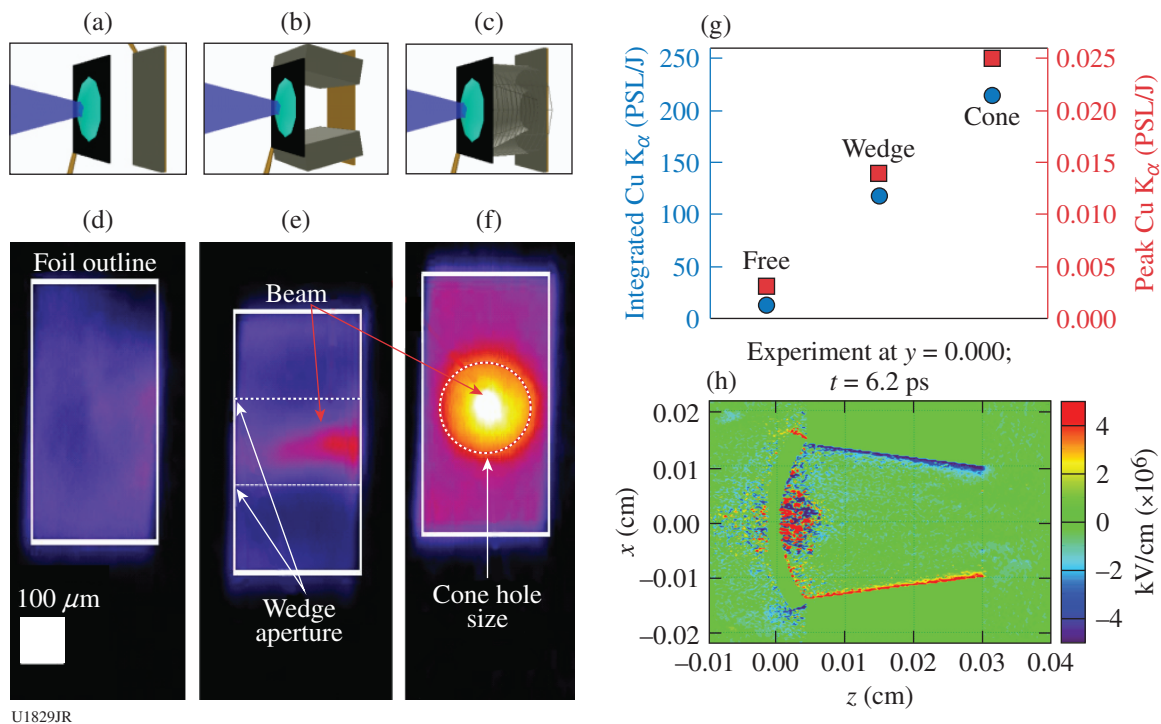


Figure 140.59

[(a)–(c)] Three target types used in the OMEGA EP experiment show heating by a focused beam as indicated by [(d)–(f)] the emission profiles of 8.048-keV Cu K_α . (g) Comparison of the signals shows that the total Cu K_α yield increased for the targets with structure, indicating a highly diverge source from the free case. The cone focused the beam, resulting in a 100- μm FWHM emission region. (h) Large-scale plasma suite (LSP) code simulation plot of the transverse electric field E_x at time $t = 6.2$ ps for a cone target.

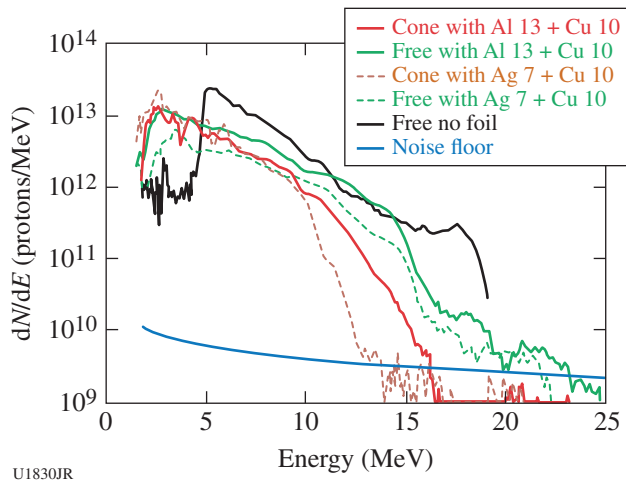


Figure 140.60
The absolute proton spectra measured with a Thomson parabola without the metals (black) and transmitted through two metals for both target types.

showed spectra similar to the free cases (green) except above 10 MeV. This is in agreement with our understanding of electron escape from the target: electrons that escape the target into the cone create an accelerating sheath that is quickly dampened, reducing the highest energy gained but not reducing the charge.

The peak beam current is estimated to be 4×10^9 A/cm², 300 μm behind the curved target, based on the recorded spectrum, assumed beam duration of 10 ps, and SCI emission region of 100-μm full width at half maximum. This density is sufficient to heat the metal foils locally to a warm dense matter, which models predict can cause self-modified beam transport. Our particle-in-cell codes predict that the stopping range can be measurably changed as beam densities increase from 10⁹ to 10¹⁰ A/cm², but thicker transport layers may be necessary.

Magnetic Shock

Principal Investigators: A. Spitkovsky (Princeton) and C. Huntington (LLNL)

The FY14 joint MagShock Campaigns (4 February and 18 August 2014) used the OMEGA laser to drive counter-propagating, colliding plasma flows to study their interaction. Characterization of the plasma conditions in this system on previous experiments provided a ready platform to investigate the electromagnetic-field structure generated during the flow interaction. The MagShock Campaigns studied the flow dynamics as the plasma interacts with a 10-T magnetic field

supplied by the magneto-inertial fusion electrical discharge system (MIFEDS). The physics of this OMEGA experiment are analogous to many astrophysical phenomena, including the dynamics of supernova ejecta streaming through a magnetized cosmic background plasma or interacting with magnetized star clusters.

The campaigns focused on proton radiography, interleaving shots where protons were generated via either target-normal sheath acceleration (TNSA) using an OMEGA EP beam or laser compression of a D³He-filled capsule. The quasi-monoenergetic 14.7-MeV protons from the capsules were particularly effective at imaging the field structure, as seen in Fig. 140.61. The long, narrow filaments stretched along the direction of plasma flow are consistent with the Weibel instability. Also persistent in the images are horizontal “plates”—a signature of magnetic Biermann-battery fields advected from the target surface to the imaging field of view. These results are currently under review in a manuscript titled “Observation of Magnetic-Field Generation Via the Weibel Instability in Interpenetrating Plasma Flows.”

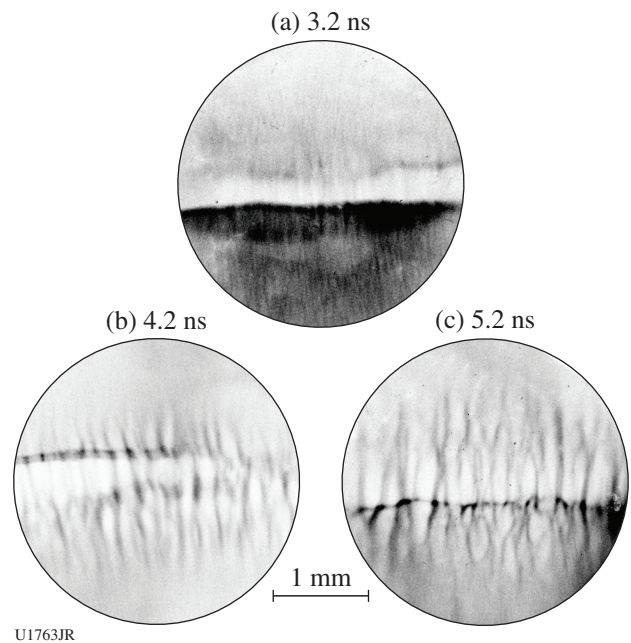


Figure 140.61
A time sequence of proton radiographs, each produced by the etching of a CR39 nuclear track detector to reveal the flux of 14.7-MeV protons. In each case, plasma flows enter from the top and bottom of the frame and interact near the mid-plane of the image. Strong filament growth occurs between 3 and 4 ns, consistent with the Weibel instability. The top–bottom asymmetry in the proton flux at early time will be investigated further in future experiments.

On OMEGA EP (EP-MagShock-14A in November 2013) we succeeded in porting our MIFEDS configuration to OMEGA EP utilizing the OMEGA EP MIFEDS system. This allows for increased experimental efficiency since we can use only one laser system to have both the magnetic fields and proton diagnostics. On OMEGA EP-MagShock-14A we tried a different magnetic configuration using a Helmholtz coil. It provided a magnetic field (7 T on axis) along the direction of the flow, unlike our previous work where the field was orthogonal to the flow. While overall the plate-filament structure was not significantly affected by the applied field, plasma did get onto the magnetic-field lines and new features in the proton image were detected. In Fig. 140.62 we show (a) the experimental configuration of this day along with two proton images taken at 4 ns for shots (b) without a B field

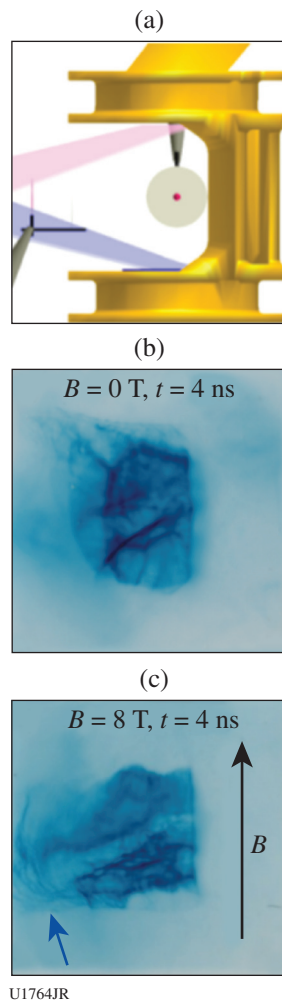


Figure 140.62
Experiments with the external field parallel to the flow direction (EP-MagShock-14A). (a) View of the experimental setup from the direction of proton film; (b) proton image without external field at $t = 4 \text{ ns}$; and (c) proton image with external field. Note the blowout area indicated by the blue arrow.

and (c) with B field parallel to the flow. The Biermann plates are clearly visible, although they are tilted in these experiments likely because additional plasma was ablated off of the MIFEDS stalk by reflected laser light. The differences induced by the B field are highlighted with a blue arrow [Fig. 140.62(c)]. We notice new wispy proton caustics indicating field enhancement on plasma-loaded field lines that undergo sideways expansion. This experiment suggests that we can produce magnetized plasma, if plasma is loaded along the magnetic field, and points to the way forward to generate magnetized shocks in the laboratory.

Study of Relativistic Laser–Plasma Interaction and Fast-Electron Beam Dynamics Using the 10-ps High-Contrast OMEGA EP Laser with a Controlled Pre-Plasma

Principal Investigators: M. S. Wei and R. B. Stephens (General Atomics)

Co-investigators: C. McGuffey, B. Qiao, and F. N. Beg (University of California, San Diego); A. Link and H. S. McLean (LLNL); W. Theobald, D. Haberberger, and A. Davies (LLE); and Y. Sentoku (University of Nevada, Reno)

Lead graduate student: J. Peebles (University of California, San Diego)

Efficient conversion of high-intensity laser energy to fast electrons and their subsequent transport are fundamental to high-energy-density (HED) science, which has many potential applications such as fast-ignition (FI) laser fusion, warm dense matter by isochoric heating, and a short-pulse, bright x-ray source. The energy coupling is controlled by the laser–plasma interaction (LPI) dynamics, which strongly depends on laser-intensity distribution and the plasma density scale length at the LPI interface as well as the dynamic response of the transport material. In our previous experiments using the high-intensity, high-energy (up to 1.5 kJ) OMEGA EP laser with low-contrast pulses, we observed electron beams dynamically evolved from a single diffuse spot in subpicosecond interaction into multiple angularly separated electron filaments over a 10-ps interaction.²⁸ Particle-in-cell simulations suggest that high-intensity laser beams undergo filamentation, hole-boring, and hosing instabilities over multiple picoseconds in the preformed plasma created by the intrinsic nanosecond pedestal prepulse, leading to the observed electron filaments.²⁹ The objectives of this General Atomics NLUF project is to further investigate the LPI dynamics and fast-electron transport dependence on pre-plasma, pulse duration, and target material using the high-contrast OMEGA EP laser. In our FY13 NLUF experiments we showed that the high-contrast OMEGA EP laser produces a more-confined electron beam, leading to an improved energy coupling to the target.³⁰

In the FY14 NLUF experiment, we focused on the investigation of the pre-plasma effect on relativistic LPI and the resultant fast-electron beam dynamics by systematically varying pre-plasma scale length using a separate UV beam prior to the high-intensity OMEGA EP pulse. For this study, we used the identical multilayered planar foil targets composed of an Al substrate with a Cu x-ray tracer layer buried $\sim 125 \mu\text{m}$ below the front surface and a large, 2-mm \times 2-mm, 1-mm-thick conductive carbon layer at the back to minimize refluxing, similar to that used in previous experiments. A low-energy UV beam (20 J, 1-ns pulse duration) was focused onto the target's front surface with a large focal spot using a 750- μm distributed phase plate to produce pre-plasma. The 10-ps, high-energy (up to 1250 J), high-intensity ($3 \times 10^{19} \text{ W/cm}^2$) OMEGA EP pulse was normally incident onto the target with several timing delays, i.e., 0.2, 0.5, 0.7, and 1.0 ns, with respect to the beginning of the UV beam. For comparison, shots were also taken without the UV beam-produced pre-plasma. A 2-D radiation-hydrodynamics simulation using the *HYDRA* code suggested that the scale length of the preformed plasmas was about 14, 40, 80, and 110 μm , respectively, for the corresponding OMEGA EP beam-delay times mentioned above. The intrinsic prepulse (1 mJ, 3-ns duration)-produced pre-plasma had a scale length of $\sim 4 \mu\text{m}$.

Fast electrons were characterized by measuring their induced Cu K_α fluorescence spot with a spherical crystal imager (SCI) and the total K_α yield by a calibrated x-ray spectrometer using a curved highly oriented pyrolytic graphite (HOPG) crystal (ZVH). A fast-electron-induced, high-energy bremsstrahlung spectrum was monitored by two fixed-port bremsstrahlung MeV x-ray spectrometers (BMXS's). A magnetic spectrometer was also fielded along the axis of the OMEGA EP beam to monitor the escaped fast-electron energy spectrum. In addition, an angular filter refractometer (AFR) with a short-pulse (10-ps), 4ω optical probe was used to characterize a pre-plasma electron density profile. A proton probe was also utilized to map electromagnetic fields and structures in relativistic LPI's.

As shown in Fig. 140.63(a), the fast-electron temperature inferred from the measured bremsstrahlung radiation spectrum decreases with increasing pre-plasma scale length. It drops from $\sim 3 \text{ MeV}$ with the intrinsic prepulse produced pre-plasma (scale length of $L = 4 \mu\text{m}$) to $\sim 1.2 \text{ MeV}$ with the UV beam-produced large pre-plasma ($L = 110 \mu\text{m}$). Compared with the intrinsic prepulse case, the measured 2-D SCI Cu K_α images indicate that the fast-electron beam significantly spreads out when relativistic LPI occurs in a large-scale-length pre-

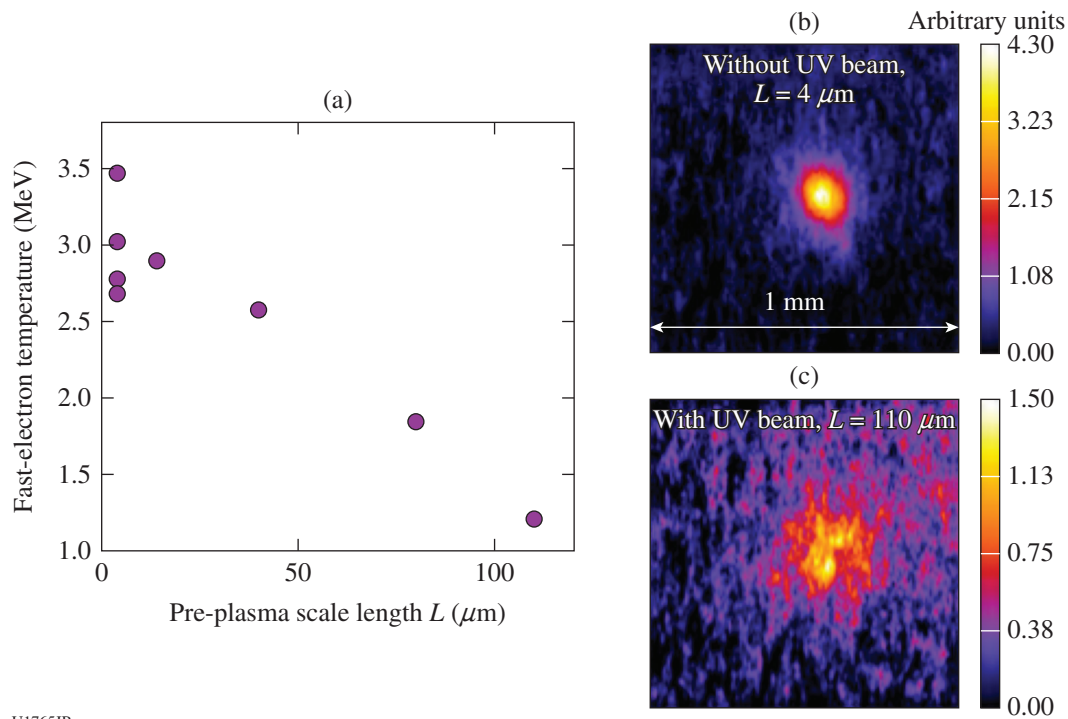


Figure 140.63

(a) The inferred hot-electron temperature from the measured bremsstrahlung x-ray spectrum as a function of the preformed plasma density scale length. (b) The measured 2-D Cu K_α spot from the 10-ps relativistic interaction without the UV beam and (c) with the UV beam-produced pre-plasma.

plasma. The measured R_{50} spot size is nearly doubled for the $L = 110\text{-}\mu\text{m}$ pre-plasma case [Fig. 140.63(c)] compared to the intrinsic pre-plasma case [Fig. 140.63(b)], i.e., $266\ \mu\text{m}$ versus $136\ \mu\text{m}$, where R_{50} is the radius of the spot that contains 50% of the total K_α yield. We also note that there was $2.3\times$ less energy within the center spot with a radius of $125\ \mu\text{m}$ for the $L = 110\text{-}\mu\text{m}$ case compared to the intrinsic pre-plasma case.

High-resolution proton probing images of electromagnetic fields that result from relativistic LPI have revealed strong nonlinear phenomena when interactions occurred in large preformed plasmas. Figure 140.64 shows the observed field structures during the high-intensity OMEGA EP laser interaction with an $L = 40\text{-}\mu\text{m}$ -scale-length pre-plasma. Multiple channels and bubbles can be clearly seen. Such phenomena were not observed with the intrinsic pre-plasma case. Instead, a planar sheath (not shown here) was seen expanding backward with a high velocity (30% of the speed of light) from the target's front surface.

In summary, the FY14 General Atomics–led NLUF experiment has been successfully performed to further investigate the effect of preformed plasma in a controlled way with added diagnostics. Strong nonlinear interaction phenomena such as channel and bubbles were directly observed during relativistic

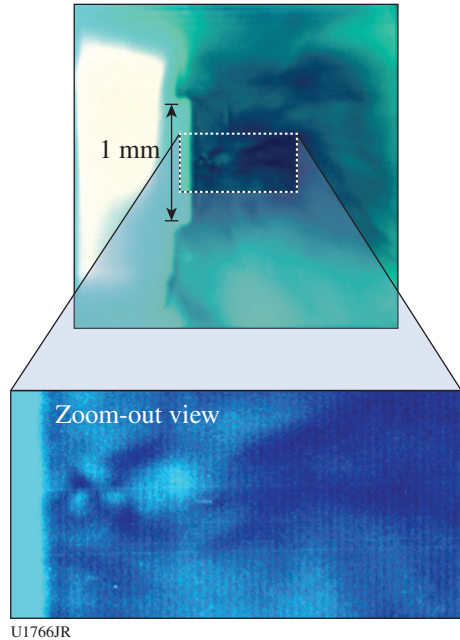


Figure 140.64
Proton probing images (false color) of electromagnetic-field structures during nonlinear relativistic laser–plasma interaction with a UV beam-produced large pre-plasma ($L = 40\ \mu\text{m}$). Channels and bubbles are clearly visible.

tic LPI in large preformed plasmas. This led to a significant spread of the fast-electron beam and the reduced fast-electron temperature observed on the solid targets. Detail data and PIC modeling is underway.

FY14 Laboratory Basic Science (LBS) Program

In FY14, LLE issued a solicitation for LBS proposals to be conducted in FY15. A total of 25 proposals were submitted. An independent review committee reviewed and ranked the proposals; on the basis of these scores, 14 proposals were allocated 20 shot days at the Omega Laser Facility in FY15. Table 140.VI lists the approved FY15 LBS proposals.

Seventeen approved LBS projects were allotted Omega Facility shot time and conducted a total of 269 target shots at the facility in FY14 (see Table 140.VII). This work is summarized in this section.

Search for Nuclear Excitation by Electron Capture in Osmium and Thulium

Principal Investigator: L. Bernstein (LLNL)

Shot Principal Investigator: R. F. Heeter (LLNL)

Co-investigators: D. Bleuel, J. Emig, and S. Ross (LLNL); M. Comet, V. Meot, F. Phillippe, and C. Reverdin (CEA)

Nuclear excitation by electron capture (NEEC) is an exotic process that has never been observed in the laboratory, but in stellar plasmas it is thought to populate low-lying nuclear excited states and may modify neutron capture and other astrophysical rates. In laser-driven plasmas created on $\sim 1\text{-ns}$ time scales, NEEC may be observed through gamma decays re-emitted on $\sim 5\text{-ns}$ time scales, after the plasma has cooled and x-ray emission is negligible. Earlier experiments searched for 8.41-keV NEEC in ^{169}Tm hohlraums (made from rolled thulium foil), using erbium as a null comparison, and found an ambiguous signature.

The FY14 experiments revisited these measurements and also searched for 9.76-keV NEEC decay emission in isotopically pure ^{187}Os -lined Ti hohlraums, with ^{192}Os as a null comparison. Ti was chosen because it could be electroplated with ^{187}Os , while not providing any x-ray contamination in the NEEC spectral band. The hohlraums were 0.6 mm in diameter and were driven at 10 kJ in 1 ns using 20 beams of the 60-beam OMEGA.

In the experiments, optical Thomson-scattering data obtained 300 μm outside the cavity laser entrance hole showed electron temperatures of $\sim 4.3\ \text{keV}$ and densities $\sim 4 \times 10^{20}/\text{cm}^3$. A suite of time-integrated and time-resolved x-ray spectra were obtained

Table 140.VI: LBS proposals approved for shots in FY15.

Principal Investigator	Affiliation	Title	OMEGA shot days allocated	OMEGA EP shot days allocated	Joint shot days**
R. Smith	LLNL	X-Ray Diffraction Study to Map Out Pressure–Temperature Phase Space in a Key Planetary Mineral: MgO	2	0	0
G. Fiksel	LLE	Detailed Study of Magnetic Fields During Magnetic Reconnection in High-Energy-Density Plasma	0	1	0
R. Betti	LLE	Ultra-Strong Spherical Shock for High-Energy-Density Physics Studies	2	0	0
D. E. Fratanduono	LLNL	Exploring Earth's Lower Mantle	1	0	0
M. Beckwith	LLNL	EXAFS Study of Iron Melting Temperature at Earth's Core Conditions	2	0	0
H.-S. Park	LLNL	Weibel Instabilities and Astrophysical Collisionless Shocks from Laser-Produced Plasmas	2	0	0
W. Theobald	LLE	Integrated Channeling for Fast Ignition	1	1	1
H. Chen	LLNL	Demonstration of a Relativistic Electron–Positron Pair Plasma	0	2	0
J. R. Davies	LLE	Laser-Driven Adiabatic Compression of Magnetized Plasma	1	0	0
C. Stoeckl	LLE	Spectroscopy of Neutrons Generated Through Nuclear Reactions with Light Ions in Short-Pulse Laser Interaction Experiments	0	1	0
A. Pak	LLNL	Phase Separation of Hydrocarbons at High Pressure	0	1	0
C. Wehrenberg	LLNL	Flow Stress and Deformation Mechanisms for Plasticity in Shock-Compressed Vanadium	0	1	0
C. J. Forrest	LLE	Studies of the Deuteron Break-up Reaction at 14 MeV Using High-Energy-Density Plasmas (HEDP's)	1	0	0
D. Martinez	LLNL	Eagle Pillar Formation on OMEGA EP	0	1	0

with CEA's X-Ray CEA Crystal Spectrometer (XCCS) and LLNL's MSPEC and HENWAY spectrometers; the XCCS view is illustrated in Fig. 140.65. These measurements failed to show NEEC emission in either ^{169}Tm or ^{187}Os within the sensitivities of these instruments but are able to set an upper bound on the highly uncertain NEEC rates. Improved measurements with larger quantities of ^{187}Os and more-sensitive spectrometers could further constrain NEEC rates.

Viscosity Measurements on Liquid Silica

Principal Investigator: P. M. Celliers (LLNL)

Co-investigators: M. A. Barrios and A. E. Gleason (LLNL)

This campaign was the third in a series to demonstrate a method for determining the viscosity of a high-pressure

fluid created by propagating a strong shock front through an initially transparent sample. This measurement technique is based on observing the evolution of a spectrum of perturbations imposed on a multimegabar shock front passing through the sample material. The viscosity of the liquid state just behind the shock front is expected to influence the decay rate of the perturbations as the shock front propagates; detailed measurements of the perturbation state can be compared with calculations in order to assess the viscosity. The sample under study is liquid silica (SiO_2), produced by propagating the shock through samples of either alpha quartz or fused silica. The viscosity of high-pressure liquid silica has obvious geophysical relevance, and measurements in the megabar domain are not possible with conventional methods. Two earlier campaigns in 2010 and 2012 examined the shock response

Table 140.VII: Approved FY14 LBS proposals.

Principal Investigator	Affiliation	Project Title
A. Bernstein	LLNL	Nuclear Excitation by Electron Capture in a Reduced-Scale Hohlraum
P. M. Celliers	LLNL	Measurement of the Viscosity of Shock-Compressed Fluids of Water and Silica
H. Chen	LLNL	Exploring Pair Plasmas and Their Applications Using the OMEGA EP and OMEGA Lasers
G. Fiksel	LLE	Magnetized ICF Implosions on OMEGA
R. F. Heeter	LLNL	Gatling-Gun Long-Duration Radiation Sources on OMEGA EP for Sustained-Drive Hydrodynamics and Low-Density Atomic Physics Applications on OMEGA EP and the NIF
S. Ivancic	LLE	Channeling Through Long-Scale-Length Plasmas
M. Lafon	LLE	Gigabar Shocks for Shock-Ignition and High-Energy-Density-Physics Studies
T. Ma	LLNL	Creation and Measurements of Novel High-Pressure Electrified States of Matter
D. Martinez	LLNL	Imprint-Driven Richtmyer–Meshkov Instability in Thick Planar Targets
D. McNabb	LLNL	Thermonuclear Reactions in Stellar Plasmas
S. Nagel	LLNL	Measuring Charged-Particle Stopping Powers Using Short-Pulse Lasers
P. M. Nilson	LLE	Radiation Hydrodynamics of Double-Ablation Fronts
H.-S. Park	LLNL	Astrophysical Collisionless Shocks and Magnetic Fields in Laser-Produced Plasmas
P. K. Patel	LLNL	Fast-Electron Focusing Using Ellipsoidal-Tip Cone Targets for Fast Ignition
J. R. Rygg	LLNL	Structure and Equation of State of Solid and Superionic Warm Dense Matter
R. Smith	LLNL	Understanding Strength Effects in Diamond Ablators Used for Ramp Compression
C. Stoeckl	LLE	Spectroscopy of Neutrons Generated Through Nuclear Reactions with Light Ions in Short-Pulse Laser Interaction Experiments

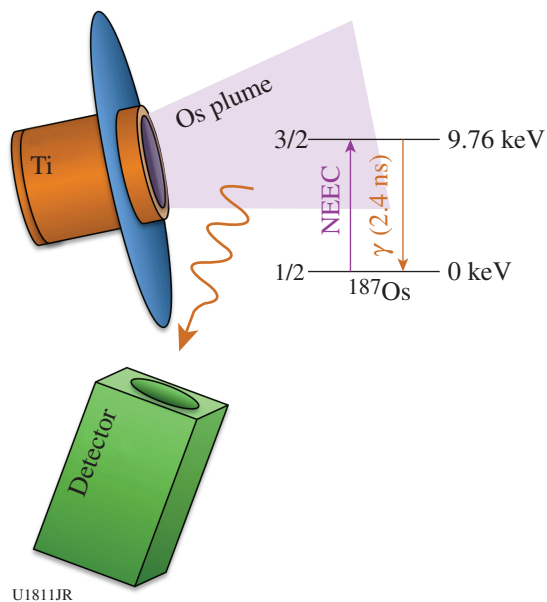
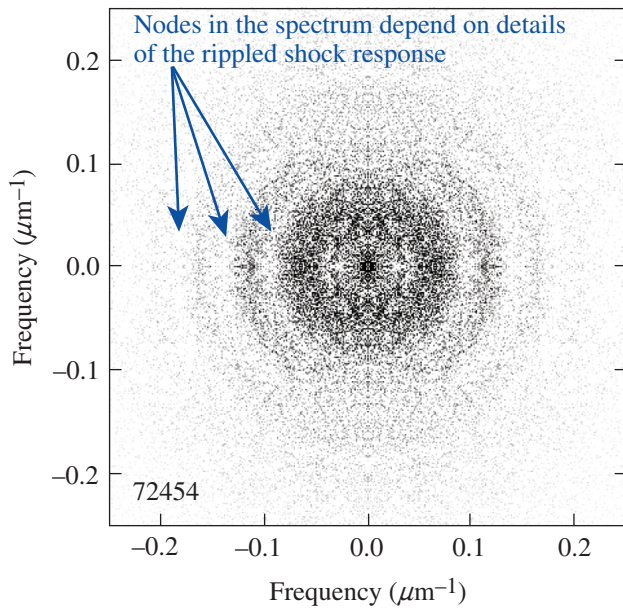


Figure 140.65
 Experimental configuration showing the Os-lined Ti hohlraum with an over-the-shoulder view of CEA's x-ray CEA crystal spectrometer (XCCS), together with the level diagram for nuclear excitation by electron capture (NEEC) and subsequent gamma decay in ^{187}Os .

to perturbation spectra that were generated by both random and coherent patterns imposed on the sample surface at the interface with the ablator. These initial experiments demonstrated the feasibility of using the OMEGA high-resolution velocimeter (OHRV) to produce quantitative measurements of the multimode velocity perturbations directly from the surface of the reflecting rippled shock front.

In the 2014 experiments, the shocks were driven using a hohlraum coupled to a $50\text{-}\mu\text{m}$ CH (PMMA) ablator followed by the sample. Although measurements on water samples as well as silica were envisaged for this campaign, that option assumed successful fabrication of novel water cell targets, which turned out to be more difficult than expected and precluded collecting a dataset on water in this campaign. Nevertheless, excellent data were obtained for silica.

In the experiments, as the shock passed through this interface, the perturbations were transferred to the shock front, where they were detected and measured quantitatively by the OHRV. Figure 140.66 shows an example velocity spectrum for an $\sim 200\text{-GPa}$ shock driven into fused silica. The



U1817JR

Figure 140.66

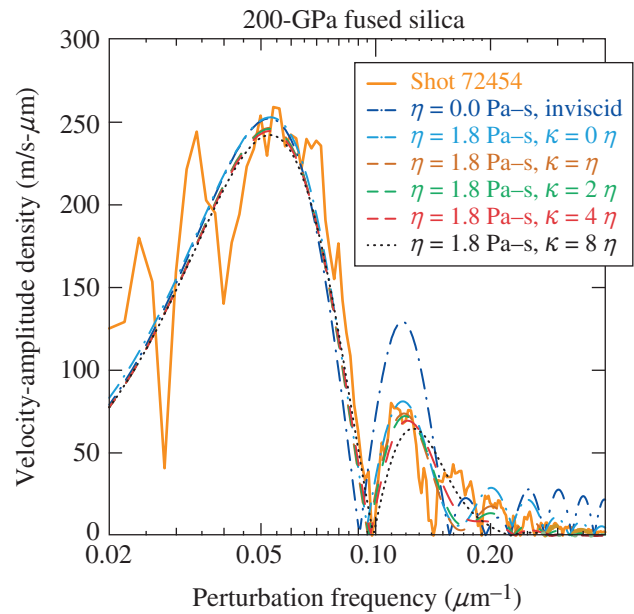
Two-dimensional velocity spectral density of a rippled shock front generated at a roughened interface between a PMMA ablator and a fused-silica sample recorded 800 ps after passage of the shock through the interface (shot 72454). The gray scale is proportional to the mode velocity amplitude. Nodal regions are where the mode velocity is near zero at the time of the probing, corresponding to those modes that are undergoing a velocity reversal at the probing time.

spectrum shows the presence of nodal zones—modes whose instantaneous oscillation velocity was near zero at the time of the OHRV probe. These nodal patterns are expected from the multimode solution of the rippled shock evolution. Details of the amplitudes and positions of the nodes depend on the viscosity. Model calculations employing an analytical expression derived by Miller and Ahrens³¹ are used to estimate the mode amplitude as a function of spatial frequency, shown in Fig. 140.67. Here, we see that the observed spectrum is consistent with viscosities ~ 1.8 Pa-s (20 poise).

Exploring Pair Plasmas and Their Applications

Principal Investigator: H. Chen (LLNL)

In FY14, an LLNL/LLE team continued the project “Exploring Pair Plasmas and Their Applications” with two LBS shot days on OMEGA EP. The experiments used the short-pulse beams to produce jets of electron–positron antimatter pairs. The experiments focused on measuring the pair yield and its dependence on the target material. The experiments successfully probed the basic physics processes involved in pair generation, and the data reveal discrepan-



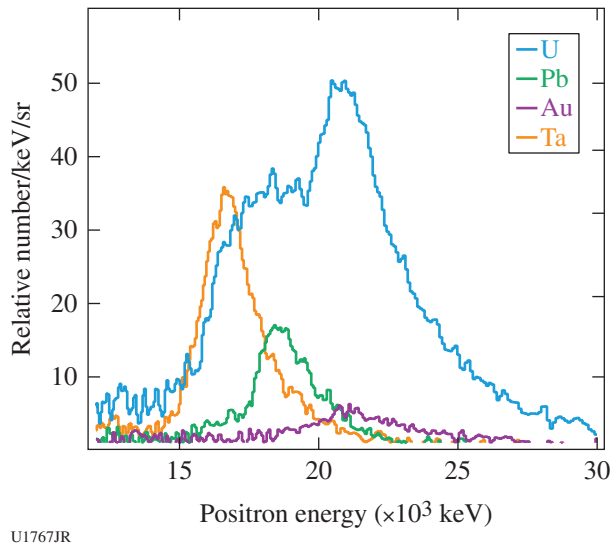
U1840JR

Figure 140.67

Background-subtracted and azimuthally averaged mode amplitude as a function of mode spatial frequency. The first node is near $0.09 \mu\text{m}^{-1}$, the second near $0.14 \mu\text{m}^{-1}$, and so on. Also shown are theoretical mode amplitudes expected for the inviscid response and several viscous cases, where the bulk viscosity κ is taken to be different multiples of the shear viscosity η . The data suggest the viscosity is ~ 1.8 Pa-s (18 poise).

cies between experiments and theory. A total of 31 shots were performed.

The OMEGA EP short-pulse beams (~ 1 kJ in 10 ps) irradiated 1-mm-thick targets of Sn, Ta, Au, Pb, and U. Unexpectedly high positron yields were recorded from the Ta, Pb, and U targets (see preliminary results in Fig. 140.68), in disagreement with the expected $\sim Z^4$ scaling from the Bethe–Heitler process. The reasons for the discrepancy, once understood, should significantly impact future pair-production experiments. Previous experiments almost exclusively used gold targets. The prior experiments showed that quasi-monoenergetic relativistic positron jets are formed during high-intensity irradiation of thick gold targets^{32,33} and that these jets can be strongly collimated³⁴ using the magneto-inertial fusion electrical discharge system (MIFEDS).³⁵ The external field produces a 40-fold increase in the peak positron and electron signal.³⁴ The FY14 results suggest that the pair density could be increased up to an order of magnitude with U instead of Au targets. This would enable the laboratory study of relativistic pair plasmas that are important to understanding some of the most exotic and energetic systems in the universe.³⁶



U1767JR
 Figure 140.68
 The Z-dependent positron-yield measurement on OMEGA EP in FY14.

Fusion Enhancement in Spherically Imploded Magnetized Targets MagICF_14A

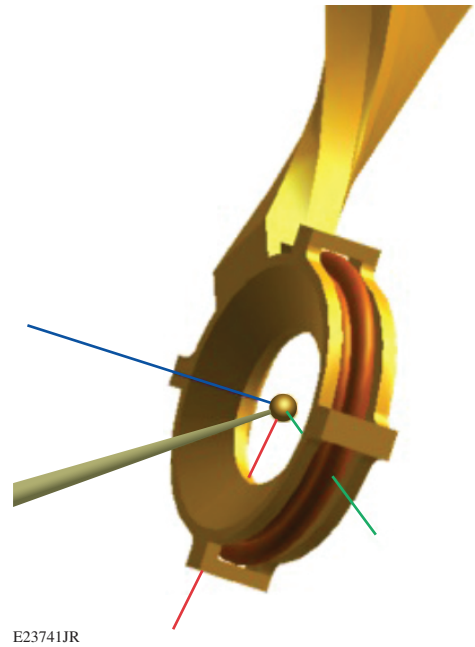
Principal Investigator: G. Fiksel (LLE)

The purpose of the MagICF Campaign on 16 July 2014 was to demonstrate a neutron-yield enhancement in magnetized spherical ICF implosions. A magnetic field of up to 15 T was embedded in a spherical target, which was a spherical plastic (CH) shell with a thickness of $22.3 \pm 0.4 \mu\text{m}$, filled with 10 atm of D_2 gas. The field was created using a single magnetic coil on the equatorial plane of the target, energized by MIFEDS. The coil was tilted along the P5–P8 axis to accommodate different diagnostics, and the spherical target was compressed using 40 OMEGA beams in a polar-direct-drive configuration along the same axis, delivering ~ 16.9 kJ of energy on target (see Fig. 140.69 for the experimental setup).

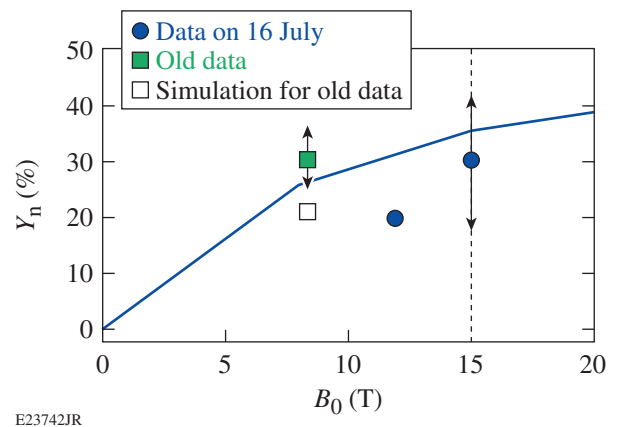
The results were compared to the result published in 2011 (Ref. 37) when an 8-T field was embedded in the target, leading to a $30 \pm 5\%$ neutron-yield enhancement while the simulation predicted a 22% increase. Ten successful shots were conducted on the shot day, including four shots without a magnetic field as the baseline, four shots with $B = 15$ T, and two shots with $B = 12$ T. One of the shots with a 12-T field had very different target specifications ($23.4 \mu\text{m}$ in shell thickness) and was not included in the analysis. For the shots with a 15-T seed magnetic field, the average neutron-average ion temperature and the average neutron yield increased by $9 \pm 2\%$ and $30 \pm 7\%$, respectively. These results agree with the results of 2011 and

with the simulation-predicted neutron yield increase of 35.6% (see Fig. 140.70).

Furthermore, the x-ray framing camera shows a brighter self-emission from the central hot region in magnetized targets, which indeed indicates a higher temperature in magnetized implosions.



E23741JR
 Figure 140.69
 Experimental setup showing the coil and the target.



E23742JR
 Figure 140.70
 Comparison of recent and previous experimental results and simulations.

Initial Applications of the Sustained-Drive “Gatling-Gun” X-Ray Source

Principal Investigator: R. F. Heeter (LLNL)
 Shot Principal Investigator: D. Martinez (LLNL)
 Co-investigators: J. Kane (LLNL); R. C. Mancini (University of Nevada, Reno); and B. Villette and A. Casner (CEA)

This FY14 OMEGA EP campaign continued the successful development of “Gatling-gun” multihohlraum-array x-ray sources began in FY13, in which a radiation temperature of 90 eV was produced for 30 ns. This capability is important for multiple physics experiments, including investigations of (a) x-ray photoionization equilibrium at relatively low plasma densities of $\sim 10^{18}$ ions/cm³ and (b) the hydrodynamics of pillar formation from directional radiation relevant to the Eagle nebula.

The FY14 campaign used a copper three-hohlraum array [shown in Fig. 140.71(a)] to drive a Ti photoionization sample and a hydrodynamics sample, simultaneously, demonstrating the capabilities of the Gatling-gun hohlraum. The three hohlraums were heated in succession using three UV beams, each

with 10-ns square pulses and 3.8 kJ of energy. The hohlraum temperature was measured with CEA’s Mini-DMX, which again recorded 80 to 100 eV over 30 ns.

The photoionization sample consisted of a 0.6-mm \times 0.6-mm \times 0.5- μ m Ti foil sandwiched between two 1- μ m-thick tamper layers of 1-mm \times 1-mm CH. The emission spectrum, recorded using the variable-spaced grating (VSG) diffraction-grating spectrometer, showed strong Cu emission from the hohlraum and a weak signal in the expected range of the Ti L-shell emission lines. Interpretation of the spectrum is ongoing.

The hydrodynamics sample consisted of 50 mg/cm³ of resorcinol formaldehyde (R/F) foam with an embedded, solid-density CH ball of 350- μ m diameter. The hydrodynamics of the sample was studied using a Ti area backlighter driven by a 1-ns, 1.25-kJ UV beam with a 500- μ m focal spot. The backlit image was imaged onto a single-frame x-ray framing camera with a 4 \times 4, 20- μ m pinhole array, providing a detailed composite radiograph from the multiple images. Figure 140.71 shows the recorded images, in which the shock front has propagated into the R/F foam past the CH ball.

Both aspects of the experiments successfully demonstrated the application of the Gatling gun, resulting in additional shots for further specific applications.

Laser Channeling Through Large-Scale-Length Plasmas

Principal Investigators: S. Ivancic and W. Theobald (LLE)
 Co-investigators: C. Stoeckl and C. Ren (LLE); and H. Habara and K. A. Tanaka (Osaka University, Japan)

Propagating a laser beam at relativistic intensities ($>10^{18}$ W/cm²) through a plasma with a large density scale length is dominated by highly nonlinear interactions. These effects are important for both fundamental aspects of relativistic laser–plasma interaction physics and applications such as fast ignition in inertial confinement fusion.³⁸ The purpose of this LBS experiment was to study the physics of channel formation with high-intensity IR laser pulses of a longer, 100-ps pulse duration and compare the results to previous results from a shot day with 10-ps pulses. The experiments showed that 100-ps infrared pulses with a peak intensity of 1×10^{19} W/cm² produced channel-to-plasma densities beyond critical, while 10-ps pulses with the same energy but higher intensity did not propagate as far.³⁹ The experiments were carried out on the OMEGA EP Laser System using two UV laser beams to create, on planar plastic targets, large-density-scale-length plasmas with a scale length of 250 μ m at the critical density (n_c) of the IR laser. The channel-

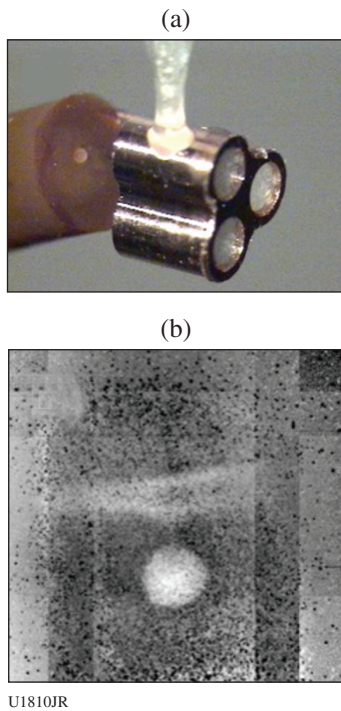


Figure 140.71
 (a) Target image showing the Gatling-gun triple hohlraum and attached resorcinol formaldehyde (R/F) foam with an embedded solid-density CH ball. (b) Radiograph reconstructed from a 16-pinhole array gated at $t = 35$ ns.

ing laser pulse was an IR beam with energy of up to 2.6 kJ. The vacuum peak intensities were 1×10^{19} W/cm² for 2.6-kJ, 100-ps pulses compared to 4×10^{19} W/cm² for 1-kJ, 10-ps pulses. The average laser intensities are about an order of magnitude lower. The focal position of the channeling beam was set to 750 μ m from the original target surface, and the corresponding electron plasma density at that location was predicted to be $n_e = 2.5 \times 10^{20}$ cm⁻³. The plasma was diagnosed using an optical diagnostic employing a 10-ps, 263-nm probe laser⁴⁰ to measure simultaneously the background plasma density and to image the channel. The phase gradients are discriminated by a technique using an angular spectral filter [angular filter refractometry (AFR)] that is placed in a Fourier plane behind the collection optics of the probe beam.⁴¹

Figure 140.23 from **Channeling Multikilojoule High-Intensity Laser Beams in an Inhomogeneous Plasma** (p. 235) shows measured channels at different probing times for 10-ps and 100-ps laser irradiation. The channel is visualized by the perturbations in the AFR contours. The contours bend as a result of strong density gradients created by the channeling pulse. The top row shows the results for the 10-ps pulse. The head of the channel reached at 6 ps to a position 450 μ m from the original target surface, corresponding to $0.6 n_c$. The last contour in the collection system corresponds to light that is refracted through a peak density above n_c (1.4×10^{21} cm⁻³). The channel was observed up to 200 ps after its creation. Later in time, the tip of the channel retreats backward with a velocity of $\sim 3 \times 10^7$ cm/s away from the target surface. There is a clear difference in the channel depth between the 10-ps and 100-ps pulses. The 100-ps pulse [Figs. 140.23(e)–140.23(h)] reaches to the contour closest to the original target surface, indicating that a density $>1.4 \times 10^{21}$ cm⁻³ has been reached. The 100-ps pulse shown in Fig. 140.23(e) reached in only 18 ps to about the same depth as the 10-ps pulse. The 100-ps pulse continues to bore through the plasma, reaching overcritical density at 65 ps after the start of the laser beam. The upper-contour bands in the lower-density region are smoothly shifted in space, while the contours at higher density inside the channel are highly distorted and obscured. Bright fourth-harmonic emission of the channeling beam was measured in the vicinity of the critical surface [Figs. 140.23(e)–140.23(h)] with the 100-ps pulse. Harmonics from the critical-density surface have been observed in experiments with high-intensity laser beams interacting with solid-density plasmas.⁴² No self-generated harmonic emission was observed with the 10-ps pulse, confirming that it did not reach as high a density as the 100-ps pulse.

Spherical Strong-Shock Experiments Using Medium-Z Ablators on OMEGA

Principal Investigators: M. Lafon and W. Theobald (LLE)
Co-investigators: R. Nora, R. Betti, J. R. Davies, K. S. Anderson, M. Hohenberger, and C. Stoeckl (LLE); A. Casner (CEA); and X. Ribeyre (University of Bordeaux, France)

The shock-ignition concept⁴³ is an alternative to the conventional hot-spot approach of inertial confinement fusion that involves generating of an intense shock at the end of the assembly pulse. The ignitor shock is generated by a power spike at the end of the laser pulse. The shock strength increases as a result of convergence and reaches 3 to 5 Gbar as the shock travels through the imploding shell. A key milestone for shock ignition to be a credible path to ignition is to demonstrate the generation of a seed shock pressure of at least 0.3 Gbar at laser intensities of 5×10^{15} to 1×10^{16} W/cm². The spherical strong-shock platform was developed to study the seed pressures at shock-ignition–relevant laser intensities on OMEGA. The experiments are very promising and have demonstrated seed pressures exceeding 0.3 Gbar (Ref. 44). At such intensities, laser–plasma instabilities play an important role in the coupling of laser energy to the target. The goal of this LBS day was to study the effect of different Z ablator materials on shock generation and laser–plasma instabilities producing hot electrons.

The 60 UV beams from the OMEGA laser are focused to high intensity (overlapping beam intensity of $\sim 6 \times 10^{15}$ W/cm²) on the surface of spherical solid targets to launch a shock wave that converges in the center. The targets with an outer diameter of 430 μ m consist of an inner plastic (CH) core that is doped with titanium with an atomic concentration of 5% and an outer ablator layer of a different material. Four different ablator materials were used: 20 μ m Be, 34 μ m CH, 28 μ m C, and 20 μ m SiO₂. The shock wave converges in the center of the solid target and heats a small volume (radius <10 μ m) to temperatures of several hundred eV. The heated plasma is ionized and emits a short burst of x-ray radiation that is detected with an x-ray framing camera. The hot electrons are characterized from the measured hard x-ray bremsstrahlung emission. Figure 140.72(b) shows the measured x-ray flash time for different ablator materials with smoothing by spectral dispersion (SSD) (squares) and without SSD (circles). An earlier flash time was measured with a plastic ablator, indicating that a stronger shock was produced in the laser–target interaction. The data show that turning SSD off shortened the flash time by ~ 50 ps for most

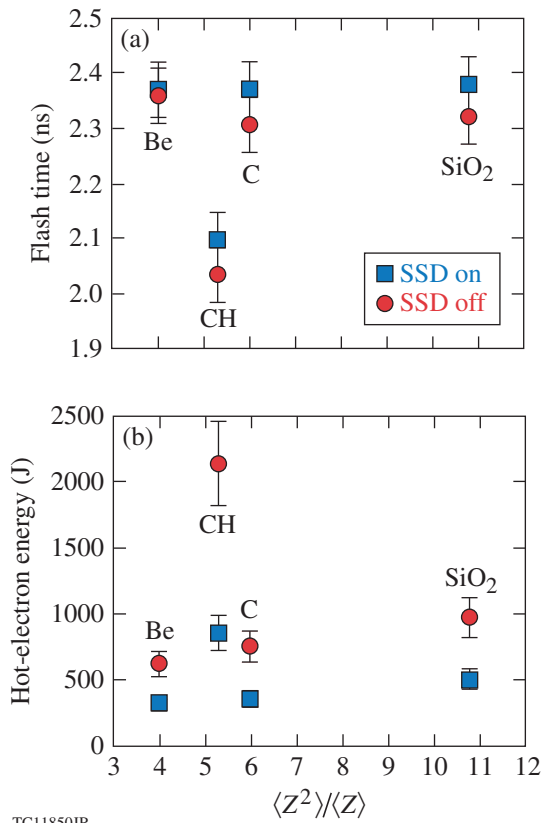


Figure 140.72 (a) Measured x-ray flash time from the convergent shock wave from the target center for different ablator materials with smoothing by spectral dispersion (SSD) (squares) and without SSD (circles). An earlier flash time was measured with a plastic ablator, indicating that stronger shocks were produced. There is also an indication that turning SSD off increased the shock strength. (b) Measured hot-electron energy deposited in the target for different ablator materials. More hot electrons are generated with a plastic ablator and SSD turned off.

of the different ablators. This indicates that stronger shocks were produced when SSD was turned off. Figure 140.72(b) shows the measured hot-electron energy for the different ablator materials. For each of the materials, about a factor of 2 more hot electrons were produced without SSD. The plastic ablator produced, by far, the most hot electrons and more than 2 kJ of hot-electron energy without SSD, which corresponds to a conversion efficiency of ~9% of the total laser energy. This is more than a factor of 2 more than what is produced in SiO₂ and almost a factor of 3 more than in carbon, which is very close in effective atomic number to plastic. Simulations are underway to study the effect of the ablator material to

understand why plastic produced a stronger shock and more hot electrons.

Creation and Measurement of Novel High-Pressure Electride States of Matter

Principal Investigator: T. Ma (LLNL)

Co-investigators: A. Pak, B. Bachmann, S. LePape, and T. Doeppner (LLNL)

Density functional theory (DFT) simulations predict a new material phase in highly compressed matter, where valence electrons, instead of becoming delocalized, actually bunch up in interstitial pockets. This creates an electron lattice co-existing within the ion lattice. This experiment used x-ray Thomson scattering to search for the existence of this electride phase by probing the lattice spacing that corresponds to the electrified.

Magnesium foils, 100 μm thick, were shock compressed to 5 to 8 Mbar (Fig. 140.73) using a single-sided ramp drive utilizing nine OMEGA beams with up to a total of 800 J of energy. The shocked samples were probed using Zn He_α x rays (8.9 keV) at a time corresponding to peak pressure. By varying the scattering angle between the shots, the static structure factor was directly probed, where the scattering profile would show pronounced peaks at low-*k* values because of the additional reflections and interferences of the electride lattice. Excellent scattering data were acquired at the various phases of Mg reached under varying shock conditions; however, preliminary data analysis does not seem to show scattering variations that would immediately indicate the existence of electrifieds. Further data analysis is required.

Ablative Richtmyer–Meshkov Experiments

Principal Investigator: D. Martinez (LLNL)

The ablative Richtmyer–Meshkov (RM) instability driven from laser imprinting in the presence of a phase inversion was explored on the 60-beam OMEGA Laser System. Figure 140.74 shows the experimental configuration. Planar 30- and 50-μm-thick CH targets were directly driven with three UV beams using a 3-ns square pulse shape, a total energy of ~0.7 kJ, and a laser intensity of ~5 × 10¹³ W/cm². Initial target modulations were imposed by laser imprinting, using a beam with a special 2-D phase plate with a modulation wavelength of ~30 μm and timing advanced by ~200 ps relative to the other drive beams, which had regular OMEGA distributed phase plates (DPP’s). The growth of

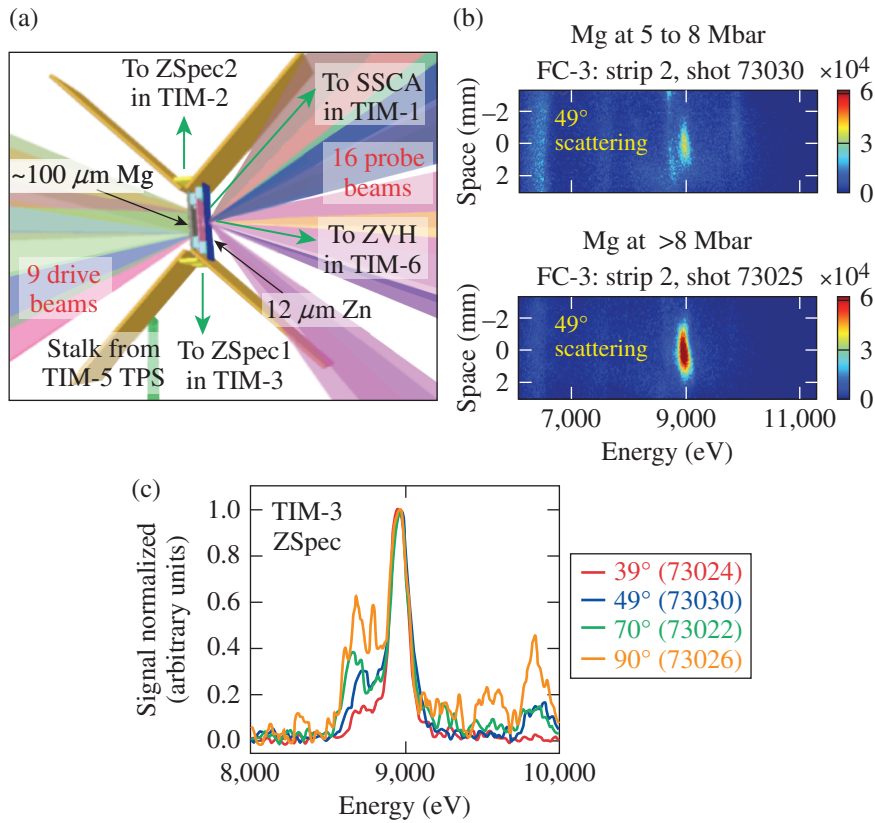
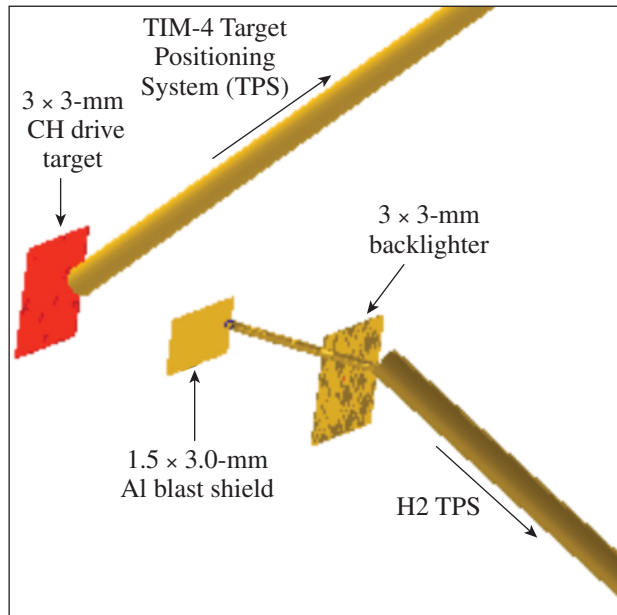


Figure 140.73

(a) Experimental configuration. (b) Raw scattering data taken at 49° for Mg compressed to between 5 to 8 Mbar [face-centered cubic (fcc) phase] and >8 Mbar [simple hexagonal (sh) phase]. (c) Comparison of scattering profiles for four shots taken at various scattering angles for Mg shock compressed to fcc (5 to 8 Mbar) phase. TIM: ten-inch manipulator; SSCA: x-ray streak camera; TPS: target positioning system.

U1807JR



U1803JR

Figure 140.74
Experimental configuration for FY14 ablative Richtmyer–Meshkov experiments.

target modulations was measured with gated x-ray radiography using samarium (~1.8-keV) and tantalum (~2.2-keV) backlighters, 10- μm spatial resolution, and 80-ps temporal resolution. The backlighters were driven with a 2-ns square pulse shape at $\sim 3 \times 10^{14} \text{ W/cm}^2$ using seven additional UV beams. Figure 140.75(a) shows a typical radiograph of the RM instability for a shot using laser imprinting. For comparison, foils with preimposed modulations were also used to observe the differences between the RM instability from preimposed modulations and the data shown in Fig. 140.75(b). Although the modulations were not purely orthogonal, the power spectrum shows that the modulations are sufficiently separated [Fig. 140.75(c)]. Figure 140.76 shows that the imprinted and preimposed modulations follow the same growth trajectory, suggesting that imprint, in the observed case, had little to no influence on the RM instability after the initial seed. Simulations using the *CHIC* code from CEA and the *DRACO* code from LLE disagree with the trajectory of the modulations; one possible explanation is that the codes overpredict the ablation velocity. Investigation into the disagreement is ongoing.

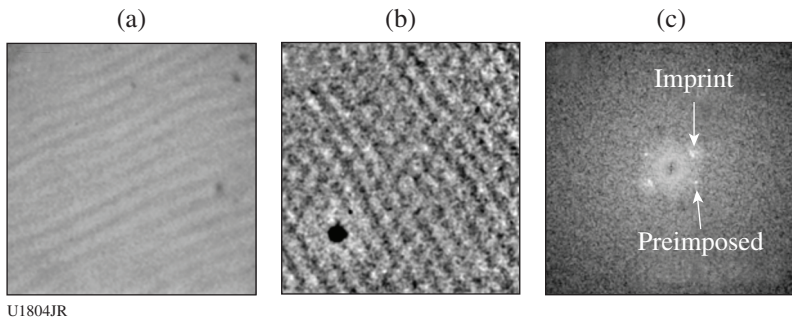


Figure 140.75
Data showing (a) imprint modulations in 30- μm -thick foil at 0.8 ns; (b) imprint and preimposed growth at 0.8 ns in a 50- μm -thick CH target; and (c) the Fourier power spectrum of (b).

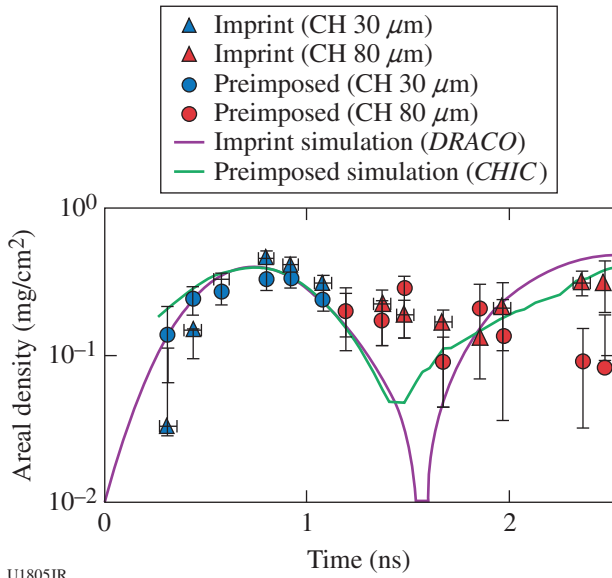


Figure 140.76
Richtmyer–Meshkov growth for 30- μm - and 80- μm -thick CH foils for imprinted (triangles) and preimposed (circles) modulations. Shock breakout is expected at 0.9 ns for 30- μm -thick foils and 2.4 ns for 80- μm -thick foils.

Thermonuclear Reactions in Stellar Plasmas

Principal Investigator: D. McNabb (LLNL)
Shot Principal Investigator: M. Gatu Johnson (MIT)

Two distinct Laboratory Basic Science (LBS) “Stellar Rates” Campaigns were fielded in FY14, in conjunction with a related NLUF effort and with extensive collaboration between LLNL, MIT, LLE, and LANL. The main goals of the first campaign were to study stratification (between T and ^3He) and nuclear product spectra in T^3He implosions (with trace D in the fuel). Understanding the impact of stratification on implosion yields is a key step toward using the implosion platforms developed in inertial confinement fusion (ICF) research to measure cross sections relevant to stellar and big-bang nucleosynthesis. $\text{T}^3\text{He}(\text{D})$

is an ideal fuel mixture to study stratification because of the many measurable nuclear yields produced from these implosions ($\text{T}^3\text{He-p}$, $\text{T}^3\text{He-d}$, $\text{D}^3\text{He-p}$, DT-n , TT-n). Trace quantities of D are not expected to significantly impact stratification between the T and ^3He majority ions. Although detailed data analysis and post-shot simulations are in progress, Fig. 140.77 shows preliminary measured $\text{D}^3\text{He}/\text{DT}$ yield ratios (points with error bars) for these shots as a function of partial ^3He pressure in the fuel. Three different fill mixtures were shot to test a theoretical prediction that stratification effects will cancel out in T^3He fuel at 90:10 T: ^3He (Ref. 45). Also shown in the figure is the pre-shot simulation of the $\text{D}^3\text{He}/\text{DT}$ ratio, from hydro-simulations (ARES) that do not consider possible stratification effects. Stratification between T and ^3He would show up as a deviation from the predicted ratio. Pending post-shot simulations, the preliminary indication is that stratification effects are small in these experiments.

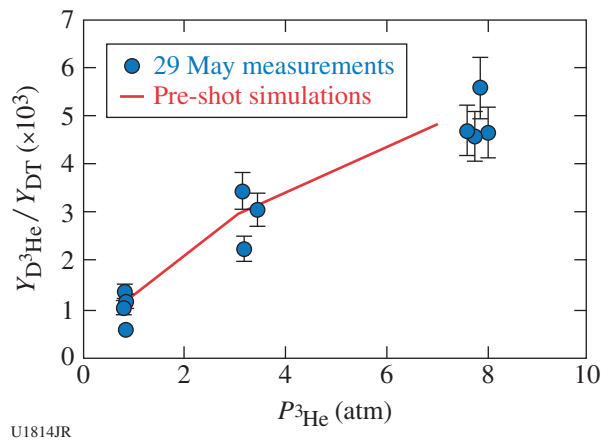


Figure 140.77
Preliminary measured D^3He -to- DT yield ratios as a function of partial ^3He fill pressure in the capsule (points with error bars). Also shown is the ratio predicted in pre-shot simulations (red line) assuming no stratification of the T and ^3He .

In the second experiment, the γ rays from the p + D fusion reaction were measured for the first time in an ICF plasma, at a center of mass (Gamow peak) energy of ~ 16 keV. This reaction is relevant to astrophysics. In particular, during big-bang nucleosynthesis, it produces ${}^3\text{He}$ (at particle energies ≥ 100 keV), and in protostars and brown dwarfs, it is the primary source of nuclear energy (at particle energies < 1 keV). The low energy of this γ (5.5 MeV) necessitated the use of the new gas Cherenkov detector (GCD)-3 detector by LANL. Excellent data were acquired for the p + D reaction, highlighted in Fig. 140.78. These shots also measured the DD- γ for the first time in ICF, which is the primary source of background for the p + D measurement.

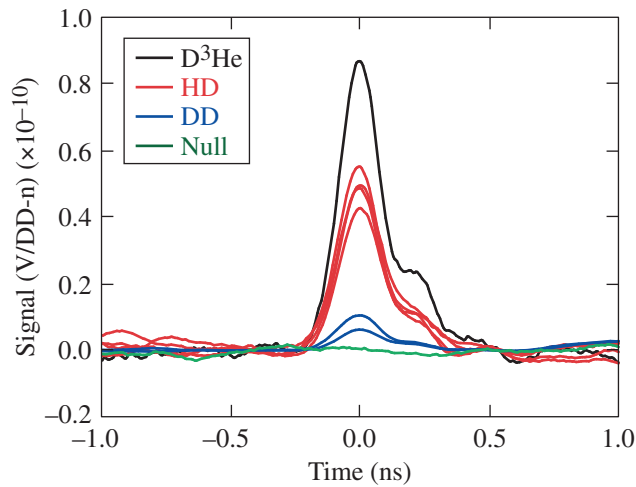


Figure 140.78
Cherenkov detector signals for the p + D experiments, showing four shot types: D^3He (detector calibration, black), HD (primary signal, red), DD (background, blue), and null (background, green). Excellent p + D fusion data were acquired for the first time.

Measurements of Charged-Particle Stopping Power on OMEGA EP

Principal Investigator: S. Nagel (LLNL)
Co-investigator: A. Zylstra (MIT)

Calculations of charged-particle energy loss in ICF-relevant plasma conditions still depend on untested theories. To address the need to validate these theories, a platform is being developed on OMEGA EP to measure charged-particle energy loss. Strongly coupled or fully degenerate conditions are difficult to obtain, but warm-dense-matter (WDM) plasmas that have temperatures of several tens of eV and approximately solid densities (10^{22} to 10^{23}) are well within the moderately coupled and degenerate regimes.

The experimental schematic is shown in Fig. 140.79. A short-pulse beam is used to generate energetic protons via the target-normal sheath acceleration (TNSA) mechanism to probe a warm foam target. The foam target is heated by x rays using a halfraum driven by three long-pulse UV beams. Compared to previous campaigns on OMEGA EP, this method showed an improvement of the proton-beam smoothness, better pointing of the proton beam through the material, and reduced cross-talk between the heating and proton probing. This, therefore, significantly advanced the platform, and new measurements are planned.

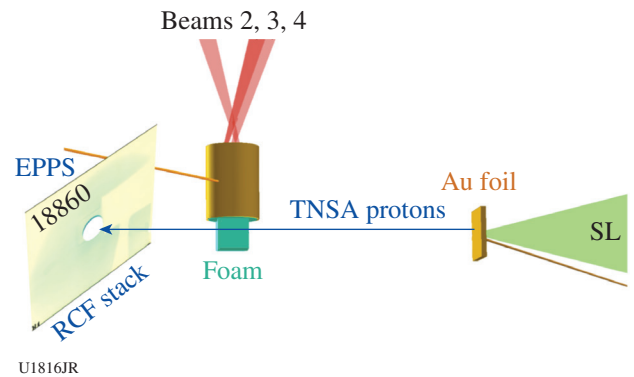


Figure 140.79
Experimental schematic. One OMEGA EP short-pulse laser beam is used to create the probing protons, whose proton-beam profile and spectra were characterized by a new combination of both radiochromic film and the electron-proton-positron spectrometer (EPPS). The other three beams are used to heat the foam target. RCF: radiochromic film; SL: sidelighter.

Radiation Hydrodynamics of Double Ablation Fronts

Principal Investigator: P. M. Nilson (LLE)
Co-investigators: M. Lafon and R. Betti (LLE)

Laser-driven ablator dynamics in moderate-Z materials provide a basic test for radiation-hydrodynamic model predictions in a regime where electron and radiation transport are dynamically significant. This series of experiments studied directly driven ablator dynamics in brominated plastic (CHBr) targets where double ablation fronts are known to form. Ablation is driven at the first front by an electron heat flux and at the second front by a radiative heat flux. The system is optically thin in the outer ablation front and close to the corona. The system is optically thick at the inner ablation front and in the plateau region. Here, radiation and matter are almost in equilibrium and the radiative energy flux is described by a thermal heat wave. Combining streaked x-ray radiography with self-emission imaging allows one to track these regions as a function of time for comparison with model predictions.

The experiments were carried out on the OMEGA EP Laser System. CHBr (6 at. %) targets were driven with a 2.5-ns square pulse at focused intensities of 10^{14} W/cm². Target trajectories and density profiles were measured using time-resolved x-ray radiography based on a laser-driven Ti x-ray source and a one-dimensional slit imager coupled to an x-ray streak camera. With appropriate filtration, emission from the hot coronal plasma was simultaneously imaged. An example radiograph for a 20- μ m-thick target with superposed x-ray self-emission imaging is shown in Fig. 140.80. The data show x-ray transmission and coronal emission consistent with a density plateau where the double ablation front forms. Tracking the location of the ablation fronts and measuring the hydrodynamic efficiency of the driven target provide a novel and direct test for equation-of-state and opacity model predictions. Detailed analysis of these data is underway.

Astrophysical Collisionless Shock Experiments with Lasers (ACSEL) on OMEGA EP

Principal Investigator: H.-S. Park (LLNL)

Shot Principal Investigator: C. Huntington (LLNL)

The ACSEL collaboration is studying high-velocity plasma flow interactions and the role of self-generated or amplified magnetic fields in such systems. Study of these phenomena is essential to understanding a range of astrophysical systems, including gamma-ray bursts, supernova remnants, and young stellar objects. The FY14 experiments using OMEGA EP expanded on the collisionless shock platform common to ACSEL (LBS) and MagShock (NLUF), with the former concentrating exclusively on plasmas without externally applied magnetic fields. Irradiating a pair of opposing planar targets with 2.2 kJ (OMEGA EP), counter-propagating flows are created, each with bulk velocity near 1000 km/s. The flows interact near the midplane between the targets, where the interpenetrat-

ing plasma is susceptible to a range of instabilities, including the two-stream and Weibel instabilities.

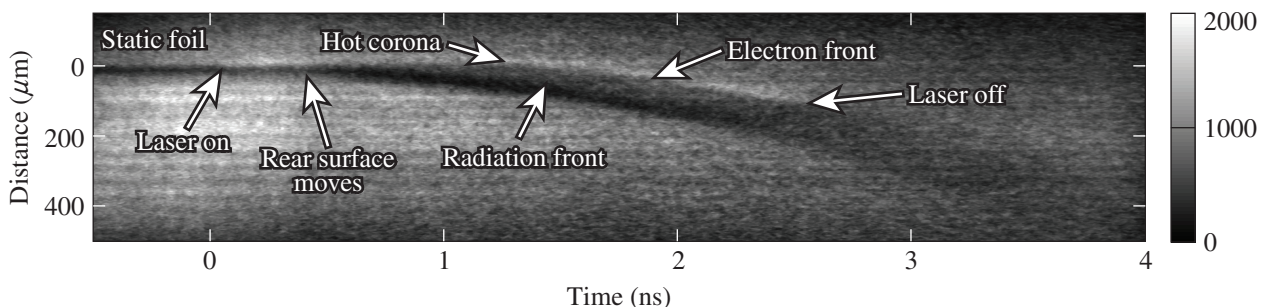
The FY14 campaigns studied the effect of varying the target material, including the effect of collisional flow from higher-Z target materials. Figure 140.81 compares data obtained for CH₂ (the same as most of the previous studies), Al, and Cu targets. The central magnetic-field advection feature^{46,47} is very different among these target types. The data show that the two horizontal features, thought to be associated with piled-up magnetic fields from the Biermann battery at the laser spot, move apart over time, which is different from collisionless flow experiments where the two features stay at the same place. This is likely caused by pressure buildup in the interaction region, which pushes the features apart. Both *FLASH* and *OSIRIS* simulations show qualitative agreement with the experimental data. On the other hand, the actual size of the interaction region remains narrow, and the fact that the two plates are still horizontal indicates that the turbulence is probably not very developed. This implies that turbulence in the collisional flow plays an important role in the formation of the magnetic field. Further experiments are planned in FY15.

Fast Ignition Using Elliptical-Tip Cone-in-Shell Targets

Principal Investigators: P. K. Patel and F. Pérez (LLNL)

Co-investigators: H. Sawada (University of Nevada, Reno); W. Theobald and A. A. Solodov (LLE); L. C. Jarrott and F. N. Beg (University of California, San Diego); M. S. Wei (General Atomics); and A. Link, Y. Ping, and H. S. McLean (LLNL)

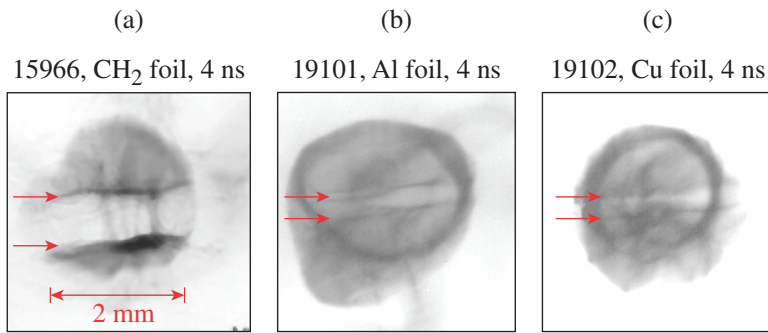
The fast-ignition (FI) approach to inertial confinement fusion has the potential to achieve higher energy gain compared to central hot-spot-ignition schemes. Fast ignition uses a separate short-pulse ignition laser to locally heat the fuel core near the time of peak compression. This ignition laser is focused inside the tip of a



E23744JR

Figure 140.80

Streaked x-ray radiograph of double ablation front formation in a 20- μ m-thick CHBr (6 at. %) target driven with a 2.5-ns square pulse at focused intensities of 10^{14} W/cm². The ablation front driven by radiative energy flux propagates into the target ahead of the electron-driven ablation front.

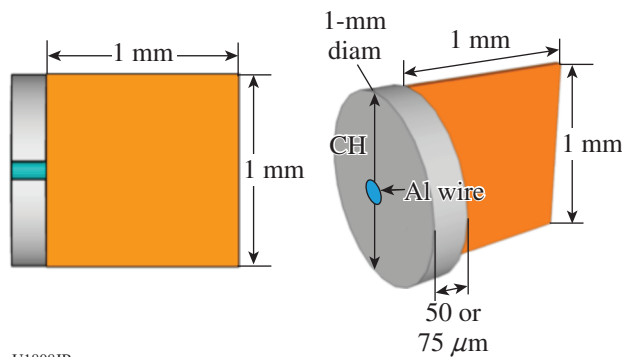


U1806JR

Figure 140.81
Comparison of magnetic fields from interpenetrating high-velocity flows. The higher-Z targets create colliding flows that affect the magnetic-field advection generated by the Biermann battery from the target surface. This indicates that turbulence in the collisional flows plays an important role in the formation of the magnetic field.

re-entrant gold cone and accelerates a large number of high-energy electrons. The efficiency of heating the fuel to thermonuclear conditions can be greatly increased if the electrons accelerated from the laser-interaction region can be guided to the dense fuel.

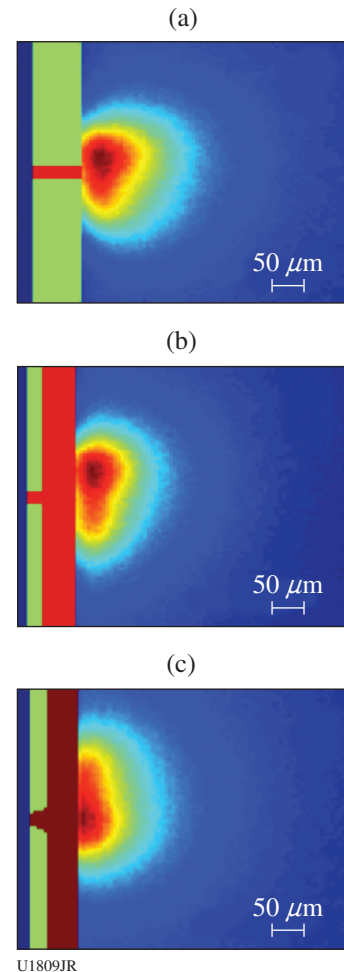
This year's experiments investigated electron-beam guiding using resistivity discontinuities through structured material interfaces. The OMEGA EP picosecond laser was focused on a slab of plastic containing short aluminum wires of various shapes. Laser-generated electrons tend to stay localized inside the wire because of magnetic fields generated along the resistivity discontinuity. As illustrated in Fig. 140.82, a copper slab was attached at the back of the CH/Al foil to detect the location of the electrons exiting the foil. Wires of three formats were used: traversing the whole slab ("long"), traversing only a short portion of the slab ("short"), or in the shape of an ellipsoid. The latter have been predicted to provide better focusing characteristics, in the manner of elliptical mirrors in optics. The electrons passing through the Cu foil induce Cu- K_{α} x-ray emission, which was imaged using the spherical crystal imager (as shown in Fig. 140.83). The presence of the wires clearly produced structure in the electron beam, showing that some guiding is occurring. In this experiment, however, the ellipsoids were not proven to be more



U1808JR

Figure 140.82
Schematic of the targets.

efficient than straight wires. A simulation effort is benchmarking the current models to these results and extending the models to ignition-scale situations. It is expected that the guiding effects will be enhanced in full-scale scenarios.



U1809JR

Figure 140.83
Cu- K_{α} images, reflecting the shape of the electron beam through the Cu foil. The green blocks correspond to plastic and the red blocks correspond to Al. The (a) long wire; (b) short wire; and (c) ellipsoid structure.

Structure and Equation of State of Solid and Superionic Warm Dense Water

Principal Investigator: J. R. Rygg (LLNL)

Shot Principal Investigators: F. Coppari and M. Millot (LLNL)

The structure and equation of state of solid and superionic warm dense water at the core conditions of Uranus and Neptune were investigated to explore a proposed superionic phase, essentially a solid lattice of oxygen ions surrounded by fluid-like diffusing protons. Its existence in the deep interiors of icy giant planets would have a dramatic impact on their internal structure and evolution.

The experiments on the 60-beam OMEGA Laser System employed new laser dynamic compression techniques, novel liquid-cell targets, and advanced diagnostics, including both optical diagnostics and x-ray diffraction. Multishock compression in these experiments squeezed initially liquid water into solid and superionic ices at pressures of several megabars, while keeping the temperature below 0.5 eV. Data were obtained using streaked optical reflectivity and pyrometry and interferometric Doppler velocimetry (VISAR), as well as x-ray diffraction. Ongoing analysis of the recently obtained x-ray diffraction data will provide unprecedented insight on the equation of state and structure of solid and superionic megabar water ices in the portion of phase space shown in Fig. 140.84.

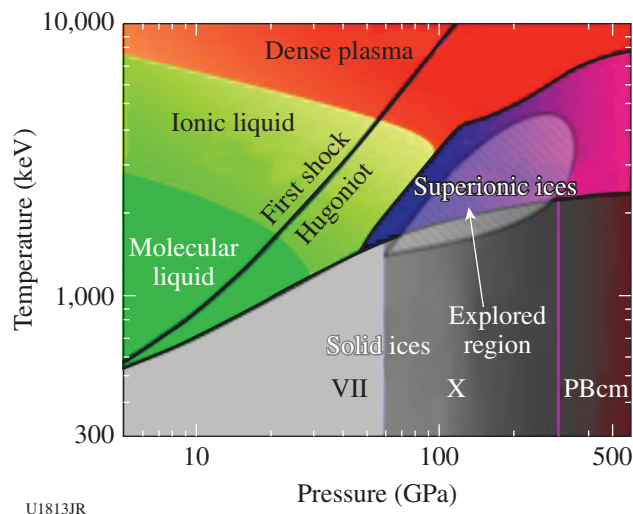


Figure 140.84

Pressure-temperature phase diagram of warm dense water, showing the region explored with multishock compression of liquid water using ultrafast optical diagnostics and x-ray diffraction on the OMEGA Laser System. PBcm: a particular type of crystal structure, characteristic of high-density water ices.

Spectroscopy of Neutrons Generated Through Nuclear Reactions with Light Ions in Short-Pulse Laser Interaction Experiments

Principal Investigators: C. Stoeckl, U. Schroeder, and V. Yu. Glebov (LLE)

The experimental objective of this project is to study nuclear reactions in light ions by measuring the spectrum of neutrons generated in short-pulse laser-interaction experiments and compare it with simulated spectra based on the published cross sections.

Planar targets are irradiated with one short-pulse beam focused at the target's front surface. Charged particles from the back side of the target create neutrons and charged particles through nuclear reactions in a second converter target placed closely behind the primary interaction target. The spectrum of the neutrons generated in the converter target is measured using a three-channel scintillator photomultiplier-based neutron time-of-flight (nTOF) detector system. Charged-particle detectors are used to measure the spectra of the primary particles.

The previous experiments in FY13 with CD primary and CD secondary targets resulted in neutron spectra showing a clear DD fusion neutron peak. For these experiments a pre-plasma was created on the front side of the primary target using a 100-J, 100-ps UV laser pulse, which was fired 0.5 ns before the main IR short pulse. This pre-plasma significantly reduced the number and energy of charged particles on the front surface of the primary target and significantly improved the signal-to-background ratio.

Two shot days were allocated for these experiments in FY14. On the first day LiD secondary targets were used with the reduced background primary CD target developed in FY13. Unfortunately no DT neutrons were recorded from the tritium generated in Li breakup reactions. Preliminary analysis of the data indicates that the cross sections for the Li breakup reactions are too small to generate enough tritium, given the flux and spectrum of the primary ions and the geometry of the experimental setup.

On the second day a neutron pickup reaction in Be [$\text{Be}^9(\text{d},\text{t})\text{Be}^8$] was chosen to produce the tritium, which then generated the DT fusion neutrons. The theoretical cross sections of this reaction reach ~ 150 mb above 1-MeV deuteron energy. The experimental values reported in the literature are varying significantly between ~ 20 mb and 200 mb. For these experiments, a Be foil of ~ 50 - to 100 - μm thickness was attached in front of the 2-mm-thick CD secondary target.

Figure 140.85 shows the nTOF spectra from the BeCD secondary target compared to the results from a CD secondary target.

With the BeCD secondary target, the neutrons are recorded much earlier compared to the CD secondary, indicating a higher energy. The short signal seen before -50 ns in the nTOF spectrum is caused by the x rays from the laser interacting with the primary target and can be used as a timing reference. Using the x-ray timing reference, the energy of the neutrons can be estimated to be ~ 2.5 MeV for the CD foil, typical for DD fusion neutrons, and ~ 4.3 MeV for the BeCD target. The ~ 4.3 -MeV neutron emission is consistent with a $\text{Be}^9(\text{d},\text{n})\text{B}^{10}$ nuclear reaction. Few data have been published about this reaction. Typical cross sections shown in the literature are of the order of ~ 100 mb. A more-detailed analysis of this data is in progress.

FY14 LLNL OMEGA Experimental Programs

R. F. Heeter, K. B. Fournier, K. Baker, M. A. Barrios Garcia, L. Bernstein, G. Brown, P. M. Celliers, H. Chen, F. Coppari, D. E. Fratanduono, C. Huntington, A. Lazicki, R. Kraus, T. Ma, D. Martinez, D. McNabb, M. Millot, A. Moore, S. Nagel, H.-S. Park, P. K. Patel, F. Pérez, Y. Ping, B. Pollock, J. S. Ross, J. R. Rygg, R. Smith, G. W. Collins, O. L. Landen, A. Wan, and W. Hsing (LLNL); and M. Gatu Johnson and A. Zylstra (MIT)

In FY14, LLNL's High-Energy-Density (HED) Physics and Indirect-Drive Inertial Confinement Fusion (ICF-ID) Programs

conducted several campaigns on the OMEGA and OMEGA EP Laser Systems, as well as campaigns that used the OMEGA and OMEGA EP beams jointly. Overall, these LLNL programs led 324 target shots in FY14, with 246 shots using only OMEGA, 62 shots using only OMEGA EP, and 16 joint shots using OMEGA and OMEGA EP jointly. Approximately 31% of the total number of shots (62 OMEGA shots, 42 OMEGA EP shots) supported the ICF-ID Campaign. The remaining 69% (200 OMEGA shots and 36 OMEGA EP shots, including the 16 joint shots) were dedicated to experiments for the HED Campaign. Highlights of the various HED and ICF campaigns are summarized in the following reports.

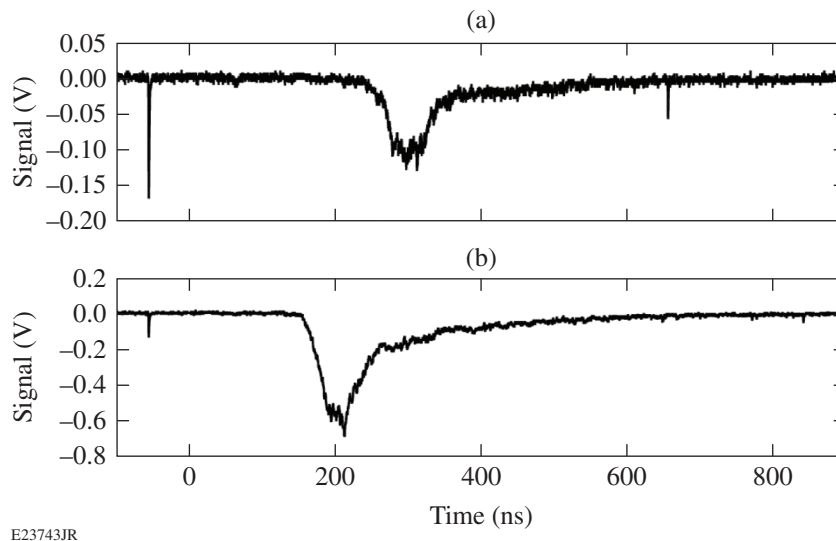
Indirect-Drive Inertial Confinement Fusion Experiments

Thomson-Scattering Measurements from Laser-Driven Gold Spheres

Principal Investigator: J. S. Ross

Co-investigators: R. F. Heeter and M. Rosen (LLNL); and D. H. Froula (LLE)

In the FY14 AuSphere and GasCoSphere Campaigns, we performed experiments using high-Z-coated spheres illuminated uniformly in direct-drive geometry to investigate atomic physics models and radiative properties of the laser-spot plasma relevant to inertial confinement fusion (ICF) indirect-drive-ignition hohlraum plasmas. Bare Au and gas-covered Au spheres (shown in Fig. 140.86) were both investigated.



E23743JR

Figure 140.85

Neutron time-of-flight signals from the experiments with (a) CD primary and CD secondary and (b) BeCD secondary targets. The arrival time of the neutrons shifts significantly earlier with the BeCD, indicating a change in the average neutron energy from 2.45 to ~ 4.3 MeV.

The laser irradiation of 1×10^{14} to 10^{15} W/cm² is similar to the intensities found in National Ignition Campaign (NIC) hohlraums. The gas-covered Au sphere experiments use a gas fill of 1 atm of propane or 1 atm of a 70/30 mix of propane and methane to achieve initial electron densities of 7.5% and 6.0% of the critical density, respectively, of the 3ω drive beams. The plasma temperature and density at various radial positions in the blowoff plasma are characterized using optical Thomson scattering. The probe beam was aligned at various radial locations ranging from 100 to 300 μm from the target surface for Thomson-scattering characterization of the low-density plasma blowoff. The laser beams used either a 1-ns square laser pulse or a two-step laser pulse (1-ns square foot, 1-ns square peak) designed to reduce the shock produced by the gas-bag window.

The electron temperature and density, the plasma-flow velocity, and the average ionization state are measured by fitting the theoretical Thomson-scattering form factor to the observed

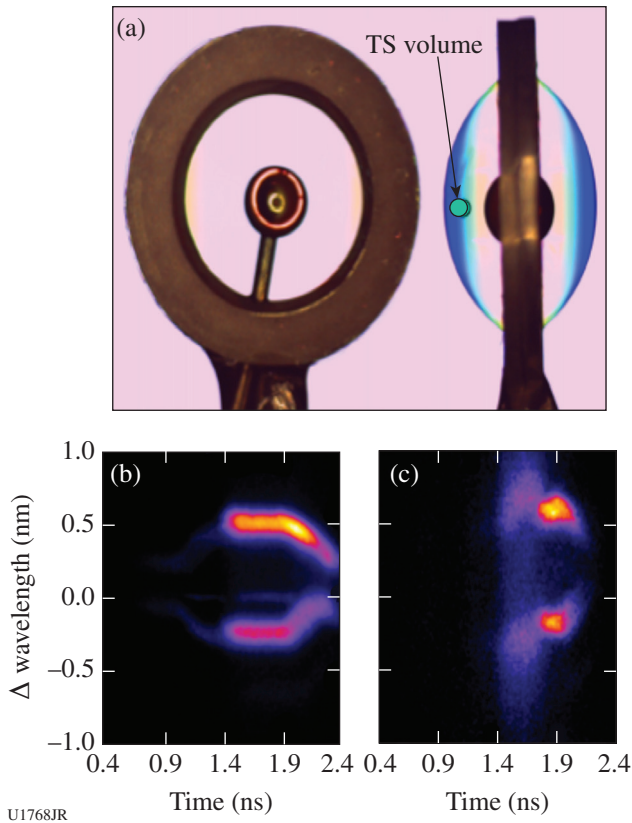


Figure 140.86
 (a) A 1-mm-diam Au sphere centered in a 2.6-mm-diam gas bag. The gas bag is filled with 1 atm of propane or a mix of methane and propane to achieve different initial electron densities. The location of the Thomson-scattering (TS) volume is shown. (b) TS spectrum as a function of time for Au sphere. (c) TS spectrum as a function of time for gas-covered Au spheres.

data. Examples of the Thomson-scattering data from ion-acoustic fluctuations are shown in Fig. 140.86 for both target types. The measured data are then compared to post-shot simulations with different atomic physics and electron-transport models. The different models predict different electron temperatures for the experimental conditions; sample results are shown for the bare Au spheres in Fig. 140.87.

The simulation with the XSN nonlocal model most closely reproduces the temperatures measured during the experiment. The XSN model with a flux-limited transport model using a flux limiter of 0.05, previously used to simulate high-Z hohlraums, predicts an electron temperature significantly higher than measured. A detailed analysis of the gas-covered sphere data is currently underway, and a comparison of Thomson-

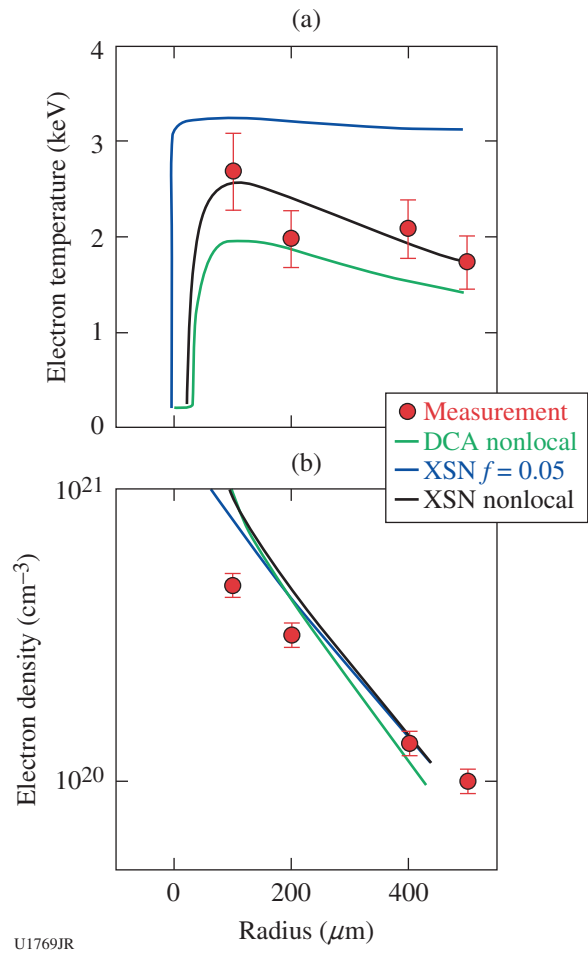


Figure 140.87
 For bare Au spheres, the (a) measured electron temperature and (b) electron density are compared to post-shot simulations using the detailed-configuration accounting (DCA) nonlocal model (green line), the XSN flux-limited model with a flux limiter of 0.05 (blue line), and a nonlocal heat-transport model (black line) for an intensity of 5×10^{14} W/cm².

scattering data, Dante absolute x-ray flux measurements, and x-ray spectroscopy to simulations will be used to further validate the atomic physics models employed in these simulations.

Cryogenic Cell Measurements of the Viscosity of Rippled Shocks

Principal Investigator: P. M. Celliers

The Shock Viscosity Campaigns began as an effort to probe the decay of rippled shocks in National Ignition Facility (NIF) ablator materials as a means of assessing whether the rippled shock response was inviscid or showed evidence of more-complicated viscous behavior. As part of this effort, attempts were initiated to field a planar cryogenic platform compatible with the viewing axis of the 2-D VISAR (velocity interferometer system for any reflector) using the OMEGA high-resolution velocimeter (OHRV). The planar cryogenic platform addresses an important surrogacy issue associated with the CapSeed Campaigns. In all prior campaigns using room-temperature targets, a layer of transparent polymethyl methacrylate (PMMA) was used as the surrogate for the fuel layer. The shock-impedance difference between PMMA and ICF ablators is much less than for DT ice or liquid D₂, so any issues associated with the deep release of the ablator into the fuel are not captured accurately in the room-temperature PMMA-based platform. For this reason, the cryogenic platform is expected to produce more-definitive data sets for the level of ablator nonuniformities transmitted into the fuel. The initial cryogenic shots of the Shock Viscosity Campaigns (Figs. 140.88 and 140.89) were aimed at establishing a baseline data set for the response of various ablators releasing into liquid deuterium. A single baseline dataset on glow-discharge polymer (GDP) was collected during the initial campaign, with other targets leaking because the GDP samples stress-fractured at cryogenic temperatures. Based on this experience, improvements were made to the target design and a second campaign produced several more datasets on high-density carbon (HDC) and Be ablator samples. The stress-fracturing issue with GDP remains to be solved.

Velocity Fluctuations in Doubly Shocked Glow-Discharge-Polymer Ablators

Principal Investigator: P. M. Celliers

The CapSeed Campaign in FY14 continued our study of GDP, the plastic polymer material used in NIF ablators. The primary goal was to study the response of GDP at the second shock level, by observing the shock-front nonuniformities shortly after a second shock (launched behind the initial shock)

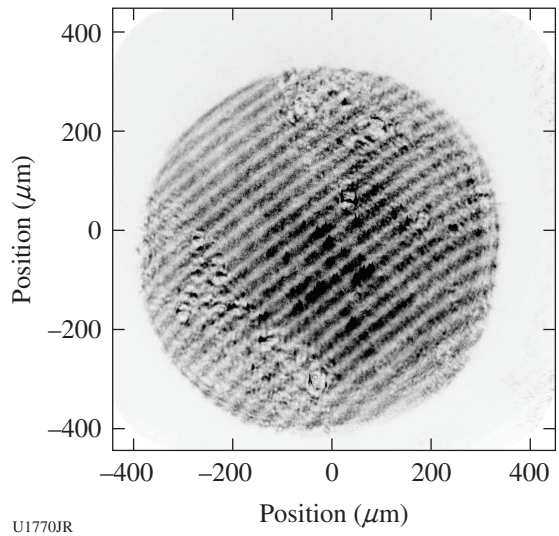


Figure 140.88 Interferogram from the first cryogenic test of a glow-discharge polymer (GDP) ablator releasing into liquid deuterium.

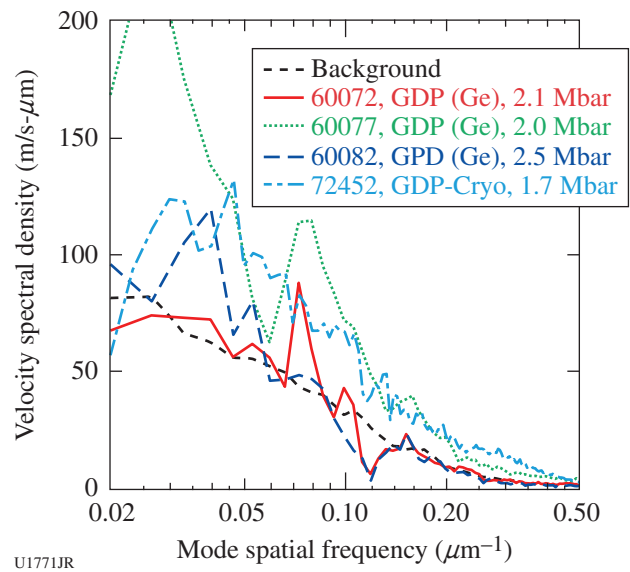


Figure 140.89 Velocity-fluctuation spectra measured for GDP on the first cryogenic test of GDP using the OMEGA high-resolution velocimeter (OHRV) diagnostic, in comparison with data from warm platform tests with PMMA as a surrogate for the fuel. Velocity-fluctuation spectra are very similar for the two platforms.

had overtaken the first. Several shots were devoted to tuning the two-shock drive by adjusting the timing delay between two groups of drive beams. The tuning study was completed and two preliminary data sets were recorded (Figs. 140.90 and 140.91). These initial results did not reveal a level of nonuniformity significantly different from the nonuniformity levels that

have been recorded at the first shock level in the GDP material. The current series has laid the foundation for further data collection of GDP using the two-shock drive in a future campaign.

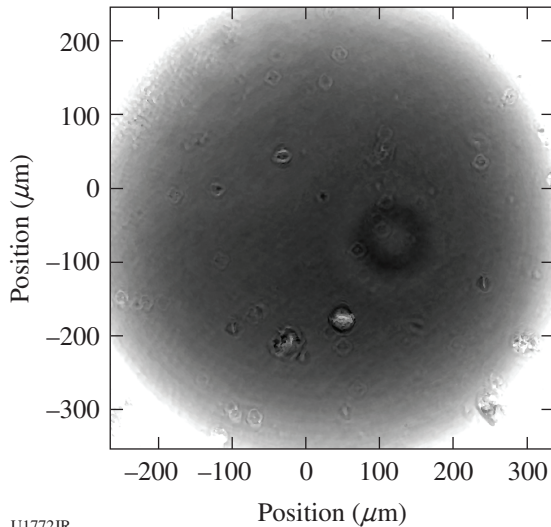


Figure 140.90
Gray-scale representation of the shock-front velocity in a GDP sample double-shocked to ~7 Mbar. The large ripple disturbance originates from a localized defect on the ablation surface; the smaller localized disturbances originate from dust particles trapped at the GDP-PMMA interface during target assembly.

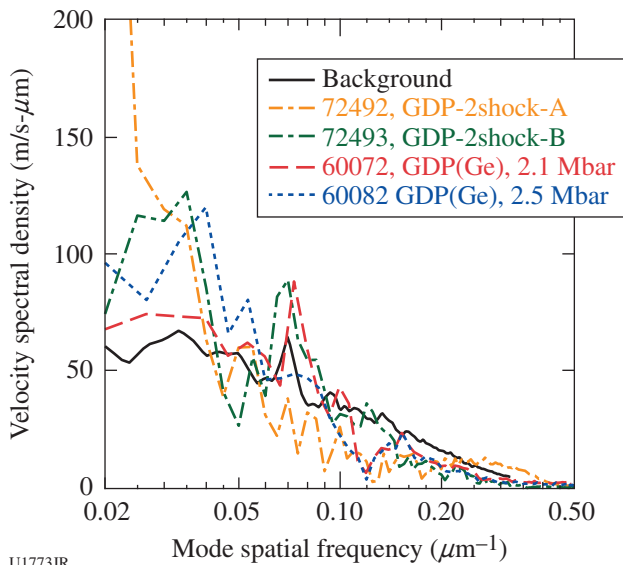


Figure 140.91
Velocity fluctuation spectra measured for GDP on two double-shock GDP experiments compared with earlier single-shock tests. Spectra have had the background subtracted. The background level is shown for comparison.

Shock-Release Isentrope Measurements of ICF-Relevant Materials

Principal Investigator: D. E. Fratanduono

To address concerns regarding uncertainties in the release isentropes of inertial confinement fusion (ICF) ablator materials into low-density gas, experiments were performed to measure the release of glow-discharge polymer (GDP) and CH into methane gas at gas densities comparable to an ICF capsule, to examine the momentum transfer in this low-density kinetic regime. The experiment measured the shock velocity in the GDP prior to shock breakout and the shock transit time through a known methane gas density (0.25 to 1.0 atm). We then utilized a momentum transfer technique to extract $P-U_p$ data (the release isentrope). These experiments suffered unexpectedly from nonreproducible effects, which made it difficult to distill conclusions. On average, the shock velocity in the methane gas was anomalously low, suggesting that the equation-of-state model may be overpredicting the release state. Since the results were not consistently reproducible, future experiments will be required to examine this region of phase space in detail.

Platform Development for Measuring Charged-Particle Stopping in Warm Dense Plasmas

Principal Investigator: A. Zylstra (LLNL/MIT Collaboration)

The TransportEP-14A Campaign conducted shots to continue developing a stopping-power measurement platform using the short-pulse lasers on OMEGA EP. In this experiment, the sidelighter beam was used for proton isochoric heating of a warm-dense-matter sample, while the backlighter beam drove a planar foil, generating protons via target-normal sheath acceleration (TNSA) to probe the sample. For the backlighter-driven proton source, the uniformity of the proton beam was studied using source-only shots with a lower-energy drive (40J/1 ps) and smooth wafer targets of chemical vapor deposition (CVD) and Si, compared to standard Au. The proton beam images are shown in Figs. 140.92(a)–140.92(c). While the uniformity has improved over previous higher-intensity shots, modulations in the proton beam remain. The proton isochoric heating configuration sends a TNSA proton beam through a CH slab ($200 \times 200 \times 50 \mu\text{m}$), which is heated by proton energy deposition and characterized by x-ray backlighting. The backlighter was a uranium area backlighter, with data taken from 0.5 ns before the slab was heated until 1.5 ns after, as shown in Fig. 140.92(d). Preliminary data analysis suggests nonthermal expansion potentially driven by electromagnetic fields.

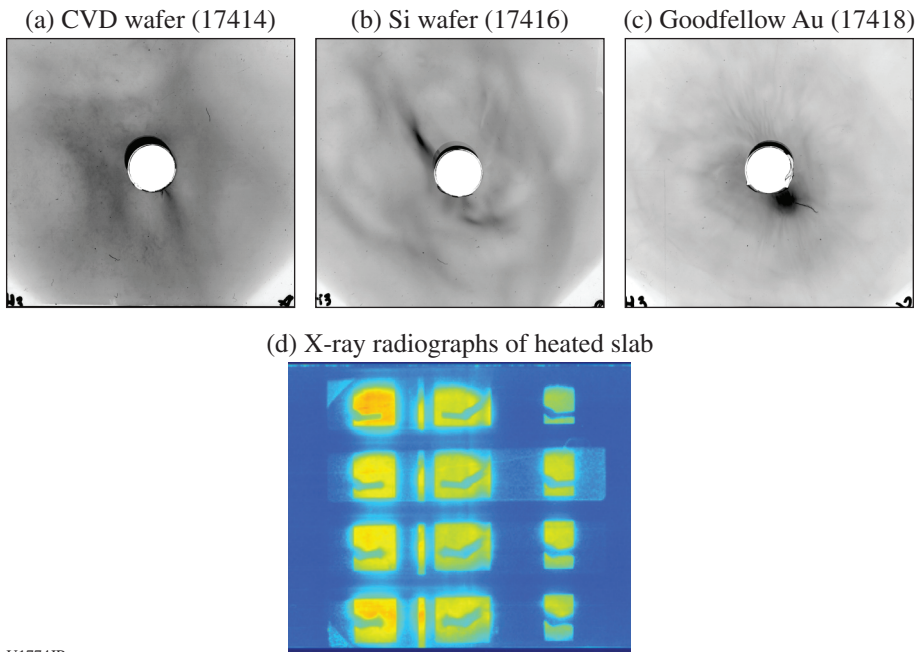


Figure 140.92
 [(a)–(c)] Proton source spatial distribution images for various foil targets and (d) x-ray radiography of proton-isochoric–heated slabs.

U1774JR

Measurements of the Opacity of Silicon in ICF Ablator Conditions

Principal Investigator: R. F. Heeter
 Co-investigators: G. V. Brown, C. Mauche, and B. Wilson

Continuing earlier ablator-opacity measurements, improved experiments were performed to measure the transmission opacity of hot silicon at $T \approx 70$ eV, $\rho \approx 0.2$ g/cm³ on OMEGA EP. At these temperatures and densities from 0.2 to 20 g/cm³, the Atwood number in Si-doped capsules has a strong sensitivity to the Si opacity. The FY14 experiment used a Be-tamped Si foil sample heated by 250-J, 250-ps impulses from two of the long-pulse beams. The sample plasma was characterized with dual-axis, simultaneous backlighting, both face-on and edge-on, using the two short-pulse beams in 10-ps mode. The backlighters were timed 200 ps after the peak of the heating impulse, as verified with the ultrafast x-ray streak camera. The edge-on radiograph measures density via the sample expansion from a known initial thickness (2.1 μm); the face-on measurement delivers Si ionization balance and transmission opacity data via absorption spectroscopy across the x-ray band from 1600 eV to 3000 eV. To probe the sample at higher density than previously, the edge-on radiography was improved by using a smaller backlighter and samples with improved planarity. The new technique delivered ~10-μm resolution, verified by radiographing a cold 10-μm Cu wire and also by discriminating the continuum absorption of the heated Si from the weaker

absorption of the underlying Be substrate. A target density of 0.2 g/cm³ was achieved by probing the Si plasma 200 ps after the peak of the heating pulse, when the silicon had expanded to 20 μm. As illustrated in Fig. 140.93, the Si measurements show absorption features from at least five of the L-shell charge states of Si, plus time-integrated self-emission from earlier in the heating pulse. This high-quality dataset will be analyzed and compared with the opacity models used for the NIF capsules.



U1775JR

Figure 140.93
 Space-resolved absorption spectrum obtained on OMEGA EP using face-on broadband spectroscopy from a Zn bremsstrahlung continuum backlighter. Photon energy increases from top to bottom; emission is dark and absorption is light. Multiple time-resolved absorption and time-integrated emission features of hot silicon are detected with an excellent signal-to-noise ratio.

Hohlraum Magnetization Using Laser-Driven Currents

Principal Investigator: B. Pollock

Co-investigators: J. Moody, J. S. Ross, and D. Turnbull

In FY14 the HohlFaradayRot Campaigns on OMEGA EP and the B-FieldHohl Campaign on OMEGA launched an investigation of the feasibility of self-magnetizing hohlraum targets for ICF applications. The first campaign in this new experimental effort employed a target consisting of a half-loop formed by folding a thin gold sheet around a 500- μm -diam fused Si rod. Figure 140.94 illustrates how the OMEGA EP long-pulse beams shine through the holes in one of two parallel plates on the open side of the loop, producing a plasma at the surface of the second plate. Hot electrons formed by this process collect around the holes in the first plate, essentially charging up a parallel plate capacitor. The half-loop connects the plates, allowing the current to flow and produce a magnetic field on the loop axis. The OMEGA EP 4ω probe capability was employed to directly measure the magnetic field inside the loop via Faraday rotation along the hohlraum axis. Fields of up to 4.6 T were measured at the time of the probe beam. A new B-dot probe was also developed for this campaign and acquired a signal on all shots. Combining the B-dot probe data with a

second set of Faraday rotation measurements from a second piece of fused Si outside of the loop, the produced peak field is inferred to be ~ 40 T. In the second HohlFaradayRot shot day, the short-pulse backlighter beam was used to drive a proton source for proton-deflectometry measurements of the fringing magnetic fields around the target. This campaign allowed for additional parameter scans and extended the previous dataset.

The B-FieldHohl Campaign transitioned the experiment to OMEGA, taking advantage of the 60 beams available and increasing the target diameter from a 0.5-mm half-loop to a 2.0-mm, nearly complete loop. Similar to the OMEGA EP experiment, the magnetic field was driven by using 14 beams to illuminate parallel plates. Another eight beams were directed into the loop to heat the quasi-hohlraum, and the fringing magnetic field outside of the target was diagnosed with proton deflectometry from a D^3He capsule source. The analysis of this recent experiment is ongoing and will be used to guide the FY15 continuation of this effort.

High-Energy-Density Experiments

1. Material Equation of State Using Diffraction Techniques

Kinetics of Melting in Iron

Principal Investigator: R. Kraus

Co-investigators: F. Coppari, D. E. Fratanduono, A. Lazicki, D. Swift, J. H. Eggert, and G. W. Collins

The iron melting curve at multimegabar pressures is critical to understanding the earth's thermal state and also how its magnetosphere formed and evolves. Dynamic experiments can probe the melting transition at pressures near the inner-core boundary of the earth (~ 330 GPa). Nguyen and Holmes previously studied the melting transition with a gas gun,⁴⁸ using sound velocity measurements, but concerns about the results were raised because of the possible kinetics of melting.

This issue was addressed using *in-situ* x-ray diffraction at the Omega Laser Facility to directly probe the onset and completion of melting along the principal Hugoniot. Polycrystalline diffraction from the high-pressure hexagonal close-packed (hcp) phase of iron was monitored. As the iron was shocked to higher-pressure states along the melt curve, we observed an intensity decrease for the solid diffraction lines together with an increase in the diffuse scattering signal. Attributing this to liquid scattering (Fig. 140.95), we have shown that both incipient and complete melting occurred at the same stress states on the laser time scale (ns) as the gas gun's time scale (100's of ns), so the kinetics of melting are negligible for

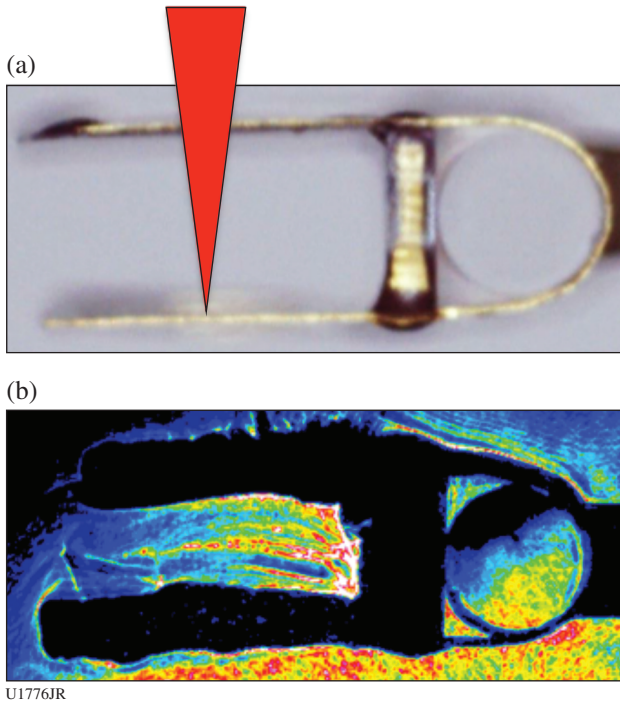
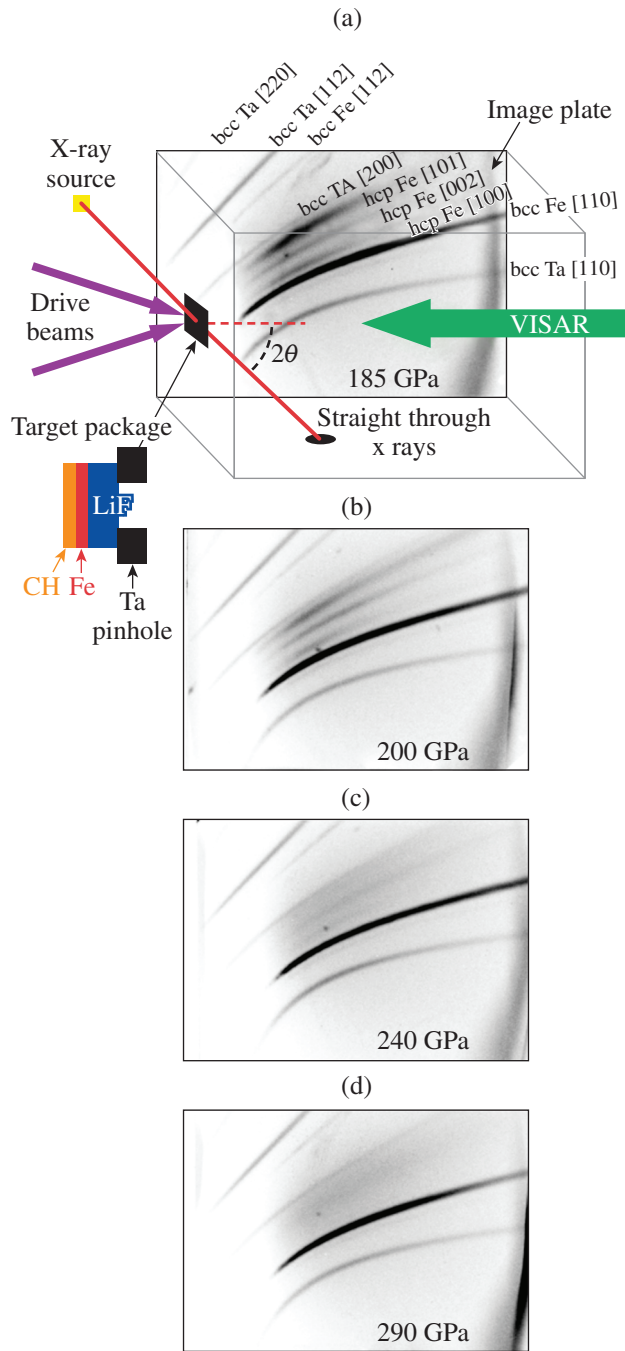


Figure 140.94
 (a) Geometry for hohlraum self-magnetization on OMEGA EP with the beam path shown schematically in red; (b) sample of 4ω probe data used to infer Faraday rotation.

these time scales and longer. The data also show that iron stays in the hcp phase along the melt curve until nearly 270 GPa, clarifying an issue that has been debated theoretically.



U1777JR

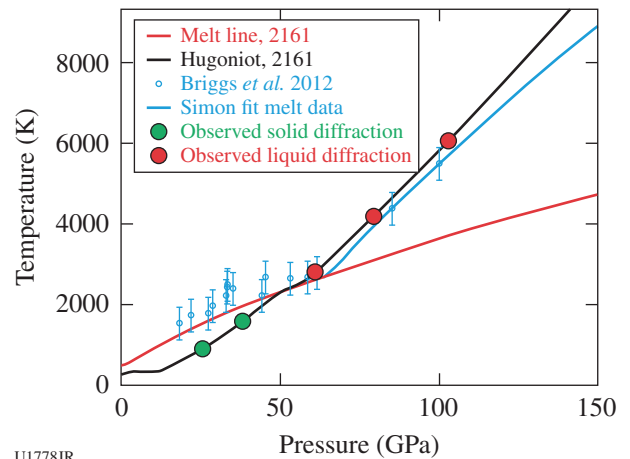
Figure 140.95
(a) Geometry for *in-situ* x-ray diffraction at the Omega Laser Facility. Also shown are image-plate data for shock-induced melting of iron, with a decrease of intensity in the solid diffraction signal and an increase in the diffuse background as melting occurs at higher shock pressures.

Kinetics of Melting in Tin

Principal Investigator: R. Kraus

Co-investigators: F. Coppari, D. E. Fratanduono, A. Lazicki, D. Swift, J. H. Eggert, and G. W. Collins

In this campaign, we used the PXRDIIP diagnostic to obtain *in-situ* x-ray diffraction at the Omega Laser Facility. Tin has a complicated high-pressure phase diagram, and the melting curve of tin has come under recent debate. Prior measurements of the melting temperature up to 1 Mbar show a dramatic increase in the slope of the melting curve as the solid phase transitions from a body-centered-orthorhombic (bco) to body-centered-cubic (bcc) structure.⁴⁹ Phase transitions in tin are also thought to be sluggish in comparison with other metals.⁵⁰ Our campaign's goal was to directly probe the onset and completion of melting along the principal Hugoniot of tin and compare the data with different time-scale experiments to learn about the kinetics of melting. For shock pressures below 50 GPa, the data show strong textured diffraction from the high-pressure phase of tin, whereas above 60 GPa, the data show a strong diffuse scattering signal from liquid tin (Fig. 140.96). These data bracket the melting transition along the principal Hugoniot, in agreement with significantly longer time-scale gas-gun experiments.



U1778JR

Figure 140.96
Pressure–temperature phase diagram for tin, showing the melting curve data from Ref. 49. Plotted along the Hugoniot of the 2161 *SESAME* equation of state are the pressure states where solid diffraction (green) and liquid diffraction (red) are observed.

Shock-Resolidification Kinetics of Tin and Iron

Principal Investigator: R. Kraus

Co-investigators: F. Coppari, D. E. Fratanduono, A. Lazicki, D. Swift, J. H. Eggert, and G. W. Collins

The Diffraction-EP Campaign extended earlier OMEGA experiments on melting kinetics of iron and tin by using OMEGA EP to probe the time scale for resolidification of both materials. Having previously shown that tin and iron can be shock melted on the time scale of a laser-shock experiment, and that melting occurred at the same pressures as in gas-gun experiments (to within the error bars of our measurements), these OMEGA EP experiments sought to quasi-isentropically compress tin and iron from shock-melted states back across the melt curve into the solid phase.

In the tin experiments, we generated an initial shock that was consistently at ~ 65 GPa (into the liquid phase) and then generated

a second shock that brought the tin to a peak pressure of ~ 160 GPa. The first shock set the initial thermodynamic state of the tin in the liquid phase, and the second shock quasi-isentropically compressed the tin into the solid stability field. After some tuning, we accurately timed the second shock and the backlighter. Figure 140.97 shows the observed strong polycrystalline diffraction peak from resolidified tin. These results are the first unambiguous observation of pressure-driven solidification in a metal. They show great promise that (1) we can probe the kinetics of solidification using laser-shock platforms and (2) *in-situ* x-ray diffraction provides an important tool in diagnosing the resolidification process.

In the iron experiments, we successfully observed strong diffraction from high-pressure hexagonal close-packed (hcp) iron, diffuse liquid scattering, and a very preliminary signature of resolidification. However, the initial thermal state in the liquid could not be accurately confirmed because of the issue with this initial experiment.

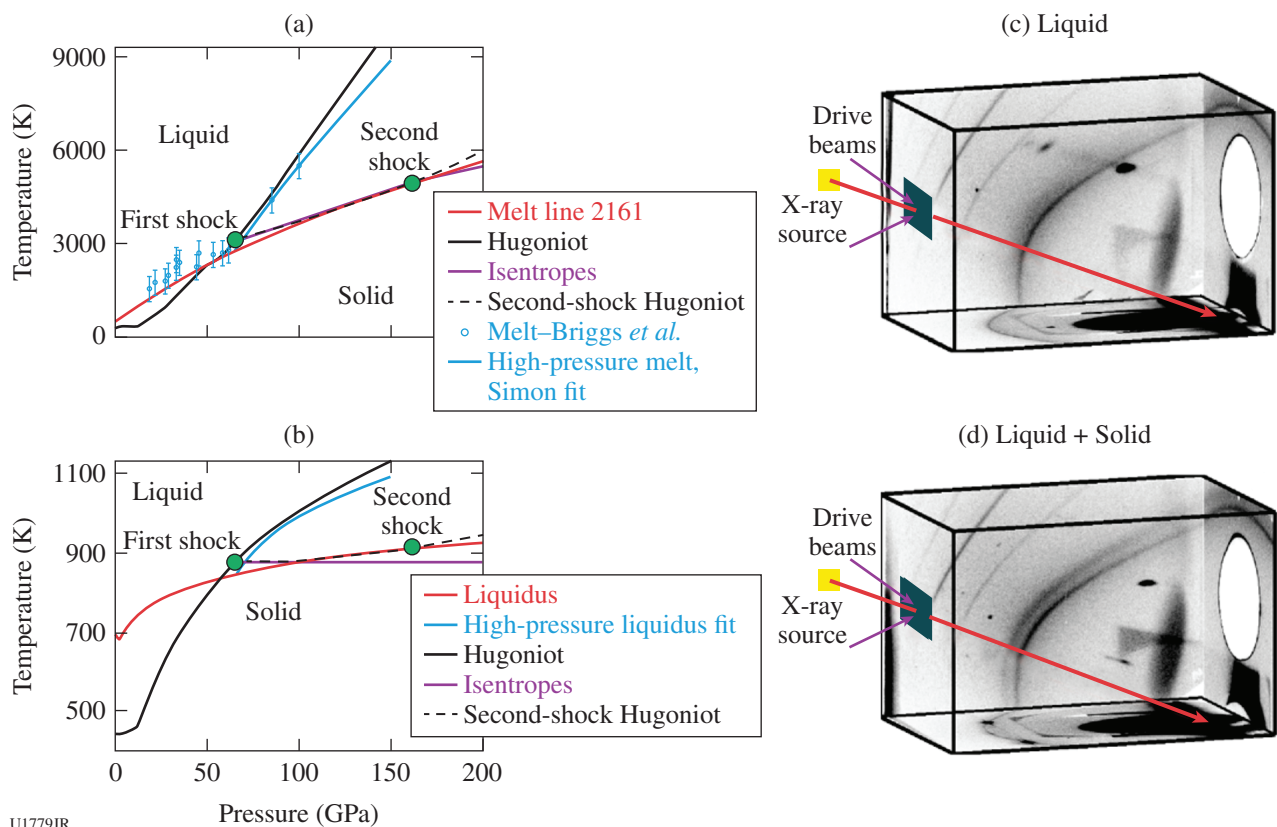


Figure 140.97

(a) Pressure–temperature phase diagram for tin from the *SESAME* 2161 equation of state. Static melting curve measurements (blue points) are from Ref. 49. (b) Pressure–temperature phase diagram for tin from *SESAME* 2161. [(c),(d)] Image plates from a double-shock experiment on Sn (first shock to 65 GPa, second shock to 160 GPa). The second shock in (c) is timed so that the x rays principally interact with unshocked and single-shocked material. The second shock in (d) is timed so that a larger volume of material reaches a second shock state of 160 GPa. Note the strong polycrystalline diffraction line observed in (d) does not exist in (c).

Improving the OMEGA High-Pressure Tantalum Diffraction Platform

Principal Investigator: F. Coppari

Co-investigators: J. H. Eggert, R. Smith, D. E. Fratanduono, A. Lazicki, and J. R. Rygg

This campaign improved the tantalum diffraction platform using the PXRDIIP diagnostic on OMEGA by resolving issues related to the high background signal observed in high-pressure shots; it also sought an understanding of the texture evolution when the sample material is ramp compressed to high-pressure states. We tested mitigation schemes that decreased the background signal and improved the platform overall. In particular, a tungsten wire, placed in a specific location of the diagnostic, provided a geometric trace of the background source. Although most of the background is caused by the ablation-generated plasma, some background also comes from the fluorescence of the image plates when hit by the direct x-ray beam. To mitigate this source of background, a fluorescence shield was implemented using a Ta skewed cylinder placed around the region where the direct x rays hit the image plate (Fig. 140.98). This mitigation scheme has also been adopted in the diffraction platform on the NIF with the target diffraction *in-situ* (TARDIS) diagnostic.

The second goal of the campaign was to start looking at the texture formation and evolution in ramp-compressed materials and, in particular, Ta. The shots compared diffraction from Ta samples with three different initial textures: commercial foils, coatings, and pressed powder. Preliminary characterization of the initial texture by laboratory x-ray diffraction and pole-figure analysis indicated that foils and coatings are characterized by a strong fiber texture, while the pressed-powder samples are randomly oriented, so that the corresponding diffraction signal is an untextured diffraction ring. The data show that when laser-driven ramp compression is used to achieve high-pressure states in these three materials, the initial texture

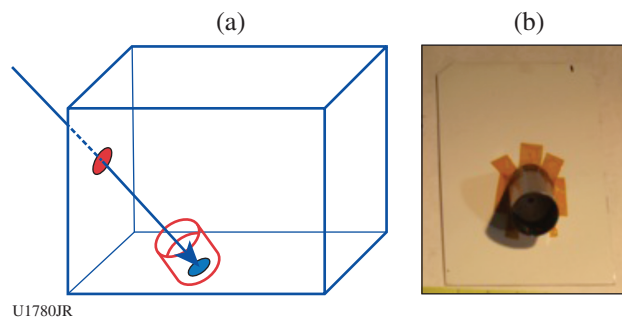
is preserved at high pressure and also across a phase transition. The initially untextured powder remained untextured, while samples with initial fiber texture showed a highly textured diffraction signal that persisted even above a solid–solid phase transition. This suggests that some sort of memory mechanism may take place that certainly deserves further investigation in future campaigns.

Development of Higher-Energy Backlighters for X-Ray Diffraction

Principal Investigator: R. Smith

The goal of these shots was to develop and optimize Zr He $_{\alpha}$ (16.3-keV) and Ge He $_{\alpha}$ (10.3-keV) x-ray sources for future x-ray diffraction experiments on OMEGA, OMEGA EP, and the NIF. The standard x-ray source for diffraction on OMEGA, using the PXRDIIP diagnostic, is the Cu He $_{\alpha}$ quasi-monochromatic line emission at 8.3 keV. In those experiments⁵¹ the main noise contributor at a high sample pressure is from thermal x rays generated in the sample drive plasma. To increase the signal-to-noise ratio of x-ray diffraction experiments, higher-energy sources that are spectrally decoupled from the drive plasma emission spectrum are necessary for more-effective noise filtering.

The targets for these experiments consisted of a freestanding, 2 × 2-mm, 10- μ m-thick Zr foil or a 6- μ m Ge layer coated on both sides of a 200- μ m pyrolytic graphite substrate. The spectrally resolved emission for a range of laser irradiance conditions was recorded with the XRS Rowland spectrometer and the NRL dual crystal spectrometer (DCS), which covers the x-ray bands from 10.4 to 45 keV and 20 to 120 keV. To optimize the output from Zr He $_{\alpha}$, up to 20 OMEGA beams were employed in a double-sided illumination geometry. Prepulse and main-pulse laser irradiance conditions on the Zr foil were systematically varied, and the resulting He $_{\alpha}$ production was measured. The laser power as a function of

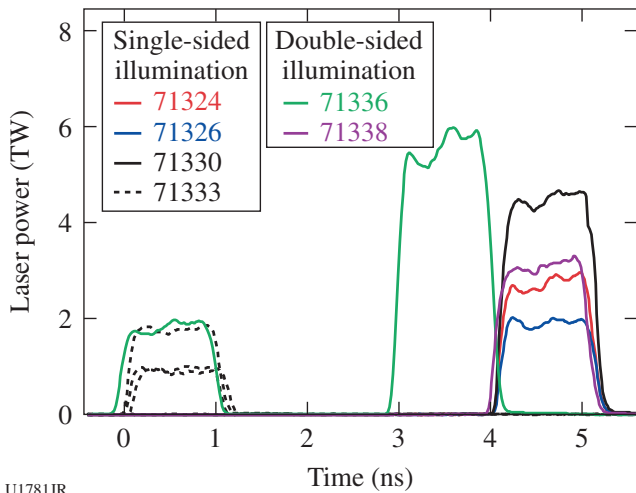


U1780JR

Figure 140.98

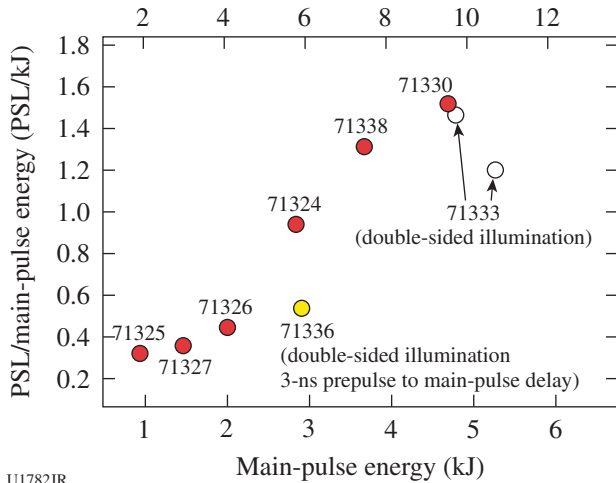
Fluorescence shield used on OMEGA to block x rays generated by the fluorescence of the bottom image plate hit by the direct x-ray beam. (a) Drawing of the position of the shield within the PXRDIIP diagnostic; (b) a photograph of the shield on the image plate.

time was varied shot-to-shot as illustrated in Fig. 140.99. The resultant PSL (photospectral luminescence) counts on the XRS spectrometer image plates from the He_α line per kJ of main-pulse laser energy are shown in Fig. 140.100 as a function of the main-pulse energy and intensity. The peak 16.3-keV He_α production occurs at an intensity of $\sim 8 \times 10^{15} \text{ W/cm}^2$. A similar experimental approach and analysis for Ge suggest that the He_α optimization occurs at a laser intensity of $1 \times 10^{15} \text{ W/cm}^2$.



U1781JR

Figure 140.99
Laser power versus time for the ZrHe_α backlighter development campaign.



U1782JR

Figure 140.100
PSL (photospectral luminescence) counts on the XRS spectrometer image plates from the 16.3-keV Zr He_α line per kJ of main-pulse laser energy are shown as a function of the main-pulse energy and intensity.

2. Material Equation of State Using Other Techniques

Measurements of the Lithium Hydride Equation of State

Principal Investigator: A. Jenei

Co-investigators: J. Hawreliak, R. London, D. E. Fratanduono, and G. W. Collins

The LiH equation-of-state (EOS) measurements started in FY13 were completed in FY14, providing data to constrain the shock Hugoniot EOS of LiH between 0 to 10 Mbar. Two different techniques were employed to determine the shock Hugoniot. The first method used velocimetry data from the VISAR (velocity interferometer system for any reflector) diagnostic to infer the velocities of reflecting shocks in a target with layers of single-crystal quartz and single-crystal LiH and pyrometry data from the streaked optical pyrometer (SOP) diagnostic to determine temperatures. Quartz was used as the EOS reference standard to determine the velocities and temperatures in LiH. Figure 140.101(a) shows an example of the raw data from this configuration, which succeeded in measuring the Hugoniot up to nearly 12 Mbar.

In the second approach, a framing camera radiographed the shock front and pusher/sample interface positions as a function of time in a shock-compressed sample backlit using a chlorine-doped plastic (2.8-keV) area backlighter. The motion of these fronts can provide absolute data on the shock and particle velocities. Although the pulse length was insufficient to generate a steady shock long enough to make an accurate EOS measurement, this experiment demonstrated successful imaging of the interfaces, as shown in Fig. 140.101(b). The information gathered about contrast and resolution provided valuable feedback for future experiment designs.

Equation-of-State Measurements on Single-Crystal Diamond

Principal Investigator: D. E. Fratanduono

NIF diffraction EOS experiments utilize single-crystal diamond in the target design to ramp compress the sample to high pressure and minimize the diffraction signal from the diamond. These experiments require an accurate stress-density response of single-crystal diamond. Previous OMEGA⁵² and NIF experiments⁵³ measured the stress-density response of CVD (polycrystalline) diamond, but there has been concern that the stress-density response of single-crystal diamond ($\langle 100 \rangle$ and $\langle 110 \rangle$) could be different from the CVD measurements. To address this, experiments were performed on OMEGA to measure the response of single-crystal diamond in the $\langle 100 \rangle$ and

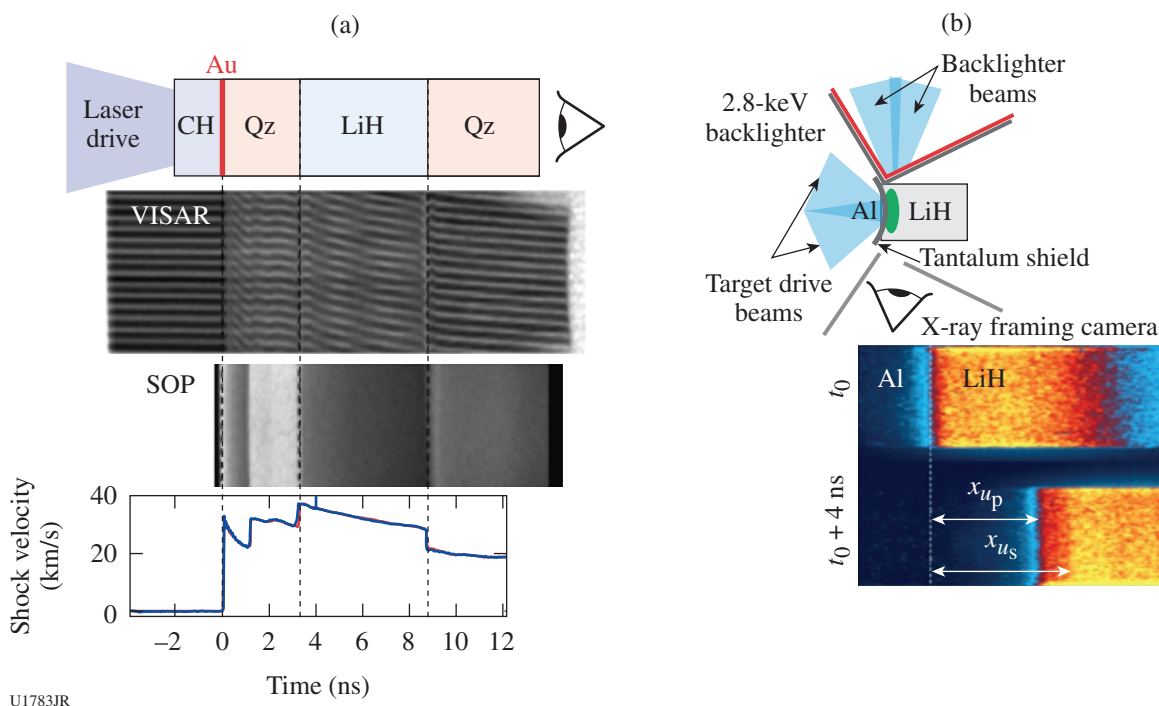


Figure 140.101

(a) LiH equation-of-state (EOS) measurements using a shock Hugoniot configuration and sample data using quartz as a reference standard. (b) Radiographic configuration and sample data for absolute EOS measurements.

$\langle 110 \rangle$ orientations, with a key result shown in Fig. 140.102. The stress–density response of single-crystal diamond is in excellent agreement with the stress–density response of CVD (polycrystalline) diamond, but results indicate that the “pullback” features observed in NIF experiments are significantly reduced in the $\langle 110 \rangle$ orientation when compared to $\langle 100 \rangle$. Radiation–hydrodynamics simulations have demonstrated a better predictive capability for the $\langle 110 \rangle$ orientation versus $\langle 100 \rangle$, but the EOS at high pressure must be improved. Future “A versus B comparison” experiments of the EOS of diamond $\langle 110 \rangle$ versus $\langle 100 \rangle$ will greatly assist in our development of a diamond strength model and will further probe the stress–density response up to 10 Mbar.

Extended X-Ray Absorption Fine-Structure Measurements of Ramp-Compressed Ta up to 200 GPa

Principal Investigator: Y. Ping

Co-investigators: F. Coppari, J. H. Eggert, and G. W. Collins (LLNL); and B. Yaakobi (LLE)

Based on successful improvements of the extended x-ray absorption fine-structure (EXAFS) platform in FY13,⁵⁴ high-quality EXAFS data of compressed Ta up to 200 GPa were

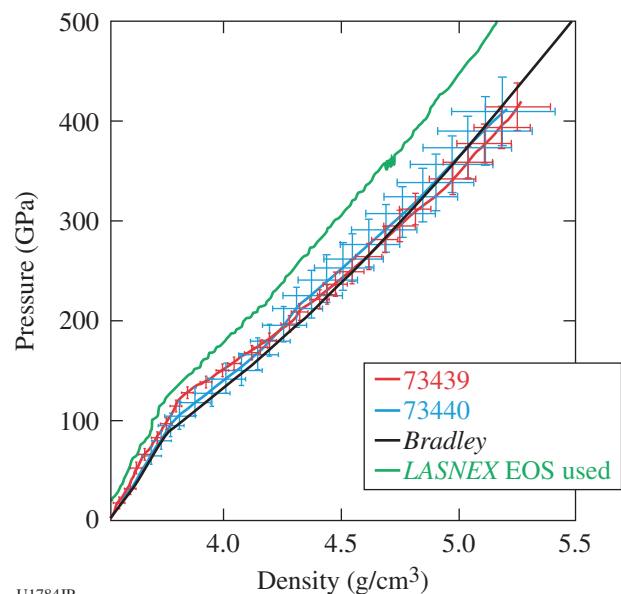
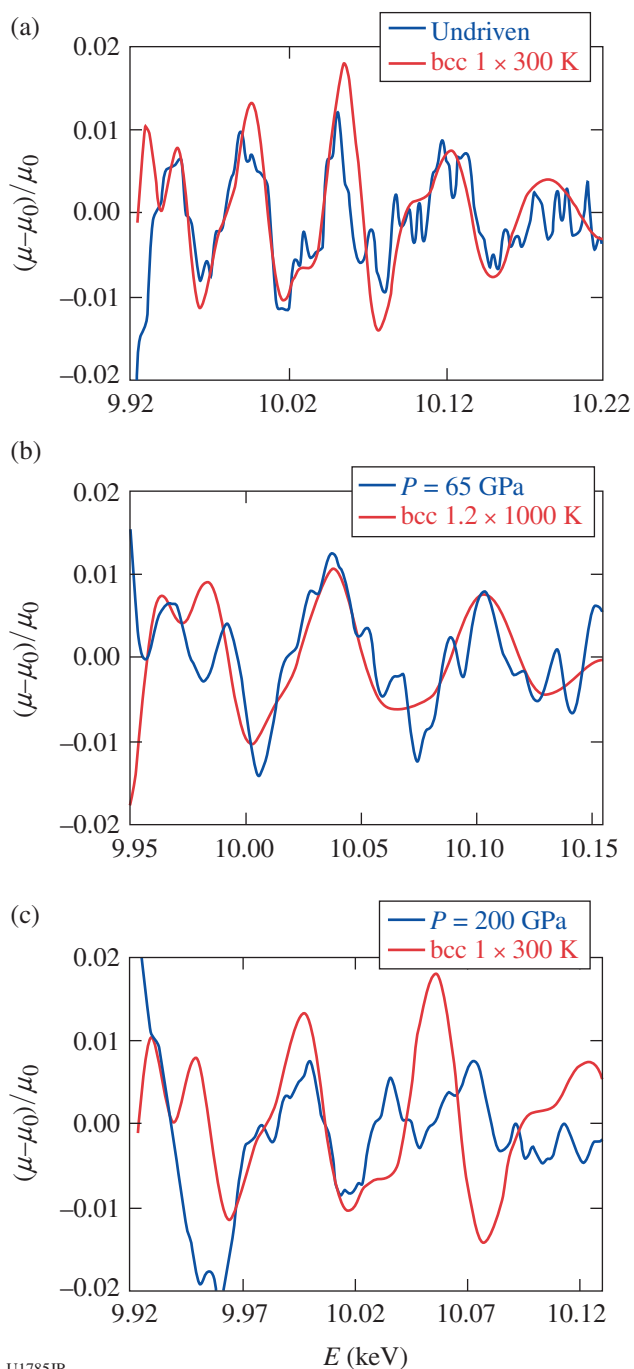


Figure 140.102

Newly measured pressure–density EOS data for single-crystalline diamond (red and blue curves), compared with prior data on polycrystalline diamond (black curve) and a reference EOS model (green curve).

obtained in FY14. The spectra at three pressures are shown in Fig. 140.103. The data at ambient conditions and at 65 GPa are consistent with Ta in the body-centered-cubic (bcc) phase, whereas the data at 200 GPa cannot be fit with the bcc phase, indicating



U1785JR

Figure 140.103
EXAFS data of Ta at (a) ambient conditions, (b) 65 GPa, and (c) 200 GPa. The measurements are shown in blue and the calculated EXAFS spectra for the bcc phase are shown for comparison in red. The 200-GPa data demonstrate that Ta is no longer in the bcc phase at such high pressures.

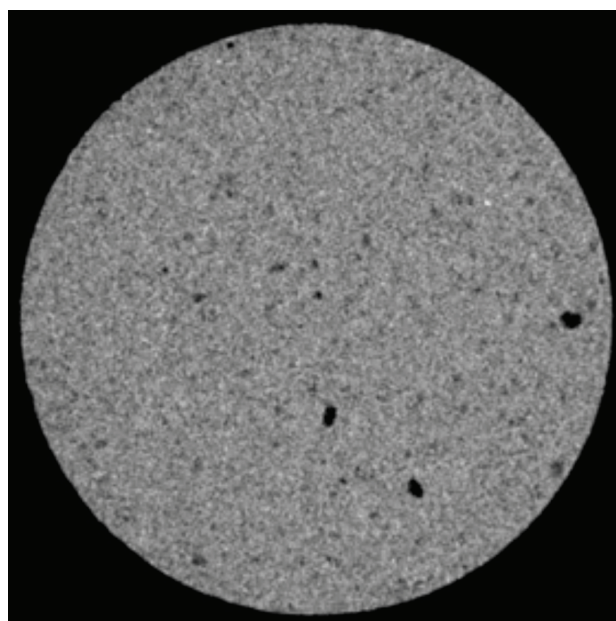
that Ta undergoes a phase transition above 1 Mbar. Subsequent shots reached 350 GPa; however, the quality of this EXAFS data was not as good as previous data. Two reasons have been identified: First, the target alignment fiducial was not as accurate as before, reducing the number of observable channels from 5 to 2, significantly degrading the signal-to-noise ratio. Second, the back-lighter brightness was $\sim 40\%$ less than on prior shots for reasons under investigation but not yet understood. Both findings provide important guidance for upcoming FY15 shots.

3. Hydrodynamics

Mix-Width Measurements of Accelerated Copper Foam on OMEGA

Principal Investigator: K. Baker

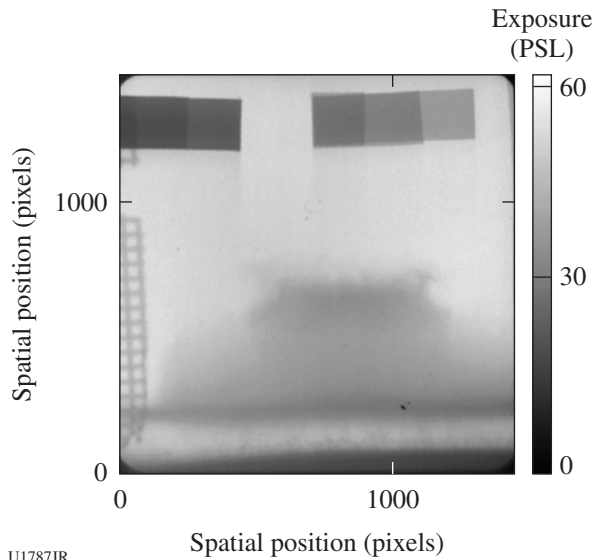
This campaign evaluated two experimental configurations to determine the mix width of accelerated copper foams and measured the effect of the internal structure of the copper foams on the measured mix width to compare the experimental results with simulations. All the targets were cylindrical shock tubes with a reduced-density copper (Cu) foam, 1 g/cm^3 , pusher-accelerated into a low-density carbonized resorcinol formaldehyde (CRF) foam at 50 mg/cm^3 . The Cu foams, which could contain voids as large as 5 to $10 \mu\text{m}$, were characterized via x-ray-computed tomography at either the Advance Photon Source or with an X-Radia MicroXCT. An example is displayed in Fig. 140.104.



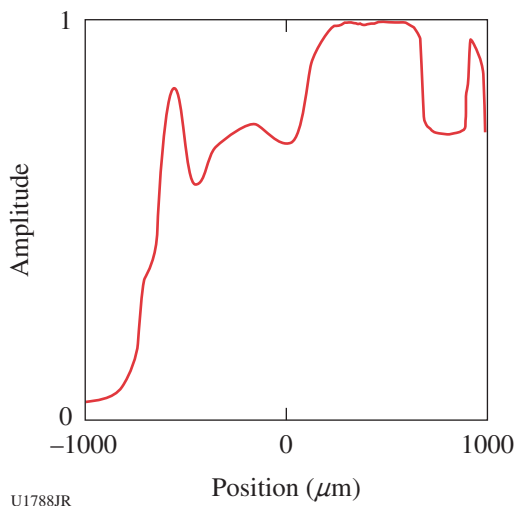
U1786JR

Figure 140.104
Reconstructed density profile of a copper foam. The voxel size of the reconstructed density is a cube, $\sim 7 \mu\text{m}$ per side.

In the first configuration, the copper foam was reduced to an 800- μm -diam cylinder for the 120 μm closest to the Cu/CRF interface (to reduce edge effects in the images) and radiographed using the OMEGA EP backlighter. The removed Cu foam was replaced with CH. The second experimental configuration used a nickel He α backlighter at 7.66 keV and a modified target design to accommodate the lower energy and minimize edge effects. Figure 140.105 shows a radiograph of the accelerated copper foam obtained using the OMEGA EP backlighter in the first configuration; Fig. 140.106 shows a lineout through



U1787JR
Figure 140.105
Radiograph of an accelerated copper foam 25 ns after the start of the hohlraum drive.



U1788JR
Figure 140.106
Vertical lineout through the accelerated copper foam shown in Fig. 140.105. The mix width comes from the 10% to 90% region between 0 and 250 μm of the graph.

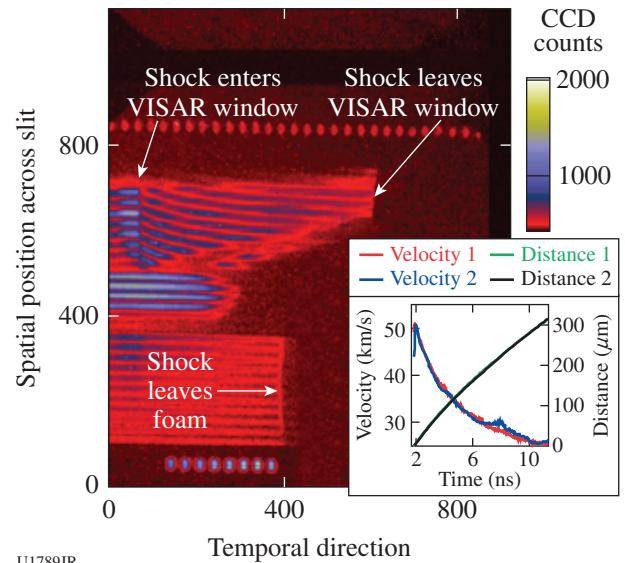
the radiograph. The mix width for this foam was determined to be 135 μm .

Shock Transit Time Measurements on Novel CH Foams

Principal Investigator: K. Baker

Shock breakout times from x-ray-driven samples of newly formulated CH_{1.6} foams were measured on this campaign for comparison with traditional carbonized resorcinol formaldehyde (CRF) foams. The foams were positioned as packages on the end of a gold halfraum. To account for differences in the drive between experiments, the hohlraum drive history was measured via breakout from an aluminum witness plate, as well as via shock speeds in α quartz using the velocity interferometer system for any reflector (VISAR). As illustrated in Fig. 140.107, all shots returned good VISAR data, showing the breakout times of the foam into and out of the VISAR window and the breakout of the shock from the CH_{1.6} or CRF foams. The corresponding VISAR unfold of the drive is inset in the lower right-hand corner of the figure. Comparison of experimental breakout times with simulations showed very good agreement with the CRF foams and good agreement with the CH_{1.6} foams.

Additionally, three Ross pair channels were implemented in Dante to look at the gold M-band emission from the laser-driven hohlraum: Saran, silver, and Mo. Four Ross pair channels were also implemented in a time-integrated x-ray pinhole camera to look at the M-band wall emission: Si, Zr, Mo, Saran, and



U1789JR
Figure 140.107
Drive and sample shock-speed measurements for CH_{1.6} foams. CCD: charge-coupled device.

Kapton. These also look promising for determining the time-integrated M-band spatial and spectral distribution on the wall.

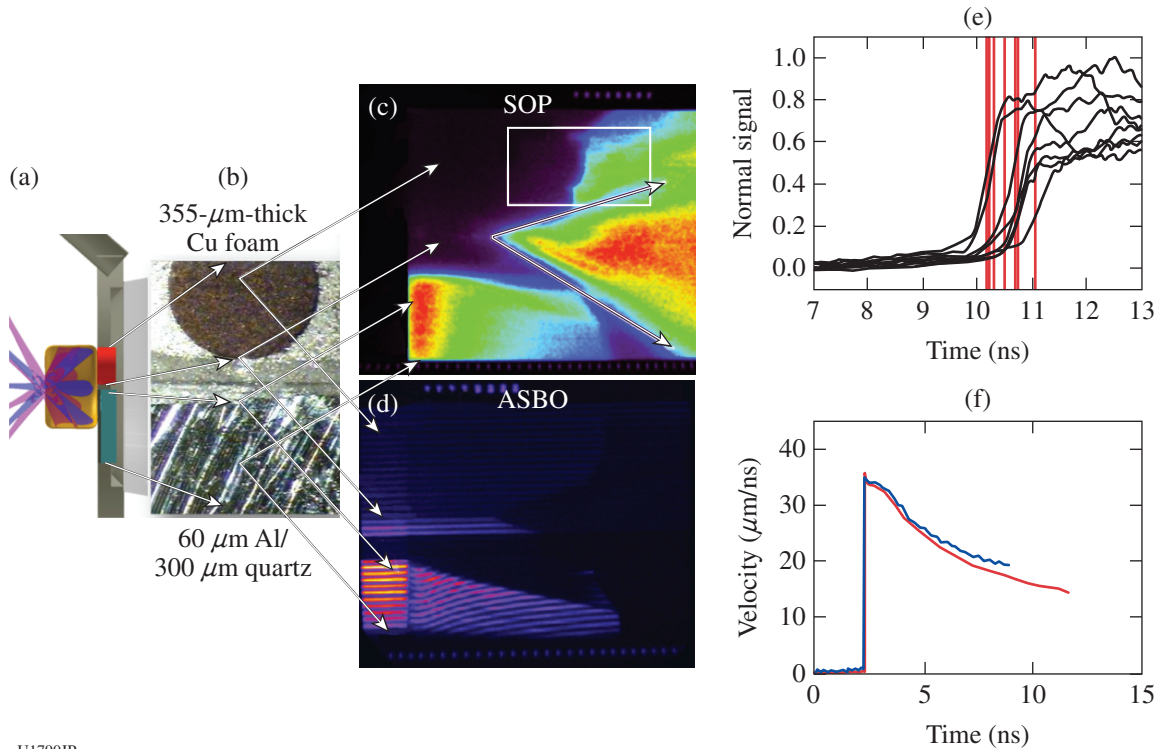
Copper Foam Shock Breakout Measurements on OMEGA
Principal Investigator: A. Moore

High-Z metal foams made via a copper ceramic casting process and with $\sim 1/10$ th solid density ($\sim 1 \text{ g/cm}^3$) have been developed at LLNL and are being produced routinely at the Atomic Weapons Establishment (AWE). This campaign investigated the relative shock propagation in foams having $1.0\text{-}\mu\text{m}$ characteristic pore sizes to qualify the equation of state (EOS) for use in future experiments. Propagation of a single shock through a material sample is an established technique to quantitatively validate the EOS model for that material via the simple dependence of the shock velocity on the pressure and, therefore, the internal energy of the material, but it had not been applied previously to these novel foams. The platform to measure the shock transit time in Cu foams was unchanged from prior campaigns of this type, using a 1.6-mm-diam, 1.0-mm-long hohlraum driven by 5.5 kJ of 351-nm laser energy

using 15 beams of the OMEGA Laser System. To improve the measured accuracy of the x-ray drive from the hohlraum, however, an Al witness sample was added so that the target package on the halfraums included a foam sample with a polystyrene ablator along a $60\text{-}\mu\text{m}$ aluminum sample backed by $300 \mu\text{m}$ of quartz. When the shock breaks out into the quartz, it can be measured directly using the active shock breakout (ASBO) or VISAR diagnostic, and the pressure history at the hohlraum ablator interface can be inferred.⁵⁵

In the experiments the drive pulse shape was varied to extend the density and temperature regimes probed. A 1.0-ns square pulse shape was used on experiments with the C_8H_8 ablator and a 2.7-ns ramp-shaped laser pulse on experiments without this ablator. The copper foam samples were 0.7 mm in diameter and nominally 0.35 mm in thickness, with a nominal density of 1.0 g/cm^3 . On these experiments the hohlraums reached a peak effective radiation temperature of $208 \pm 5 \text{ eV}$.

Data from the streaked optical pyrometer (SOP) were obtained on five shots, an example of which is shown in Fig. 140.108(c).



U1790JR

Figure 140.108

Streaked optical pyrometer (SOP) and active shock breakout (ASBO) data from shot 71664 for a hohlraum with no CH ablator driven by a SS2704vA01 shaped pulse. (a) VisRad diagram of the target. (b) Images of the Cu foam ($355 \mu\text{m}$ thick at a density of 1.084 g/cm^3) and Al/quartz surface viewed by the ASBO and SOP. (c) Raw SOP image data with arrows highlighting edge effects caused by the expanding joint between the Cu foam and Al/quartz samples. (d) Raw ASBO image data showing shock breakout times. (e) Normalized optical emission caused by the shock breakout showing that the shock in the Cu foam arrived at $10.48 \pm 0.33 \text{ ns}$. (f) Shock velocity in the quartz peaked at 34 km/s , within 3 km/s of pre-shot predictions.

These data indicate that some spatial structure exists in the shock traveling through the Cu foam, but the average shock breakout time was still determined to within $\pm 3\%$. The ASBO was used on three shots to measure the decaying shock velocity as a function of time in the quartz, returning data very close to pre-shot predictions.

High-Energy Point-Projection Backlighter Experiments on OMEGA

Principal Investigator: K. Baker

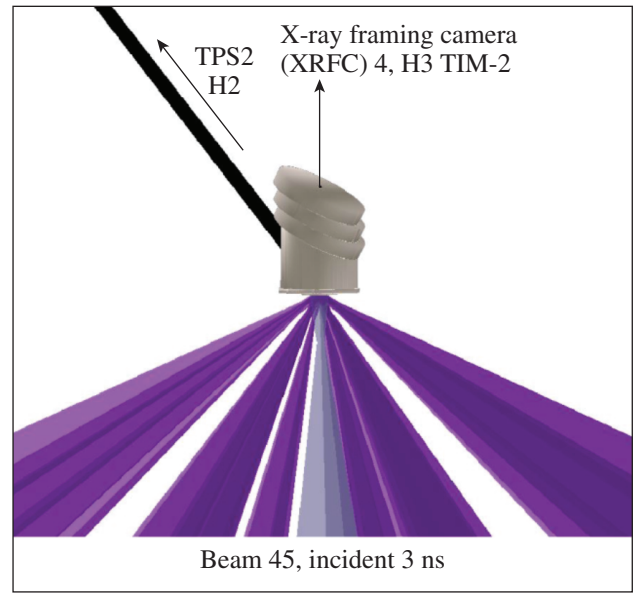
The goal of this campaign was to evaluate high-energy backlighters for use on the NIF. The backlighter energies needed on the NIF range from 35 to 45 keV. Previous conversion efficiency (CE) measurements with short-pulse lasers at 1ω indicated a CE of 7×10^{-5} for tin through 4×10^{-5} for samarium. These efficiencies are close to meeting NIF-required fluences using the Advanced Radiographic Capability short-pulse laser being deployed on the NIF but would require that the NIF detector be placed much closer to the target than previously. However, the previous experiments had been conducted with wire backlighters, and other laser-target geometries are possible to improve x-ray fluence yields. In this campaign, the OMEGA 3ω lasers were used to drive a point-projection backlighter with a Ta pinhole to reduce the source size. Tin and samarium targets were fielded, with and without a prepulse, using either thick solid or exploding-foil plasmas. Figure 140.109 illustrates the target geometry. The transmission crystal spectrometer (TCS) measured the tin and samarium spectra. Figure 140.110 shows the TCS spectra from these shots, together with a prior 1ω short-pulse silver wire backlighter spectrum.

The highest conversion efficiency was seen for thick foils without a prepulse. The prepulsed plasmas may have refracted the drive laser beams, leading to a reduction of yield. Resolution tests using a sharp, opaque gold edge had blurry features for all the targets, indicating a large source size. This could be improved with a significantly thicker or more-advanced pinhole substrate.

Radiographic Techniques for Drive Symmetry

Principal Investigator: D. Martinez

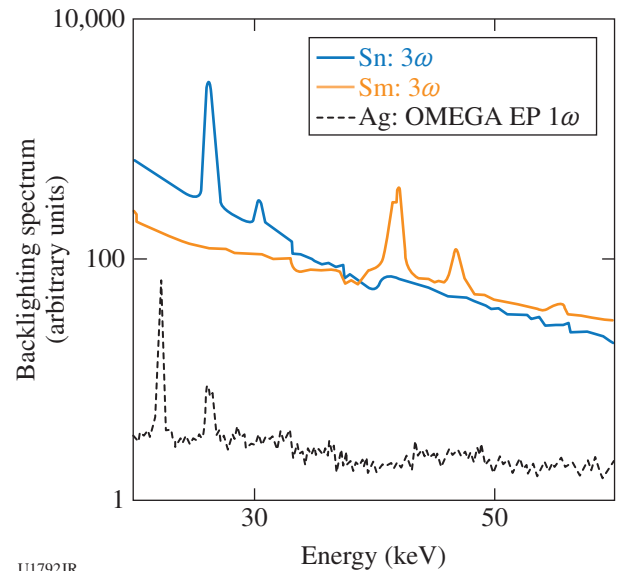
Hohlraum experiments were performed on the OMEGA Laser System to develop and exploit radiographic techniques to study the symmetry of foam balls illuminated with hohlraum x rays. Using a joint OMEGA EP configuration, $10\text{-}\mu\text{m}$ -thick Ag wire backlighters mounted on $300 \times 300\text{-}\mu\text{m}$ -sq, $10\text{-}\mu\text{m}$ -thick polyimide foils were irradiated with the $\sim 1\text{-kJ}$ short-pulse OMEGA EP beam in a configuration similar to that expected on the NIF Advanced Radiographic Capability short-pulse



U1791JR

Figure 140.109

Target geometry used to evaluate the efficacy of high-energy point-projection backlighters. The pinhole substrate was $200\text{-}\mu\text{m}$ -thick Ta, sandwiched between $100\text{-}\mu\text{m}$ disks of CH to limit the number of hot electrons reaching the pinhole substrate.



U1792JR

Figure 140.110

Backlighter spectra measured with the transmission crystal spectrometer (TCS).

laser, with a pulse duration of ~ 50 ps at a laser intensity of $\sim 2 \times 10^{17}$ W/cm². Point-projection x-ray radiographs of the targets with a magnification of ~ 40 were measured on image plates using the HERIE diagnostic positioned ~ 50 cm from target chamber center. The high-energy bremsstrahlung spec-

trum was used to diagnose the target. Figure 140.111 shows data from resolution test objects illustrating the radiographic signal and contrast, which were consistent with previous Ag μ -wire experiments using OMEGA EP and demonstrated 17- μ m resolution. Transmission of the backlighter through a Cu step wedge was measured and used to infer the hot-electron temperature by modeling the backlighter with a simple single-temperature bremsstrahlung spectrum. These experiments produced high-quality radiographs and established a baseline for future complex hydrodynamics experiments on the NIF.

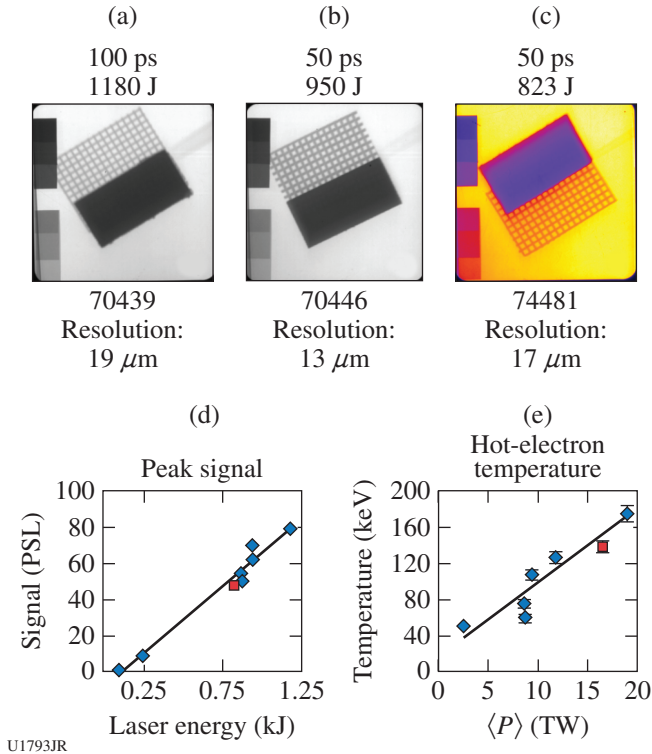


Figure 140.111 [(a),(b)] Silver μ -wire backlighter from past Toto experiments compared with (c) current performance. [(d),(e)] Trends in the peak signal and approximated hot-electron temperature show that results are consistent with previous Ag μ -wire experiments using the same filtering and diagnostic.

Proton Heating of Copper Foams on OMEGA EP

Principal Investigator: A. Moore

High-Z metal foams made by a copper ceramic casting process at $\sim 10\%$ of solid density ($\sim 1 \text{ g/cm}^3$) provide a novel target material for use in high-energy-density-physics experiments on the NIF, Orion, and OMEGA. For experimental results to be constraining to radiation-hydrodynamics simulation codes, however, the materials must be well characterized, with a good understanding

of the material opacity and EOS. These proton-heating experiments developed a platform to access the EOS of the Cu foam via isochoric heating of the material with protons and investigated the feasibility of scaling the approach to the NIF using the upcoming Advanced Radiographic Capability short-pulse laser.

Proton heating offers a novel way to measure the low-temperature EOS since the energy is absorbed near-isochorically by the Cu foam, especially when compared to heating with x rays or via direct laser irradiation.⁵⁶ If the density profile of the expanding plasma is measured, the isentrope can be extracted directly. These experiments studied density measurements of proton-heated disks of Al and Cu foam and Cu wires. The proton source consisted of a 10- μ m-thick, 500- μ m-diam Au foil irradiated by a high-intensity ($\sim 1 \times 10^{18} \text{ W/cm}^2$), 1053-nm, 10-ps laser pulse from the OMEGA EP laser. This generated a proton beam through target-normal sheath acceleration (TNSA).⁵⁷ The Cu foam and other samples were placed 2 mm from the proton source along the normal to the Au disk. To radiograph the sample expansion, a Ni foil backlighter was positioned 5 mm from the sample perpendicular to the foam disk normal. Beamlines 1, 3, and 4 delivered 1-ns, 351-nm laser pulses to this Ni foil with a 10-ns delay after the short-pulse beam, generating He α x rays (7.9 keV) to radiograph the expanding Cu foam.

The proton spectrum was measured using a radiochromic film (RCF) stack 25 mm past the Au disk source. Figure 140.112 shows the proton "auto-radiograph" measured using the RCF stack when the Cu-foam disk was present and heated by the

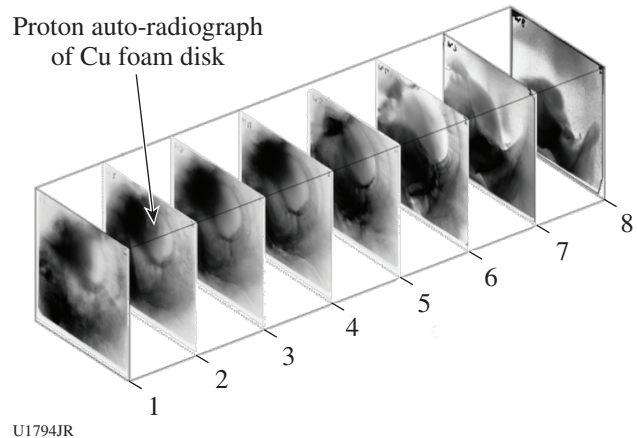


Figure 140.112 "Proton auto-radiograph" of the proton-heated Cu foam measured by a radiochromic film pack in the near-target arm diagnostic.

protons. Figure 140.113 shows the success of the area-backlit radiography in obtaining images of the unheated and heated Cu foams. Work is ongoing to establish the relative contribution of x-ray and proton heating at the front surface of the Cu foam.

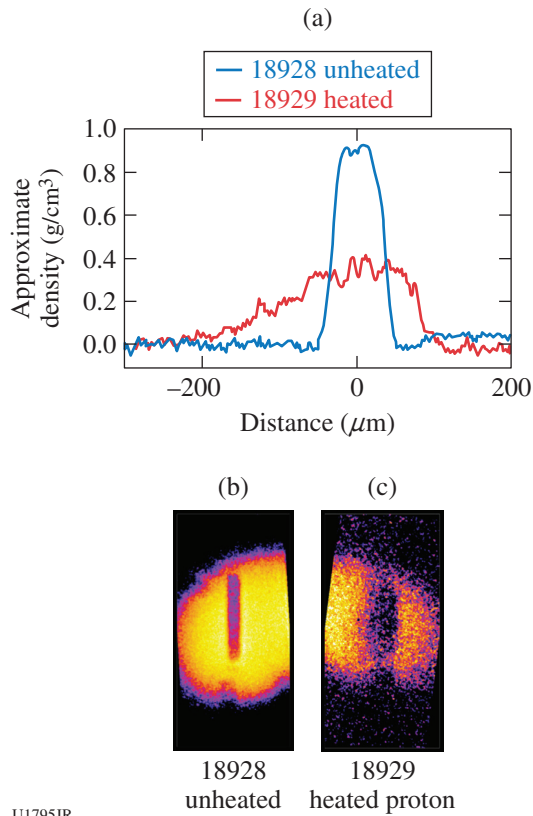


Figure 140.113 Radiograph of unheated (shot 18928) and proton-heated (shot 18929) Cu foam after 10 ns of free expansion. The density profile of the heated foam is obtained assuming no significant changes to the opacity of the Cu foam when heated and calibrating the backlighter x-ray spectrum using the predicted transmission of the 0.9-g/cm³ unheated foam.

4. Radiation Transport and Opacity

X-Ray Spectroscopy of Fully Characterized Non-LTE Gold Plasmas

Principal Investigator: G. Brown
 Co-investigators: J. A. Emig, M. E. Foord, R. F. Heeter, D. Liedahl, C. A. Mauche, J. S. Ross, M. B. Schneider, and K. Widmann (LLNL); and D. H. Froula and J. Katz (LLE)

Experiments on the NIF have shown a need for a more-precise understanding of the radiative properties of non-LTE gold to improve x-ray drive simulations of laser-driven hohlraums used

in inertial confinement fusion and other areas of high-energy-density physics. Expanding on prior work,⁵⁸ the AuNLTE-14A Campaign fielded laser-heated beryllium-tamped gold/iron/vanadium foils, with the following primary objectives: (1) high-resolution measurements of time-resolved gold M-band spectra from 2 to 5.5 keV, simultaneously with (2) measurements of the plasma electron temperature (T_e) via K-shell emission from helium-like V and Fe ions, (3) independent measurements of T_e using Thomson scattering in a transmission geometry, and (4) measurements of the sample density by time-resolved spectral imaging of its expansion normalized to the initial thickness.

This campaign acquired data for three different target types: (a) “thicker” and (b) “thinner” mixtures of Au, Fe, and V, and (c) a mixture of Fe and V without Au. Simultaneous K-shell spectra from He-like Fe²⁴⁺ and V²¹⁺ and M-band Au, together with expansion images, were acquired for all three target types (Fig. 140.114). After some adjustments, ion-acoustic-wave (IAW) “transmission” Thomson-scattering data were successfully obtained, for the first time, from plasmas at electron densities >10²¹/cm³. Some of the IAW data were obtained simultaneously with the other measurements, with measured T_e in the ~1-keV range. Although detailed data analysis is ongoing, this suite of measurements is potentially the most-comprehensive non-LTE data set recorded to date. If confirmed in the final analysis, this will yield improved validation benchmarks for non-LTE models.

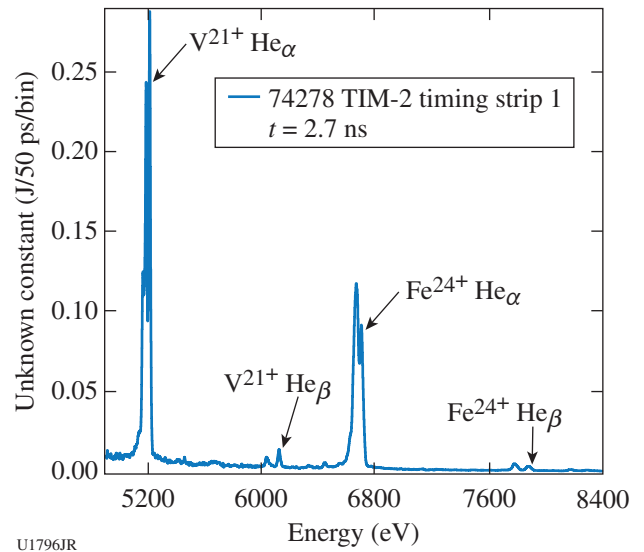


Figure 140.114 Spectrum measured by the MSpec spectrometer of the x-ray emission from K-shell transitions in highly charged vanadium and iron.

5. Material Dynamics and Strength

Classical Rayleigh–Taylor Growth

Principal Investigator: C. Huntington

Within the material strength effort aimed at assessing the strength of various metals at high pressure and a high strain rate, the goal of the Classical Rayleigh–Taylor Campaign is to measure Rayleigh–Taylor (RT) growth of samples that behave “classically,” i.e., can be fully modeled using a fluid description. Without the stabilization of strength, classical RT growth is characterized by a growth rate $\gamma = \sqrt{kgA_n}$, where k is the wavelength of the unstable mode, g is the acceleration, and the Atwood number A_n quantifies the magnitude of the density jump at the interface. The sample in the experiment is accelerated by the stagnation of a releasing shocked plastic “reservoir,” which is directly driven by ~ 1 kJ of laser energy. The growth of preimposed ripples is recorded using transmission x-ray radiography of a vanadium He_α source, where the opacity of the sample is calibrated to the ripple amplitude. The FY14 campaigns collected data for ripples with $30\text{-}\mu\text{m}$, $60\text{-}\mu\text{m}$, and $120\text{-}\mu\text{m}$ wavelengths. An example of $60\text{-}\mu\text{m}$ data is shown in Fig. 140.115. The area backlighter generates an image with varying brightness across the image; the brightest region is analyzed, and a background curve that captures the shape of the x-ray illumination is subtracted. The pre-shot metrology and measured ρR of the driven sample together yield the growth factor, which is compared to models of RT growth.

6. X-Ray Source Development and Application

Calibration of the NIF X-Ray Spectrometer

Principal Investigator: S. P. Regan (LLE)

Co-investigators: F. Pérez, M. A. Barrios Garcia, K. B. Fournier, G. E. Kemp, J. Pino, J. Emig, and S. Ayers (LLNL); M. Bedzyk, M. J. Shoup III, A. Agliata, B. Yaakobi, and F. J. Marshall (LLE); and J. Jaquez, M. Farrell, and A. Nikroo (GA)

The NIF x-ray spectrometer (NXS) is an elliptically bent crystal spectrometer that provides both time-resolved and time-integrated spectral measurements. The NXS covers a spectral range from 2 to 18 keV in ten discrete spectral windows, each corresponding to a particular crystal configuration. Two FY14 OMEGA campaigns provided data for a photometric calibration for all 30 NXS crystals (each configuration has three interchangeable crystals), by uniformly irradiating millimeter-scale spherical targets coated with various cocktails of mid-Z elements. The targets were designed to generate either L-shell or K-shell emission within the energy range of the NXS' spec-

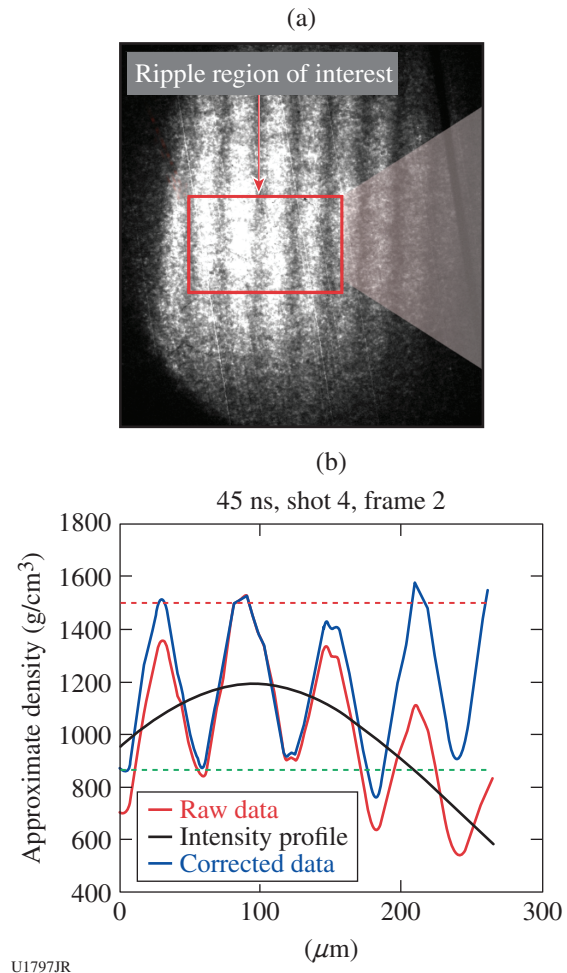


Figure 140.115

(a) A region of interest (shown in red) is selected from a piece of data. (b) The integrated profile of these ripples is shown in red, and the “corrected” trace is shown in blue, after being adjusted by the black curve.

tral windows. Five different targets were designed for these calibration shots: four coated with CrNiZn, ZnZr, SiAgMo, or: TiCrAg coatings, and one uncoated CH target used to measure continuum emission. Target emission was recorded by five different spectrometers for each shot: three NXS and two XRS spectrometers. The XRS spectrometer crystals were absolutely calibrated off-line and provide an absolute x-ray yield from which the photometric calibration of the NXS crystals will be derived. All data were recorded onto Fuji spatial resolution (SR)-type image plates, which are also being calibrated off-line to provide an end-to-end absolute calibration for the NXS spectrometer.

In preparation for the OMEGA calibration shots, hydrodynamic simulations using *HYDRA* and *ARES* were performed

to predict the emission from the metal-coated targets. Figure 140.116 compares these simulation results with the absolute x-ray yields measured by the XRS spectrometer for all four metal-coated targets. Here, target types A, B, C, and D correspond to SiMoAg, TiCrAg, CrNiZn, and ZnZr coatings, respectively. The predicted line emission agrees qualitatively with the

XRS results. Details on the simulations and comparison with the XRS data have been published.⁵⁹ A more-rigorous comparison between model and measured data will be performed once the absolute NXS calibration is finalized. Figure 140.117 shows sample data measured for one of the NXS spectrometers. This shot used a CrNiZn-coated target; measured data on the

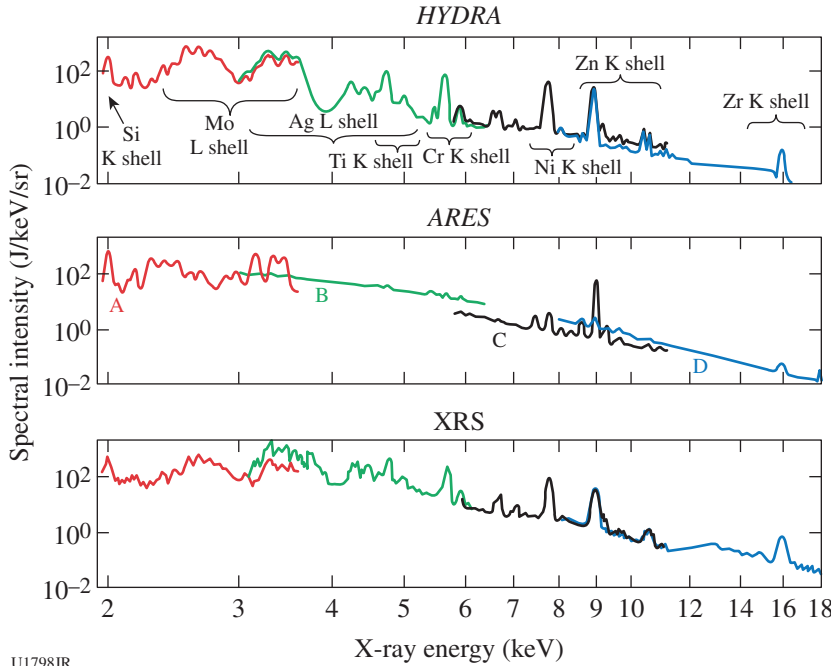
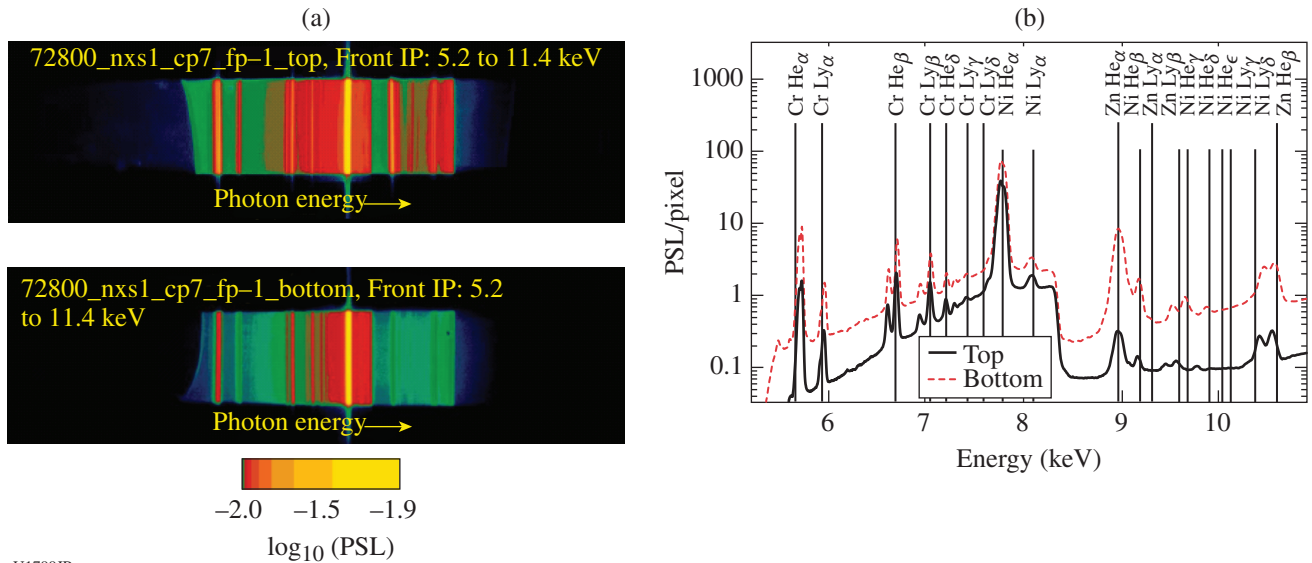


Figure 140.116 Simulated spectra using *HYDRA* and *ARES* hydrodynamics codes are compared to measured XRS data for metal-coated targets A (SiMoAg), B (TiCrAg), C (CrNiZn), and D (ZnZr). Good qualitative agreement between data and simulations is observed.

U1798JR



U1799JR

Figure 140.117 Measured data on the NIF x-ray spectrometer (NXS) for one of ten configurations. (a) Measured spectra recoded onto an spatial resolution (SR) image plate, with (b) corresponding data lineouts.

top and bottom image plate are shown in Fig. 140.117(a), with corresponding lineouts in Fig. 140.117(b). Several K-shell emission lines from Cr, Ni, and Zn were observed and identified.

X-ray Source Fluence Measured as a Function of Viewing Angle

Principal Investigator: M. Barrios Garcia

Co-investigators: M. J. May, K. B. Fournier, F. Pérez, and J. D. Colving (LLNL); F. Girard and B. Villette (CEA); S. Seiler and J. Davis (DTRA); and J. Fisher and C. D. Newlander (Fifth Gait Technologies)

The NSView Campaign was designed to understand target fluence as a function of viewing angle for x-ray source applications, to better understand the fluence delivered to material samples and other test objects using these or similar targets as x-ray sources. In this campaign, stainless-steel-lined cavities were symmetrically driven with ~ 20 kJ of 3ω light delivered in 1 ns. To provide distinct view angles for the diagnostics fielded, three different laser-target orientations were used throughout the day. The target x-ray emission was recorded with a suite of x-ray diagnostics, enabling one to characterize both the temporal evolution and spectral content of the source.

Figure 140.118 shows the measured spectra recorded using the Dante and DMX spectrometers, for view angles relative to the target symmetry axis of 0° , 42° , and 79° , and 5° , 46° , and 75° , respectively. These instruments observe a pronounced view angle dependence on the measured flux for x-ray energies below 4 keV, but little to no dependence on a view angle is observed for the Fe K-shell emission at higher energies. The observed x-ray emission from 4 to 9 keV, describing the Fe K shell, is consistent with a volumetric emitter that is therefore optically thin and independent of view angle. The emission from 2 to 4 keV is also consistent with a volumetric emitter, once geometric and optical-depth corrections are considered. These factors cause the x-ray yield to decrease as a function of increasing view angle. For x-ray emission between 0 to 2 keV, corresponding to the Fe L shell, the observed yields peak at angles $\sim 42^\circ$ to 46° and show the largest variation between view angles. This low-energy x-ray yield is also the dominant contribution to the total x-ray production. A spectral reconstruction model developed to match these observations suggests the x-ray output between 0 to 2 keV is best described as a surface emitter, where the emission originates from the cavity's inner walls and laser entrance hole. Figure 140.119 compares this

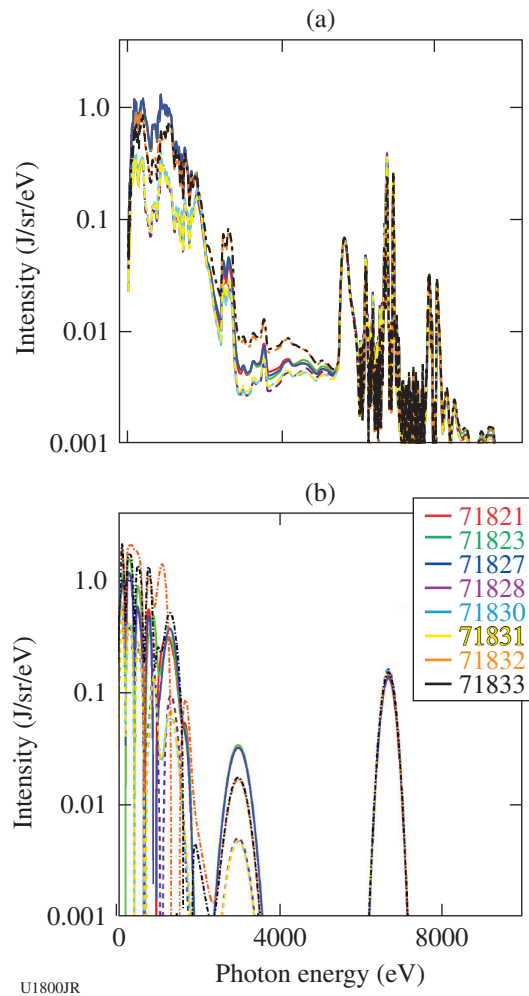


Figure 140.118
Measured (a) DMX and (b) Dante time-integrated spectra.

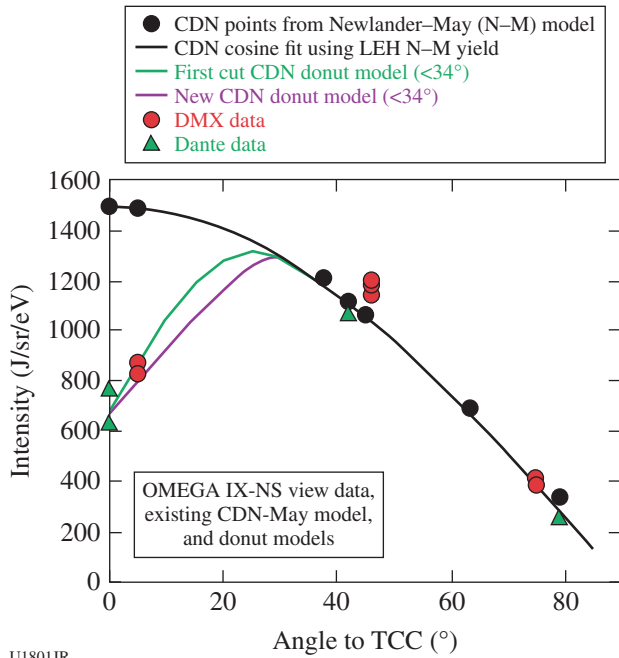
model with the data. Future work will measure x-ray emission for intermediate angles to better constrain the model and investigate other types of targets.

Optimizing X-ray Emission from Nanostructured Copper-Doped Foams

Principal Investigator: F. Pérez (LLNL)

Co-investigators: J. D. Colvin, K. B. Fournier, M. J. May, S. O. Kucheyev, and S. Charnvanichborikarn (LLNL); and T. E. Felter (Sandia)

In FY13 the X-Ray Source Development team, funded by the Defense Threat Reduction Agency, began a study of the x-ray emission from laser-irradiated Cu-doped foams. The goal is to generate bright, nanosecond-class x-ray pulses



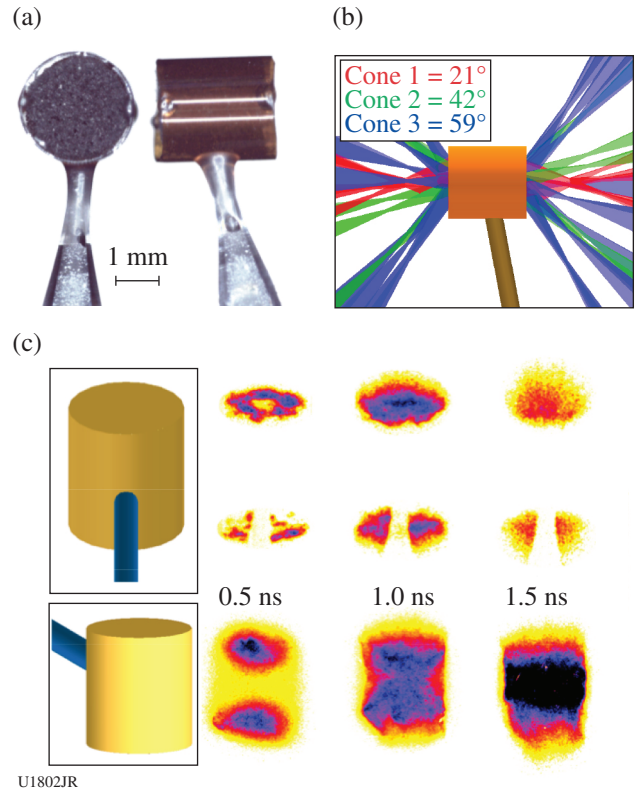
U1801JR

Figure 140.119 Dante and DMX total x-ray yield as a function of view angle, compared to the developed model.

with ~9-keV photon energies. A novel fabrication technique successfully produced Cu-doped carbon foams with densities below 50 mg/cm³ for FY13 shots. In 2014 this effort continued, developing another novel foam-fabrication method and yielding, for the first time, doped foam densities below 10 mg/cm³.

These C/Cu foams [Fig. 140.120(a)] were irradiated by 40 beams of the OMEGA laser to generate x rays [Fig. 140.120(b)]. Various foams, with densities ranging from 5 to 50 mg/cm³, were shot on two campaigns. Measurements of the x-ray yield show that the optimal density is close to 10 mg/cm³, where the conversion efficiency from laser energy into Cu K-shell x-ray energy reaches 0.8%. The dynamics of the laser-foam interaction were also investigated using framing and streak cameras, revealing that the low-density foams are heated over a much larger volume [Fig. 140.120(c)]. X-ray spectra also provided information on the plasma temperature. These measurements are currently being used as a simulation benchmark, with the wide range of densities providing tight constraints.

In FY14 this research also led to pure-Cu foams under 20 mg/cm³, which will be fielded in FY15 experiments.



U1802JR

Figure 140.120 (a) Foam sample held in a plastic tube; (b) laser irradiation pattern of the OMEGA laser; (c) x-ray emission images at different times relative to the beginning of the irradiation. The top and bottom rows correspond to foams of 50- and 8-mg/cm³ density, respectively.

This type of material has never been fabricated before and is expected to achieve even higher x-ray yield.

ACKNOWLEDGMENT

This work was performed under the auspices of the U.S. Department of Energy by Lawrence Livermore National Laboratory under Contract DE-AC52-07NA27344.

FY14 LANL Experimental Campaigns

In FY14, LANL scientists conducted 218 target shots at the Omega Laser Facility including 206 shots on OMEGA and 12 on OMEGA EP. The ICF program accounted for 40 of these shots and the HED program accounted for 174.

Shear

The Los Alamos National Laboratory (LANL) Shear Campaign is examining instability growth and its transition to turbulence relevant to mix in ICF capsules. An experimental platform was developed with antisymmetric flows about a shear

interface to examine the Kelvin–Helmholtz (KH) instability growth. The platform consists of a directly driven shock-tube target with an internal physics package consisting of two hemi-cylindrical foams separated by a layer of tracer material (Fig. 140.121). Gold plugs are situated on opposing ends of the foams to limit shock propagation from the direct drive to only one end of the foam; this sets up a pair of pressure-balanced counter-propagating shocks about the tracer layer. Measurements of the tracer layer (shear interface) mixing dynamics are used to benchmark the LANL Besnard–Harlow–Rauenzhan (BHR) turbulence model.⁶⁰ The mixing dynamics are characterized by measuring the mix width of the layer as well as examining multidimensional structure growth along the layer surface.

The FY14 Shear Campaign focused on examining the model's initial condition parameter space by varying the characteristics of the target's tracer layer. In November 2013 the Shear Campaign completed a set of experiments varying the tracer material and thickness, using 12- μm and 20- μm Ti tracer foils as opposed to the 20- μm Al tracer foils used in previous years. In May 2014 the Shear Campaign completed a two-day platform test of streaked imaging for measuring the mixing width of the tracer layer, demonstrating that streaked imaging could be a viable alternative to radiography. The May 2014 experiments were also a successful test for using a controlled increase in the tracer layer's surface roughness as another avenue for changing the mixing/instability initial conditions (see Fig. 140.122). Experiments with enhanced

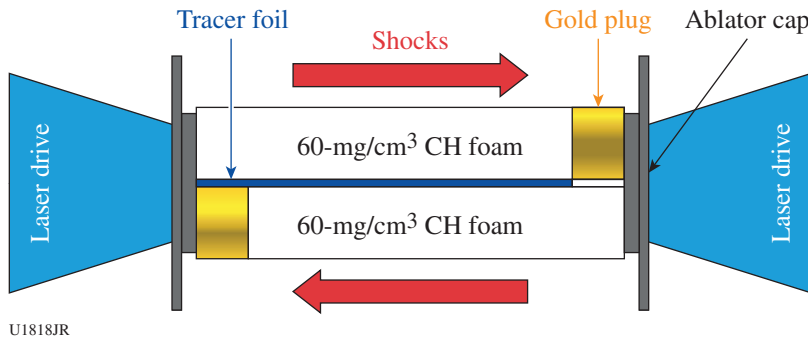


Figure 140.121
Schematic of counter-propagating shear experiment.

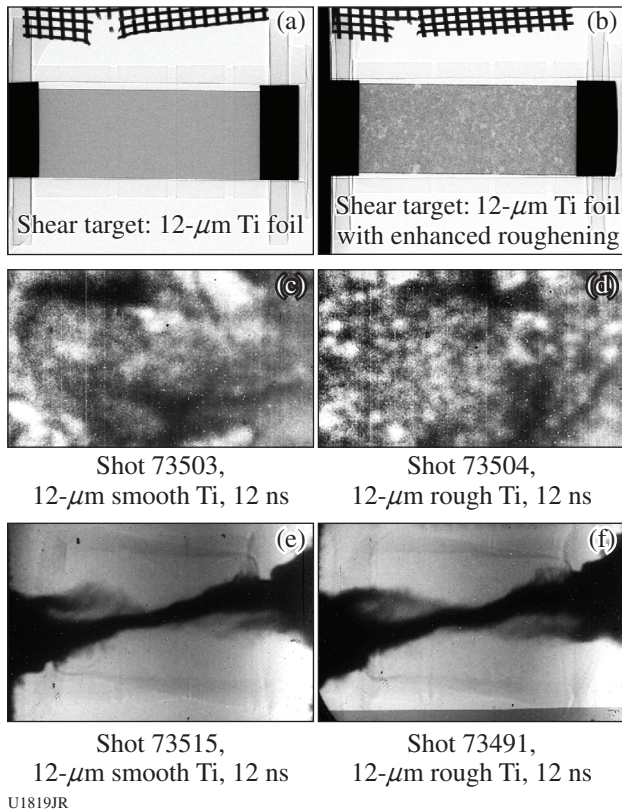


Figure 140.122
X-ray radiographs of edge-on and plan-view shear experiment for smooth and enhanced surface roughness foils.

roughened foils have shown a qualitative difference in early-time tracer-layer surface structures compared to previous experiments. Preliminary analysis also suggests that greater surface roughness can be used to alter the growth rate of the tracer layer.

CoaxDiff

The Coaxial Diffusion Experimental Campaign on the OMEGA laser is a radiation transport experiment specifically designed to challenge the implementation of implicit Monte Carlo (IMC) radiation transport techniques in radiation-hydrodynamics simulations. A gold half-hohlraum is driven with 20 OMEGA laser beams to generate x rays that interact with a low-density SiO₂ foam. The x-ray drive from the hohlraum is modified using filtration and apertures to move the physics of the radiation transport through the foam into a regime that requires the use of IMC radiation transport.

In FY14, the coaxial diffusion platform demonstrated the ability to radiograph the hydrodynamic response to the Marshak wave (heat front) when it transitioned from super- to subsonic. This gives a measure of the total energy deposited into the foam as well as information on the anisotropy of the radiation source. Experiments were also performed that

demonstrated a new technique to introduce a localized Ti dopant into the foam for absorption spectroscopy measurements (Fig. 140.123) without impacting the overall radiation transport of the experiment. This was achieved by fabricating a Ti-doped SiO₂ foam and inserting it into our standard SiO₂ foam.

WDFeos

In FY14 we built on recent results of equation-of-state (EOS) measurements of shocked silica (SiO₂) aerogel foam at the Omega Laser Facility, which used the velocity interferometer system for any reflector (VISAR) diagnostic to obtain shock-velocity measurement in the foam and a streaked optical pyrometer (SOP) to measure temperature in the shock front. Foams are important low-density pressure standards used in many high-energy-density experiments, including the novel technique of shock and release, and are also used in radiation transport and hydrodynamic instability experiments. Because of their many applications, foams are heavily studied materials and have a well-known Hugoniot curve. This work complements the velocity and pressure measurements with additional independent temperature data providing the full EOS information within the warm-dense-matter regime for the temperature interval of 1 to 15 eV and shock velocities between 10 and 40 km/s, corresponding to shock pressures of

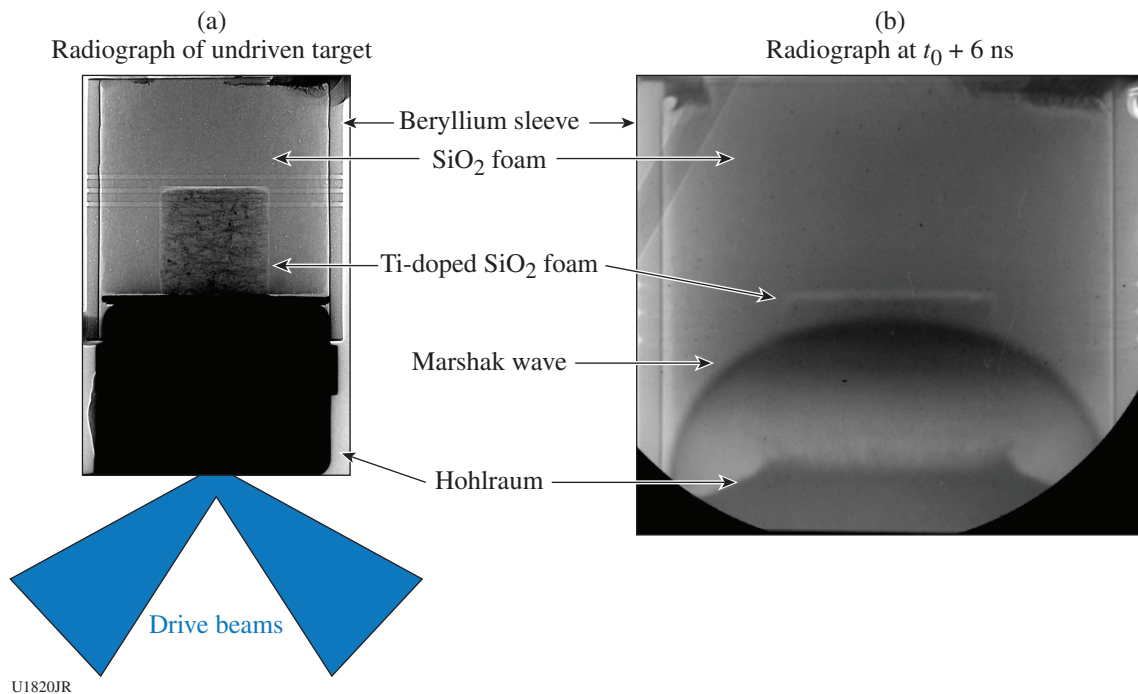


Figure 140.123

(a) A static radiograph of an undriven target using a nested Ti-doped foam for absorption spectroscopy. (b) An x-ray radiograph of the driven target 6 ns after the 1-ns-long hohlraum drive shows a well-developed Marshak wave without discontinuities at the SiO₂/Ti-doped SiO₂ foam interface. This indicates that the titanium dopant has been introduced in a way that is noninvasive to the overall radiation transport of the problem.

0.3 to 2 Mbar. The experimental results were compared with hydrodynamic simulations and EOS models. We found that the measured temperature was systematically lower than suggested by theoretical calculations. Simulations provide a possible explanation that the emission measured by optical pyrometry comes from a radiative precursor rather than from the shock front, which could have important implications for such measurements. Our previous findings were summarized in Ref. 61.

Consequently, in the latest experiments we used imaging x-ray scattering to directly measure the temperature in the shocked aerogel without relying on self-emission that appears to come from the precursor plasma, not from the bulk of the plasma within the shock wave. In FY14 we focused on CH foams at 0.15 g/cm^3 , which are not transparent like silica aerogel. The target designs are shown in Fig. 140.124. VISAR and SOP diagnostics are used to obtain shock velocity from breakout timing in a stepped foam sample. A shock wave is driven by laser ablation in

the planar-layered targets using 14 OMEGA beams (1-ns square pulse) stacked to give 2-ns drive at high intensity (450 J/beam) and low intensity (300 J/beam). An additional ten OMEGA beams were used to create a Ni He $_{\alpha}$ x-ray line at 7.8 keV by irradiating a Ni foil at ~ 2 to $3 \times 10^{15} \text{ W/cm}^2$, which was used to probe the conditions with x-ray scattering. The scattered signals were measured by the imaging x-ray Thomson spectrometer (IXTS). We obtained excellent VISAR and SOP data, which provided us with consistent shock-velocity measurements (see Fig. 140.125). We also obtained our first x-ray scattering data from the low-density CH foams. The scattering spectra were clear and the signal-to-noise ratio was excellent; however, we found that the quartz pusher was mixing into the field of view of the IXTS diagnostic, causing contamination of the scattering signal (see Fig. 140.126). Based on radiation-hydrodynamics simulations, we have redesigned the scattering targets to use a thicker Al pusher that should minimize this contamination and provide us with scattering data that simplifies the analysis.

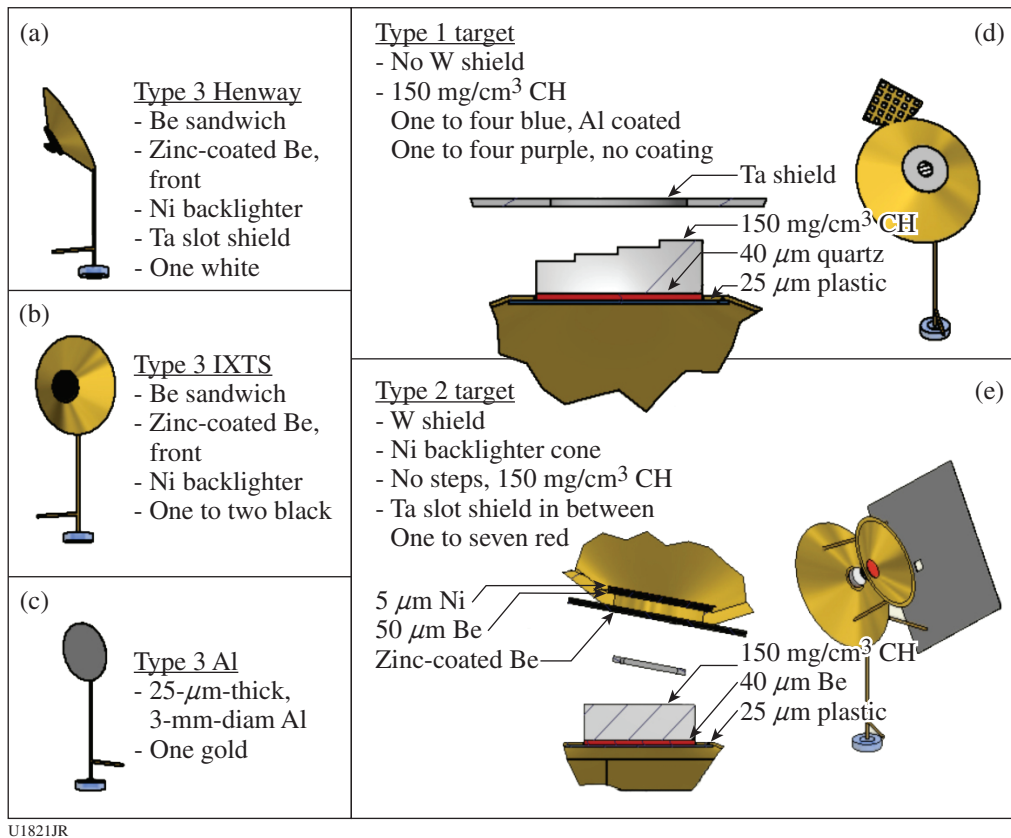


Figure 140.124
 Schematic images of the targets. Each target consisted of a 25- μm -thick plastic ablator, a 40- μm quartz pusher, and 0.15 g/cm^3 of CH foam (in the VISAR/SOP targets there were four 40- μm -thick steps on the back of the foam).

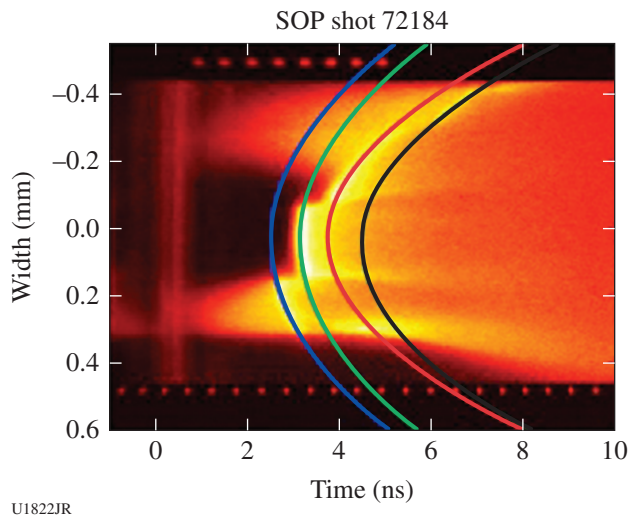


Figure 140.125 Example of the shock breakout measurement across four steps on the back of the foam target using the SOP diagnostic. Parabolic profiles are fit to each step to estimate the timing between the breakout for each step to measure the shock velocity.

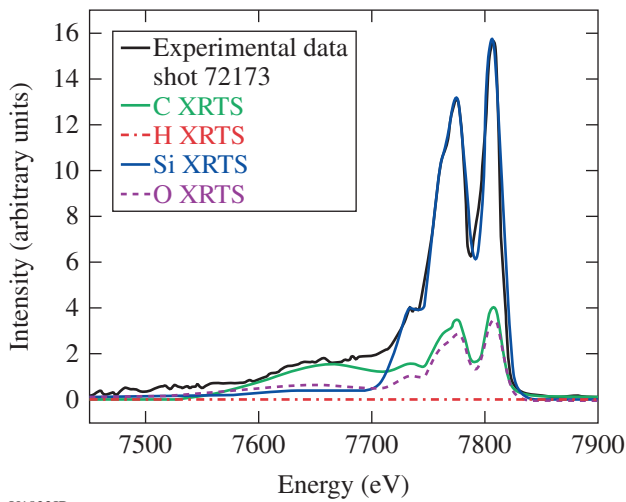


Figure 140.126 Example of x-ray scattering data from shocked CH foam. These datasets suffer from significant contamination scattering from the quartz pusher, which will be mitigated by using a thicker Al pusher for FY15 experiments.

ObliShockEP

The ObliqueShockEP-14A experiment was a test of a new platform designed to investigate the coupling between low-mode and high-mode asymmetries at a shocked interface on the OMEGA EP laser. Single-mode, machined sinusoidal modulations were used as the high-mode asymmetry, and an angled

interface with respect to the shock front made up the low-mode asymmetry. Data were taken using the OMEGA EP spherical crystal imager (SCI), a spherical crystal designed for Cu K_{α} x rays (~ 8 keV), to radiograph the perturbed interface side-on.

This experiment successfully demonstrated the platform as a viable tool to investigate the nature of oblique shock interactions with high-mode features (Fig. 140.127). The SCI resolu-

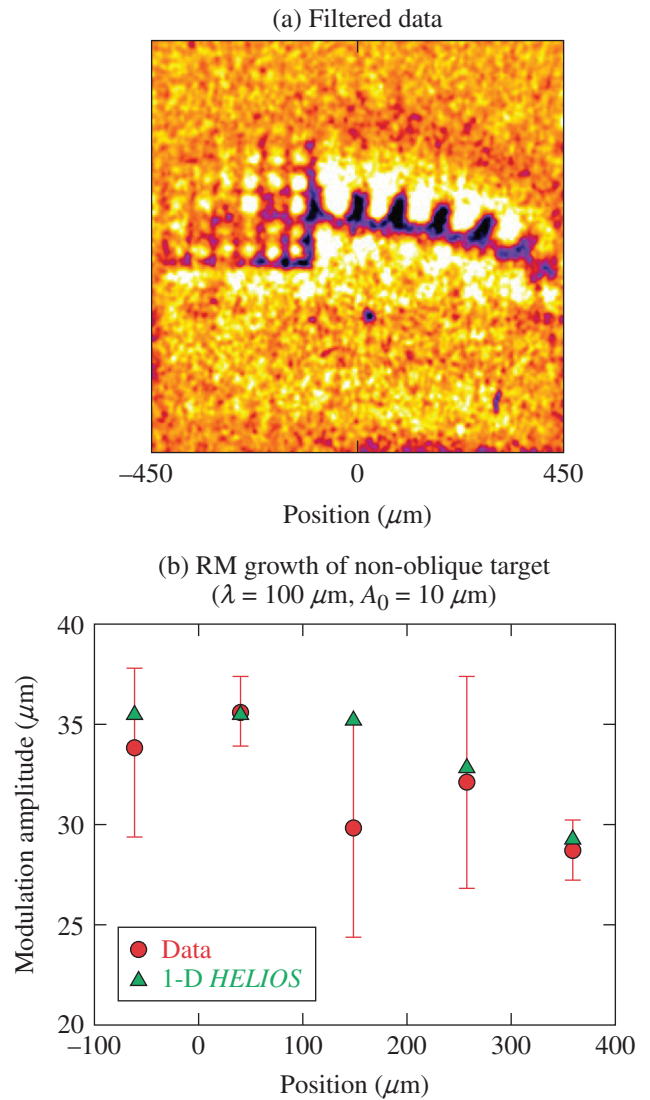


Figure 140.127 (a) Filtered data taken from a nonoblique target shows large single-mode modulations that have two amplitudes of 30 to 35 μm from an initial amplitude of 10 μm . (b) The data are overplotted with an analytic model for the classical Richtmyer–Meshkov instability using the 1-D hydrodynamics code HELIOS for the hydrodynamic parameters.

tion was $\sim 10 \mu\text{m}$, and the fluence from the backlighter was sufficient to use a low-sensitivity image plate (BAS-SR). Publication-quality data were obtained on all physics shots with the only exception being the placement of the fiducial grid overlapping with the shocked interface on some of the late-time data points.

MagLPI

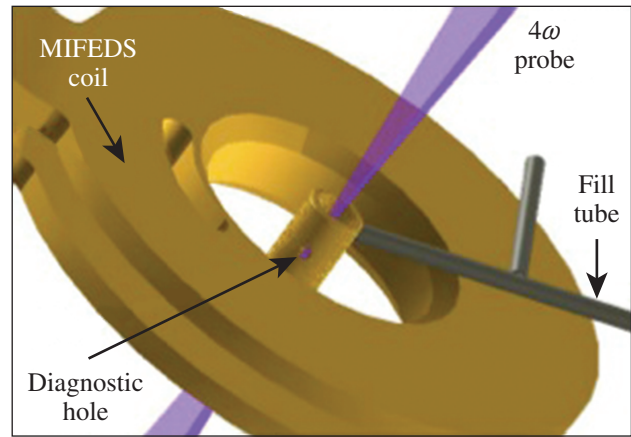
The goals of the MagLPI experiments in FY14 were to use a large external magnetic field to insulate conduction losses of the underdense plasma within a low-Z, gas-filled hohlraum and increase the plasma temperature to improve laser-plasma coupling in gas-filled hohlraum targets. Magnetic insulation is expected to occur when the electron gyroradius in the field is much smaller than the electron-ion collisional mean free path such that the gyroradius sets the step size for thermal transport. A successful demonstration of magnetic insulation may improve laser-plasma coupling in NIF ignition hohlraums.

In the OMEGA experiments, a gas-filled hohlraum was heated with 39 beams in a 1-ns pulse, and an additional 4ω probe beam measured the plasma temperatures using Thomson scattering. The 4ω probe beam propagated along the hohlraum axis. The hohlraum was 2.4 mm long and 1.6 mm in diameter with 1.2-mm-diam laser entrance holes, with 500-nm-thick polyimide windows covering the holes. A 0.4-mm-diam diagnostic hole centered in the hohlraum side was used to measure the Thomson-scattered light. The hohlraum wall was 5- μm -thick Au supported externally by 25- μm -thick epoxy. The hohlraum was filled with 1 atm of a mixture of CH_4 and C_5H_{12} gases to produce a fully ionized average electron density of $4 \times 10^{21} \text{ e/cm}^3$, and the pressure was monitored for each target up to shot time. An external B field was applied along the hohlraum axis using a Helmholtz coil driven by MIFEDS, and B fields up to 8 T were generated. A schematic of the experiment (without heater beams for simplicity) is shown in Fig. 140.128.

The time-dependent plasma temperature was measured using 4ω Thomson scattering, and the scattering profiles were fit with $\pm 100\text{-eV}$ accuracy. An increase of up to 50% in electron plasma temperature was measured with an applied field $B = 7.5 \text{ T}$. Figure 140.129 shows the measured time-dependent temperatures for an experiment with (red circles) and without (blue triangles) an external B field. Figure 140.130 shows the measured electron temperature early and late in time as a function of applied B field.

DPeOs

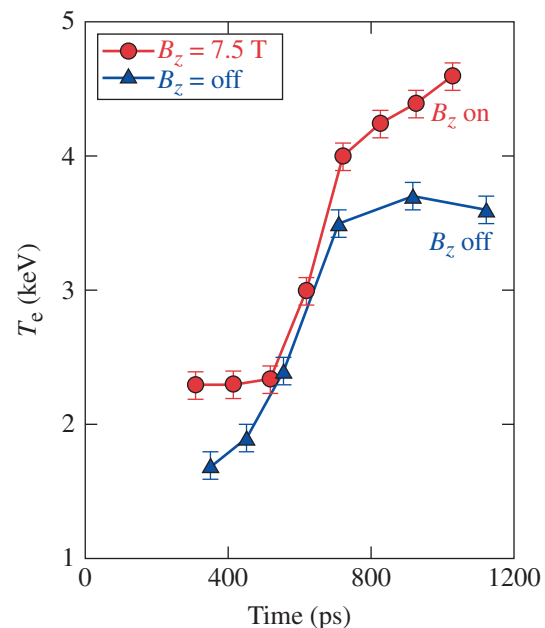
Accurate measurements and determination of the equation of state (EOS) of light elements at high pressure, solid densi-



U1825JR

Figure 140.128

Schematic of the experiment as viewed from the Thomson-scattering diagnostic. For simplicity, the heater beams are not shown.

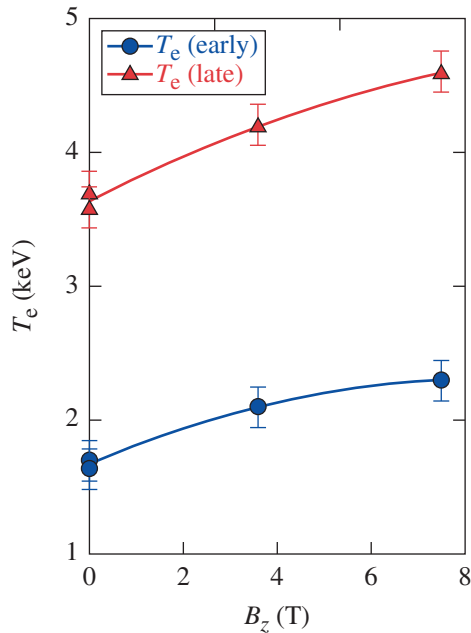


U1826JR

Figure 140.129

Plot of measured temperature versus time for an experiment with (red circles) and without (blue triangles) an external B field.

ties, and moderate temperatures (1 to 100 eV), often referred to as the warm-dense-matter (WDM) regime, are essential to understanding the structure of many astrophysical objects, including giant gaseous planets, and play an important role in the development of inertial confinement fusion (ICF). At WDM conditions, quantum degeneracy and strong interparticle coupling effects become significant and theoretical models of WDM face many challenges. Unfortunately, it is difficult to

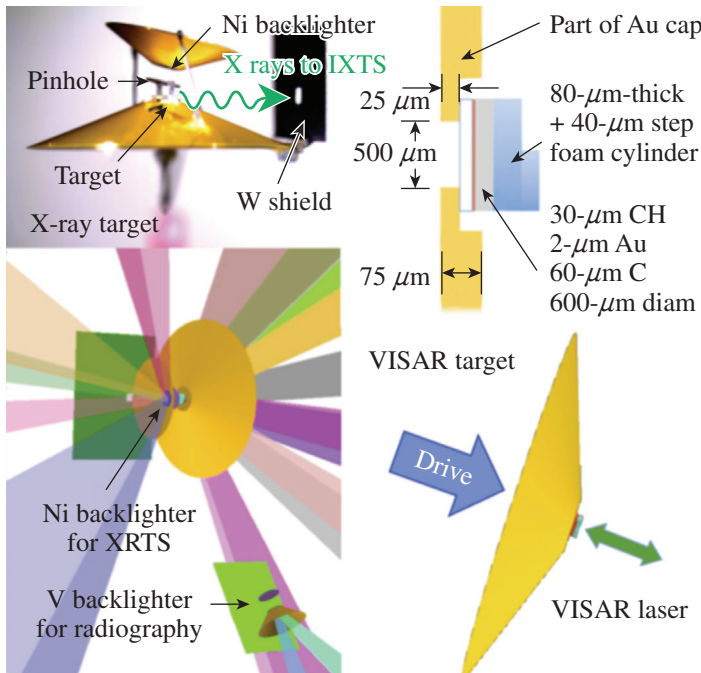


U1827JR

Figure 140.130
Plot of measured temperature versus applied B field for early time (blue) and late time (red).

obtain complete EOS information through experiments at these conditions. The goal of our project is to produce uniform dense plasma conditions in an experimental target and to measure three thermodynamic variables to determine the full EOS.

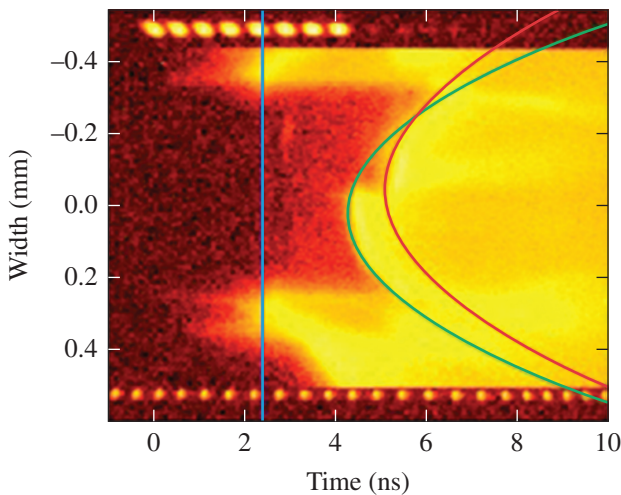
Our approach to obtaining WDM EOS data utilizes a standard shock and release technique, with two important innovations. First, the OMEGA laser was used to drive very strong (10-Mbar) initial shocks into a thin carbon or diamond foil, creating release states previously not accessed by other shock and release EOS experiments. When this shock moves through the foil and follows into a low-density, low shock impedance material (0.2-g/cm^3 silica aerogel foam), the shocked carbon sample undergoes a very deep release. This results in generating WDM conditions in the carbon, roughly solid density, and temperatures ~ 10 eV. These temperatures are far above melt or any phase transitions and are very different from the principal Hugoniot conditions typically produced in shock experiments and used to constrain EOS models like *SESAME*. Our technique, thereby, creates a useful platform for testing EOS models in this important parameter regime where no complete experimental data have been available to date (Fig. 140.131). The second key innovation is the use of x-ray Thomson scattering (XRTS) to determine the temperature of the released WDM carbon in conjunction with additional independent measurements of density and pressure using radiography and velocity interferometry (VISAR)/streaked optical pyrometry (SOP), providing us with a full EOS measurement. We succeeded, for the first time, in obtaining data on all these measurements for material at dense plasma conditions. Previous data with a Ni He_α backlighter as an x-ray-scattering probe driven by beams of 10-ns duration have been recently published (see Ref. 62).



U1828JR

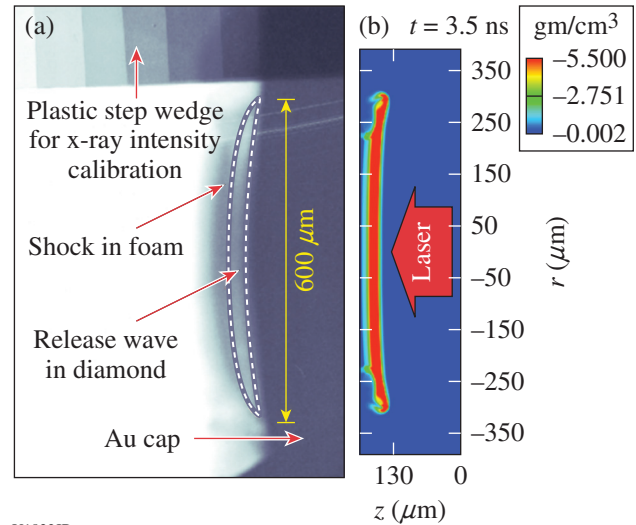
Figure 140.131
Schematic of the x-ray scattering and VISAR targets. The driven target sits inside the larger cone inside a small gold cap and consists of a plastic (CH) ablator, a graphite or diamond sample, and a silica (SiO_2) aerogel disk. The second smaller gold cones contain Ni and V backlighted foils for XRTS and radiography measurements, respectively, coated on top of a Be filter on the inner side of the cone. Laser beams then illuminate the driven target and the ablator from the inside of each Au cone. The XRTS target also includes Ta pinholes on top of each backlighter to collimate the x rays. The VISAR target is identical but has no backlighter cones or pinholes and includes a $40\text{-}\mu\text{m}$ step on the back side of the aerogel disk.

The experiments were performed on carbon at different conditions using graphite and diamond targets driven by either a low laser drive at a total intensity of 5×10^{14} W/cm² and a duration of 4 ns or a 2-ns (high) drive of 1.5×10^{15} W/cm². The targets consisted of planar layers of a plastic ablator, Au radiation shield, the carbon sample (diamond or graphite), and a thick layer of silica aerogel foam, which acted as a low-density release material. The strong shock first travels through the carbon layer and later releases into the foam, while a release wave travels back through the carbon layer, creating the desired WDM conditions. The radiographic measurement using the 5.2-keV-V-He α line was used to obtain a direct mass-density measurement through transmission. The temperature measurement was obtained from noncollective x-ray Thomson scattering using the IXTS diagnostic. Previously we used ten OMEGA beams to create Ni He α x rays at 7.8 keV, but in 2014 we began developing a new platform for utilizing a Cu K α x-ray source to be driven by the OMEGA EP beam conveyed into the OMEGA target chamber. We experienced issues with a strong electromagnetic pulse (EMP) that impaired the charge-coupled-device (CCD) camera in the IXTS diagnostic. We are currently redesigning the diagnostic to use image plates for our FY15 joint OMEGA EP shots. We managed, however, to get some additional scattering data using the old configuration with a Ni backlighter. In 2014 we obtained valuable VISAR, SOP, and radiography data as well (Figs. 140.132–140.134). We also measured an excellent flat-field spectrum that characterized the crystal nonuniformity in the IXTS diagnostic and provided an intensity correction for

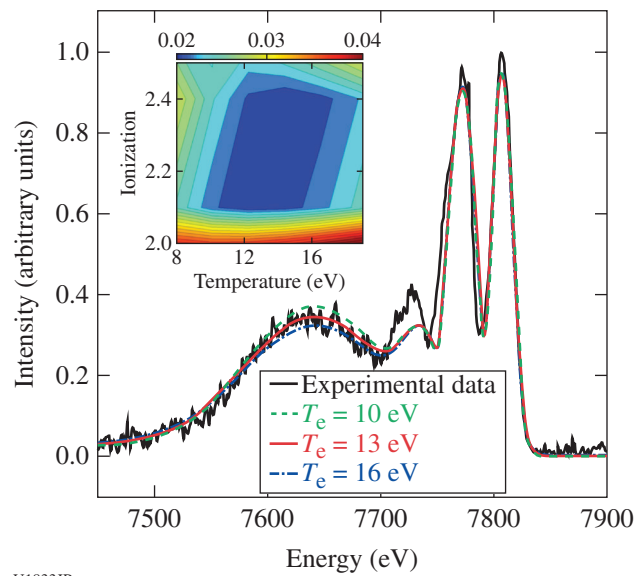


U1831JR
 Figure 140.132
 An example of shock breakout measurement using the SOP diagnostic. The shock breakout is used to measure shock velocity in the foam, which provides the release pressure in carbon.

measured x-ray spectra. The release pressure was obtained from a VISAR/SOP measurement of the velocity in the aerogel using the EOS relationship from *SESAME* Table 7387, which was confirmed by direct measurements by Knudson and Lemke.⁶³



U1832JR
 Figure 140.133
 An example radiography image of released diamond showing transmitted intensity (a) compared to a mass density plot from 2-D *FLASH* simulation. (b) The 2-D simulations confirm that the transverse effects in warm-dense-matter (WDM) conditions within the release wave are negligible.

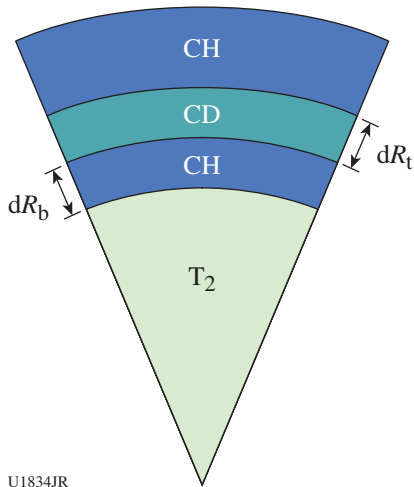


U1833JR
 Figure 140.134
 X-ray scattering data from shock-released diamond at high drive using the Ni He α x-ray source. The best-fit conditions were $T_e = 13 \pm 2$ eV, $n_e = 2.6 \pm 0.2 \times 10^{23}$ cm⁻³, and $Z = 2.0$ to 2.5 . The error bars were determined by a χ^2 fit (inserted image).

CDTMixCap

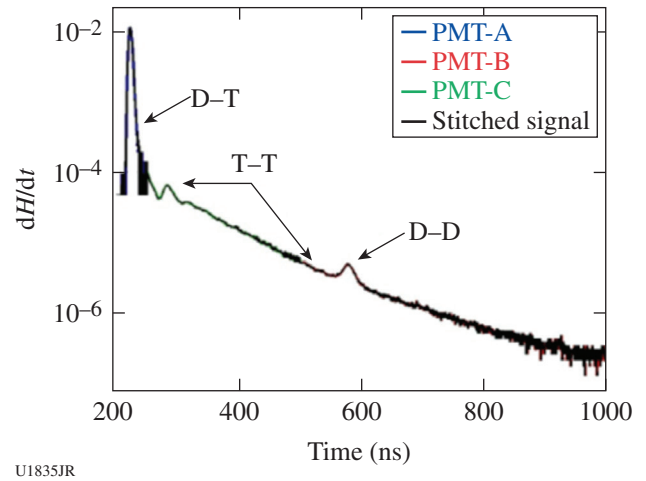
One of the challenges for developers of radiation–hydrodynamics codes is the proper calculation of burn in turbulent mixing fluids. In 2011, LANL embarked on a three-year program of study to validate turbulent models implemented in LANL’s Eulerian Applications Project code suite under the conditions of a reacting plasma. On 3 April 2014 at the Omega Laser Facility, a LANL team successfully executed a day of direct-drive implosions of 865- μm -diam plastic shells filled with pure tritium. As shown in Fig. 140.135, the plastic shells were manufactured with 1- μm -thick (dR_t) deuterated plastic layers, positioned on the inner surface of the capsule, as well as 1 and 2 μm from the inner surface (dR_b). In these implosions, deuterium–tritium fusion reactions provide a diagnostic for burn and mix.

Nuclear data collected from the implosions included fusion yields from D–D, D–T, and D–T reactions, TT ion temperatures, and gamma and neutron bang times. These data are being used to validate cutting-edge burn physics models being implemented in LANL’s Eulerian Applications Project (EAP) code suite. Figure 140.136 shows an example neutron spectrum collected from the data set. The spectrum shows clear evidence of T–T fusions from the hot gas core, D–T fusions from the atomically mixed gas-shell region, and D–D fusions from plastic chunks in the gas-shell mix volume—an experimental first! Simulations of these data and validation of the turbulent mix models in the EAP code suite are currently still ongoing.



U1834JR

Figure 140.135
Pie diagram of capsules used to validate LANL’s Besnard–Harlow–Rauenzhan (BHR) mix model implemented in the Eulerian Applications Project code suite.

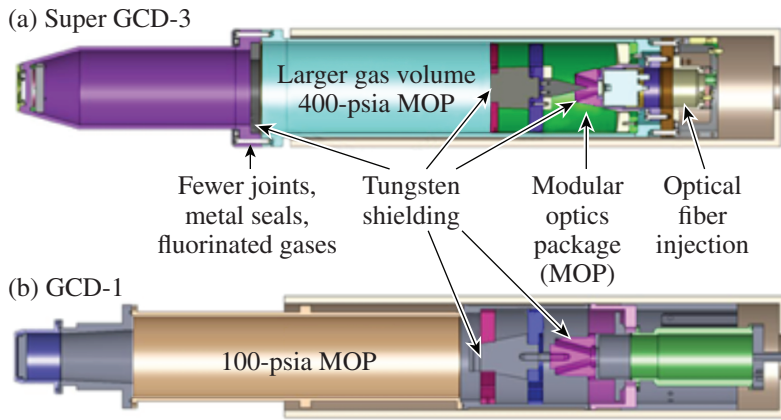


U1835JR

Figure 140.136
Neutron spectrum from a CDT Mixcap shot with 1 μm of CD on the inside of the shell. Clear evidence of D–T, T–T, and D–D fusion reactions is present in the spectra.

Gas Cherenkov Detector 3 (GCD-3)

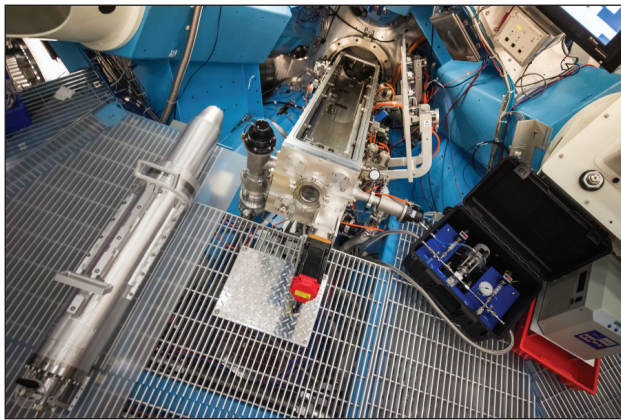
In collaboration with LLE, LANL scientists and engineers have designed, constructed, and implemented a new gas Cherenkov detector (GCD-3) on OMEGA, opening a new window to inertial confinement fusion (ICF) gamma-ray spectroscopy. GCD-3 (Figs. 140.137 and 140.138) was funded by the National Nuclear Security Administration ICF Program (LANL C-10). GCD’s operate by converting MeV gammas to UV/visible Cherenkov photons for easy detection. They provide a variable energy thresholding based on the pressure and temperature of the Cherenkov conversion gas. Previously two ten-inch manipulator–based GCD’s were fielded on OMEGA, both limited to 100 psia of CO₂, providing a >6.3-MeV energy threshold. These GCD’s were primarily designed to measure DT fusion gammas at 16.75 MeV to provide a fusion reaction history. An additional GCD-type detector, known as gamma reaction history (GRH), operates outside the OMEGA target chamber, restricting sensitivity, and is limited to operation with <215 psia of SF₆, lowering the Cherenkov conversion threshold to 2.9 MeV. In addition to reaction history, the improved lower threshold of GRH makes it possible to measure ablator areal density based on the ¹²C(n,n’) gamma at 4.44 MeV. The OMEGA GRH acted as the prototype for the four-gas cell GRH-6m, which has been in operation at the National Ignition Facility (NIF) since 2010. The new GCD-3 fulfills the need for greater sensitivity and lower threshold than afforded by the existing detectors. This was achieved by designing GCD-3 to operate inside the target chamber with high-pressure fluorinated gases. It can be safely pressurized up to 400 psia and uses all metal seals



E23465JR

Figure 140.137

CAD model depicting differences between the super gas Cherenkov detector (GCD-3) and GCD-1. Each gas cell is ~1 m long.



E23466JR

Figure 140.138

GCD-3 pressure vessel prior to insertion in an OMEGA ten-inch manipulator (TIM). GCD-3 is capable of being pressurized to 400 psia, providing Cherenkov thresholds as low as 1.8 MeV.

to virtually eliminate leakage into the target chamber. With this instrument, the energy threshold can be as low as 1.8 MeV, opening a new portion of the gamma-ray spectrum to investigation. Its first use was in collaboration with MIT to measure the cross section for H–D fusion [$H + D \rightarrow {}^3\text{He} + \gamma(5.5 \text{ MeV})$], an important step in big-bang nucleosynthesis, brown dwarfs, protostars, and the solar proton–proton fusion chain. It performed as expected with CO_2 at 400 psia, successfully measuring H–D gammas for the first time in an ICF experiment. It was also used at the end of August 2014 to compare gamma emission of samples of ${}^{12}\text{C}$ and ${}^{13}\text{C}$ under 14-MeV neutron exposure as part of a feasibility study for time-dependent “dark-mix” studies on the NIF.

HED-MMI

While deficiencies in modeling of fuel–shell mixing have been suggested to play a role in the under-predicted performance in ICF, we have primarily relied on integrated measurements to test this understanding. In this work our goal is to more severely

constrain this modeling via spectroscopic imaging [multiple-monochromatic imager (MMI)] of a Ti tracer layer. The dopant is incorporated into the plastic shell adjacent to the fuel interface.

As an example of the importance of imaging data, we note the integrated time-resolved spectroscopy in our experiments. These data clearly indicate that the Ti accesses a higher temperature than predicted from 1-D simulation, consistent with fuel–shell mixing. This information does not provide, however, a direct measure of the extent of mixing. The near-bang-time MMI images from 7 August 2014 show two principal features: (1) a broadened emission limb (as predicted) with a much-reduced contrast, and (2) an elliptical outer shape with an axis ratio of 1.3 to 1.4 from one of the two views. Analysis of the limb broadening/contrast is ongoing but we note here that little variation was observed in this aspect across thicknesses ranging from 16 to 21 μm . This insensitivity suggests that the ablative Rayleigh–Taylor does not vary this observable, so the

first FY15 shot day will explore the dependence on fill pressure (related to deceleration-phase Rayleigh–Taylor instability). For the low-mode asymmetry, this feature is observed to persist across all the targets and show no alignment with the target stalk. The ellipticity is also observed both in an undoped target and from the GMXI imager at a view angle 140° from the MMI. Surprisingly, the fluence distribution on target (hard sphere assumption with area corrections from F. Marshall) suggests the larger low-mode drive imbalance ($\sim \pm 2\%$) from the perspective showing the more-symmetric contour (see Fig. 140.139). This may suggest inaccuracies in the drive characterization or a breakdown in the interpretation of the 3-D implosion within 2-D frameworks. An indication of an understanding of the drive will be obtained in the FY15 experiments that will correct beam energies for the measured area variations.

FY14 CEA Experiments at the Omega Laser Facility

During FY14 CEA-led teams conducted 67 target shots on the OMEGA laser for several experiments. A brief summary of some of this work is included in this section.

Wall Motion

The objective of the wall motion experiment performed on 18 June 2014 was to characterize the interaction that occurs between the laser beams and the expanded plasma from the hohlraum walls and, more precisely, in the rugby-shaped cavity. The expansion of the gold plasma wall produced by the external laser cone can indeed modify the propagation of laser beams of an internal cone and then directly affect the implosion of the imploded microsphere.

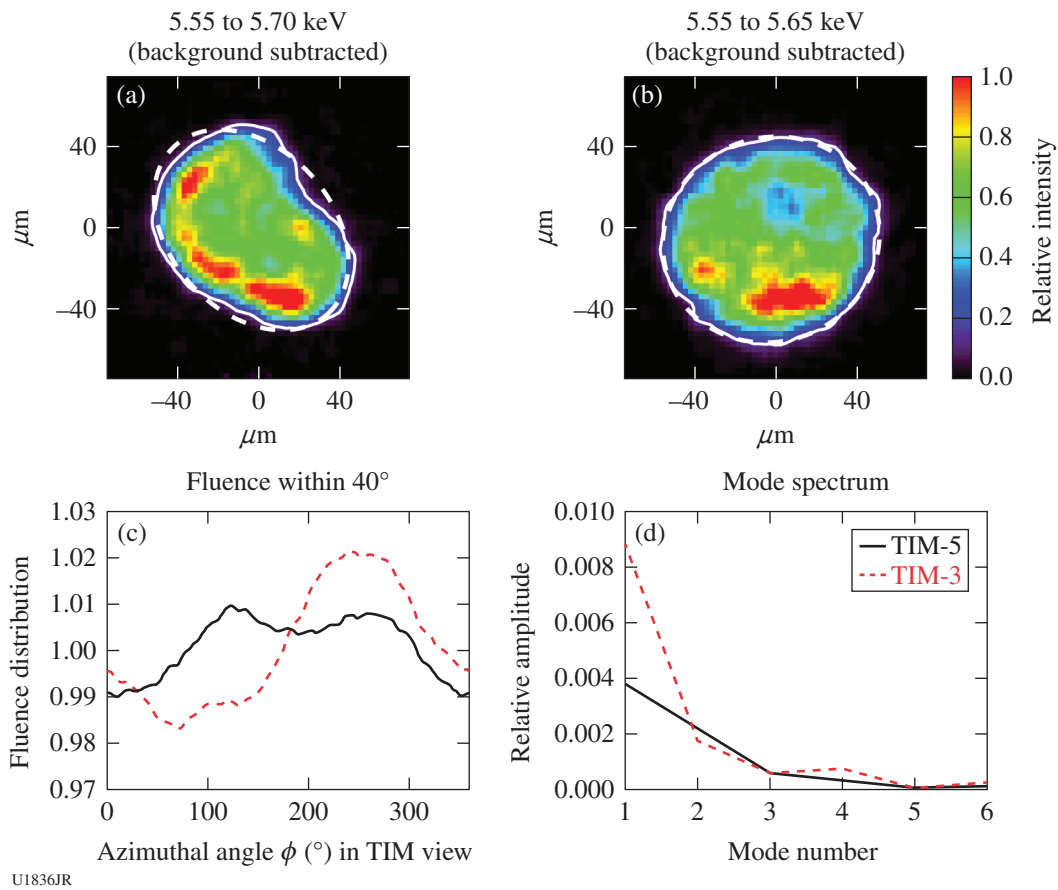
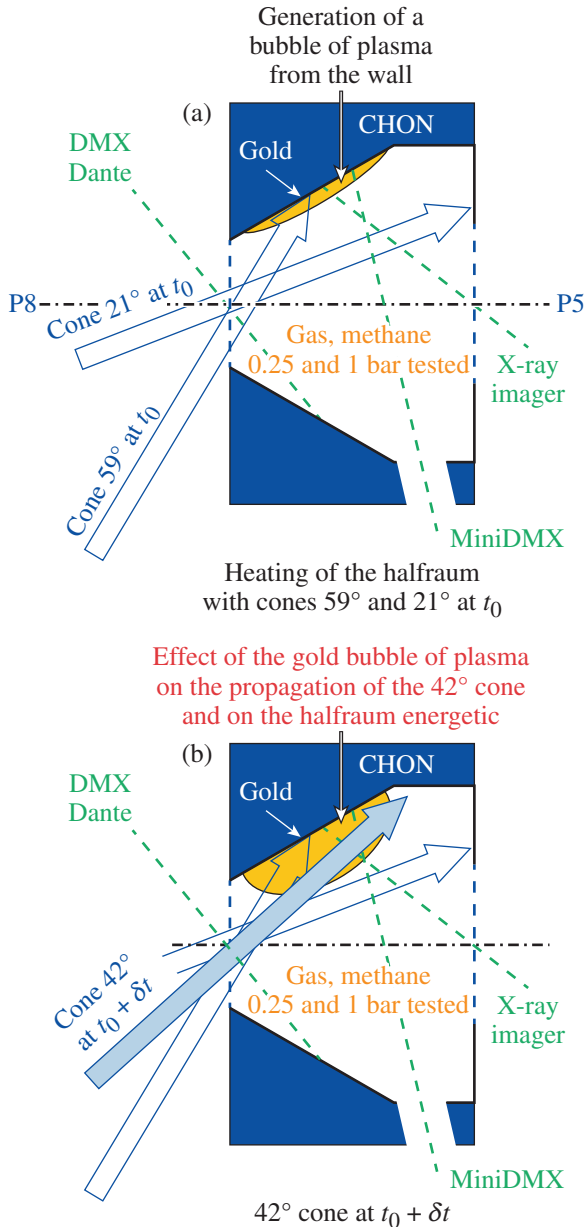


Figure 140.139

HED-MMI images and laser drive characteristics: (a) Narrowband Ti He_β image obtained from TIM-5 at ~ 100 ps prior to nuclear bang time. (b) Image obtained (same shot, same approximate timing) from TIM-3. The gross features of the implosion symmetry are typical of all targets shot for the day. (c) Equatorial fluence distribution with coordinates defined such that the pole ($\theta = 0$) is aligned toward the viewing position. (d) Modal composition of the equatorial fluence distribution.

This experiment on OMEGA was performed with a halfraum (a double-wall design with one wall tilted by 30° relative to the second wall) filled with methane (see Fig. 140.140). At t_0 , laser beams from the 21° and 59° cones (heating beams) were focused inside the target. The 59° cone was located near the point where the production of the plasma bubbles (in which we are interested) originated. At $t_0 + \delta t$, laser beams from the 42° cone were focused inside the halfraum and propagated through the plasma bubbles, which were more or less expanded, depending on the time delay δt .

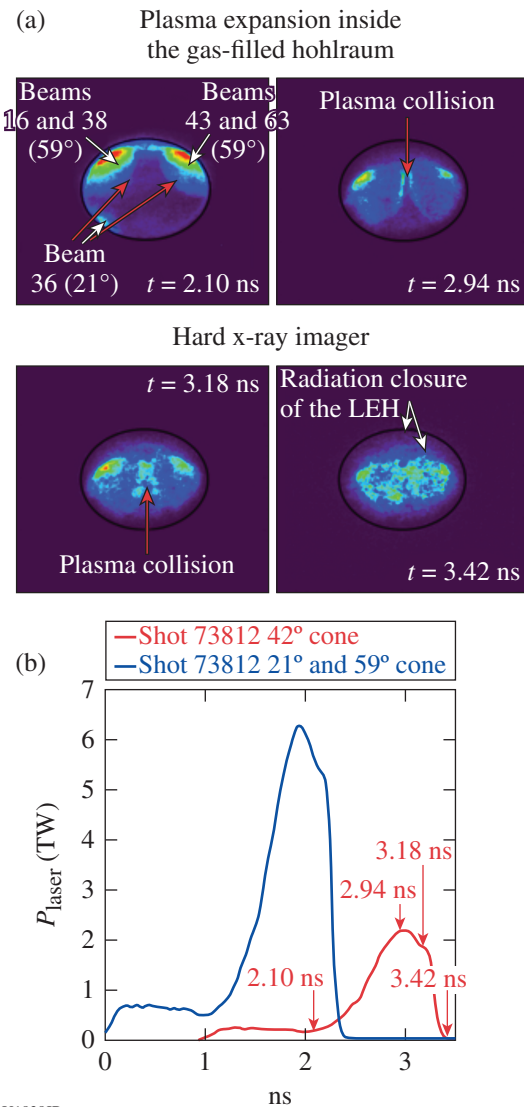


U1837JR

Figure 140.140
Principle of the experiment.

On the opposite side of the laser entrance hole (LEH), a window in the halfraum gives direct access to the plasma bubbles. In configuration “P8” represented in Fig. 140.140, plasma expansion was studied using an x-ray imager positioned in TIM-5. In configuration P5, the target was turned by 180°, and the plasma bubbles were studied using the broadband x-ray spectrometers DMX and Dante.

The x-ray imager in TIM-5 in the P5 configuration gives access to the expansion of the plasma wall produced by the 59°-cone laser beams. Figure 140.141 shows an example of



U1838JR

Figure 140.141
Images obtained with the hard x-ray imager in TIM-5 (P5 configuration).
LEH: laser entrance hole.

images obtained with $\delta t = 1$ ns and a gas pressure $P = 1$ bar, where the collision of two plasmas can be seen.

In the P8 configuration, the hard x-ray imager in TIM-5 can view the laser beams (42° and 59° cones), which impact the halfraum walls. Figure 140.142 shows experimental results obtained with $\delta t = 0.5$ ns and $P = 1$ bar. The maximum emission of the heating laser beams (59° cone) can be seen on the first image. Persistence of the signal and features could suggest a 42° -cone laser-beam energy deposition inside the plasma bubble produced by the 59° cone.

Neutron and X-Ray Imaging on the same axis on OMEGA

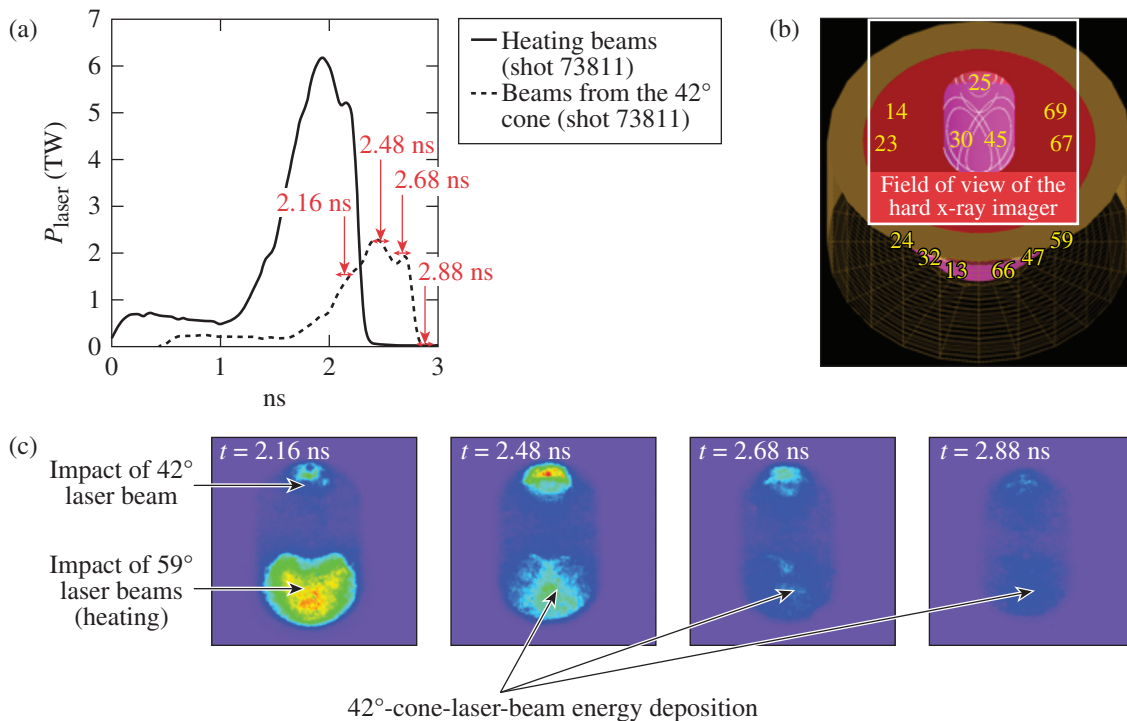
O. Landoas, T. Caillaud, S. Laffite, F. Girard, V. Tassin, and J. L. Bourgade (CEA); F. J. Marshall, V. Yu. Glebov, and T. C. Sangster (LLE)

On 9 July 2014 an experimental campaign labeled Chononmix was conducted at the Omega Laser Facility to study the mix between the target shell and the fuel during implosion. During this shot day, direct-drive implosions of D_2 , D_2 -Ar, and

DT-filled CH targets were conducted with several laser pulse shapes. The neutron yield ranged from 4×10^9 to 2×10^{10} for D–D implosions and from 10^{11} to 3×10^{12} for D–T implosions.

Among the many diagnostics activated, the neutron imaging system (NIS) was one of the main diagnostics required to acquire the core image shape. For many years, comparison between neutron and x-ray images was provided by two different diagnostics viewing the target from different target chamber ports and then integrating 3-D effects by different viewing angles. This year, we developed a system to produce neutron and x-ray images simultaneously on the same axis through the same penumbral aperture.

Over the past 15 years, we have developed the Laser Mégajoule Facility (LMJ) NIS diagnostic using a penumbral or annular coded aperture technique.^{64–68} With the NIS diagnostic, we are able to use both the small neutron imaging system's (SNIS)⁶⁹ and the large neutron imaging system's (LNIS)⁷⁰ cameras placed, respectively, at 4 and 13 m from the target.



U1839JR

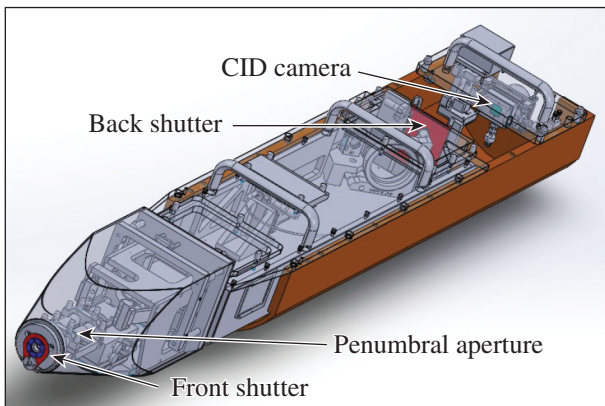
Figure 140.142 (a) Laser pulse for shot 73811 and (b) VISRAD view of the target seen from TIM-5. (c) Images obtained with the hard x-ray imager in TIM-5 (P8 configuration).

To acquire an x-ray image on the same axis as the neutron image, we set a charge-injection–device (CID) camera behind the aperture manipulator (cf., Fig. 140.143).

The CID was placed at 1.4 m from target chamber center (TCC), giving a magnification of slightly higher than 5. Several x-ray filters were set at different places to adjust x-ray transmission. A 50- μm copper filter was set in front of the CID. A 200- μm beryllium blast shield and a 100- μm aluminum filter were set on the front shutter of the aperture manipulator and a 100- μm -thick aluminum filter on the back shutter. This back shutter can be opened or closed during the shot, allowing us to adjust the x-ray transmission to optimize the signal-to-noise ratio (SNR) on the CID camera. Some preliminary results are presented in Fig. 140.144.

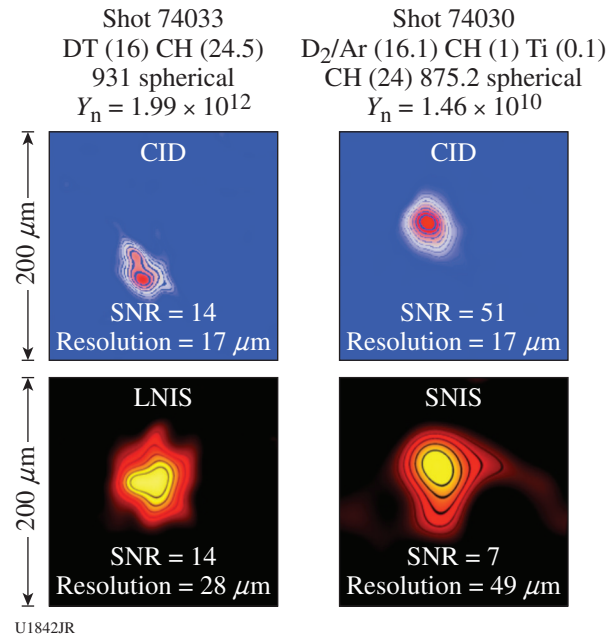
The locations of the CID, SNIS, and LNIS along the line of sight were accurately measured during alignment using a telescope as reference. Previous experiments at CEA were performed to define a referenced pixel on each detector, viewing in the same plane the front and the back of each detector. In this way, we make no hypotheses about the position of the neutron and x-ray sources using the center of the projection of the source through the penumbral aperture.

Preliminary overlaying results of neutron (SNIS) and x-ray (CID) images are presented in Fig. 140.145. The tracking accuracy of SNIS over the CID can be estimated at 15 μm in the source plan.



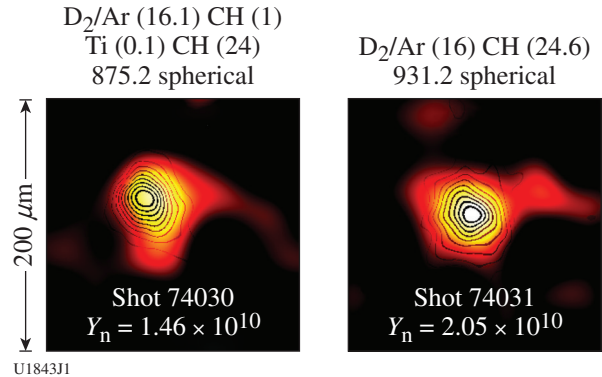
U1841JR

Figure 140.143
Aperture manipulator and CID camera on the TIM-6 line of sight.



U1842JR

Figure 140.144
X-ray and neutron images.



U1843JI

Figure 140.145
Overlaying of neutron and x-ray images for shots 74030 and 74031. X-ray images are represented as image contours at 0.2, 0.3, to 0.9 of maximum.

REFERENCES

1. W. Fox, G. Fiksel, A. Bhattacharjee, P. Y. Chang, K. Germaschewski, S. X. Hu, and P. M. Nilson, *Phys. Rev. Lett.* **111**, 225002 (2013).
2. G. Fiksel, W. Fox, A. Bhattacharjee, D. H. Barnak, P.-Y. Chang, K. Germaschewski, S. X. Hu, and P. M. Nilson, *Phys. Rev. Lett.* **113**, 105003 (2014).
3. A. S. Liao, S. Li, P. Hartigan, P. Graham, G. Fiksel, A. Frank, J. Foster, and C. Kuranz, "Numerical Simulation of an Experimental Analogue of a Planetary Magnetosphere," to be published in *High Energy Density Physics*.

4. P. Loubeyre, S. Brygoo, J. Eggert, P. M. Celliers, D. K. Spaulding, J. R. Rygg, T. R. Boehly, G. W. Collins, and R. Jeanloz, *Phys. Rev. B* **86**, 144115 (2012); J. H. Eggert, D. G. Hicks, P. M. Celliers, D. K. Bradley, R. S. McWilliams, R. Jeanloz, J. E. Miller, T. R. Boehly, and G. W. Collins, *Nat. Phys.* **6**, 40 (2010).
5. M. J. Rosenberg, H. G. Rinderknecht, N. M. Hoffman, P. A. Amendt, S. Atzeni, A. B. Zylstra, C. K. Li, F. H. Séguin, H. Sio, M. Gatu Johnson, J. A. Frenje, R. D. Petrasso, V. Yu. Glebov, C. Stoeckl, W. Seka, F. J. Marshall, J. A. Delettrez, T. C. Sangster, R. Betti, V. N. Goncharov, D. D. Meyerhofer, S. Skupsky, C. Bellei, J. Pino, S. C. Wilks, G. Kagan, K. Molvig, and A. Nikroo, *Phys. Rev. Lett.* **112**, 185001 (2014).
6. H. G. Rinderknecht, H. Sio, C. K. Li, A. B. Zylstra, M. J. Rosenberg, P. Amendt, J. Delettrez, C. Bellei, J. A. Frenje, M. Gatu Johnson, F. H. Séguin, R. D. Petrasso, R. Betti, V. Yu. Glebov, D. D. Meyerhofer, T. C. Sangster, C. Stoeckl, O. Landen, V. A. Smalyuk, S. Wilks, A. Greenwood, and A. Nikroo, *Phys. Rev. Lett.* **112**, 135001 (2014).
7. H. G. Rinderknecht, H. Sio, C. K. Li, N. Hoffman, A. B. Zylstra, M. J. Rosenberg, J. A. Frenje, M. Gatu Johnson, F. H. Séguin, R. D. Petrasso, R. Betti, V. Yu. Glebov, D. D. Meyerhofer, T. C. Sangster, W. Seka, C. Stoeckl, G. Kagan, K. Molvig, C. Bellei, P. Amendt, O. Landen, J. R. Rygg, V. A. Smalyuk, S. Wilks, A. Greenwood, and A. Nikroo, *Phys. Plasmas* **21**, 056311 (2014).
8. A. B. Zylstra, M. Gatu Johnson, J. A. Frenje, F. H. Séguin, H. G. Rinderknecht, M. J. Rosenberg, H. W. Sio, C. K. Li, R. D. Petrasso, M. McCluskey, D. Mastrosimone, V. Yu. Glebov, C. Forrest, C. Stoeckl, and T. C. Sangster, *Rev. Sci. Instrum.* **85**, 063502 (2014).
9. M. J. Rosenberg, F. H. Séguin, C. J. Waugh, H. G. Rinderknecht, D. Orozco, J. A. Frenje, M. Gatu Johnson, H. Sio, A. B. Zylstra, N. Sinenian, C. K. Li, R. D. Petrasso, V. Yu. Glebov, C. Stoeckl, M. Hohenberger, T. C. Sangster, S. LePape, A. J. Mackinnon, R. M. Bionta, O. L. Landen, R. A. Zacharias, Y. Kim, H. W. Herrmann, and J. D. Kilkenny, *Rev. Sci. Instrum.* **85**, 043302 (2014).
10. H. G. Rinderknecht, H. Sio, J. A. Frenje, J. Magoon, A. Agliata, M. Shoup, S. Ayers, C. G. Bailey, M. Gatu Johnson, A. B. Zylstra, N. Sinenian, M. J. Rosenberg, C. K. Li, F. H. Séguin, R. D. Petrasso, J. R. Rygg, J. R. Kimbrough, A. Mackinnon, P. Bell, R. Bionta, T. Clancy, R. Zacharias, A. House, T. Döppner, H. S. Park, S. LePape, O. Landen, N. Meezan, H. Robey, V. U. Glebov, M. Hohenberger, C. Stoeckl, T. C. Sangster, C. Li, J. Parat, R. Olson, J. Kline, and J. Kilkenny, *Rev. Sci. Instrum.* **85**, 11D901 (2014).
11. H. Sio *et al.*, *Rev. Sci. Instrum.* **85**, 11E119 (2014).
12. C. K. Li, D. D. Ryutov, S. X. Hu, M. J. Rosenberg, A. B. Zylstra, F. H. Séguin, J. A. Frenje, D. T. Casey, M. Gatu Johnson, M. J. E. Manuel, H. G. Rinderknecht, R. D. Petrasso, P. A. Amendt, H. S. Park, B. A. Remington, S. C. Wilks, R. Betti, D. H. Froula, J. P. Knauer, D. D. Meyerhofer, R. P. Drake, C. C. Kuranz, R. Young, and M. Koenig, *Phys. Rev. Lett.* **111**, 235003 (2013).
13. M. Rosenberg, "Studies of Ion Kinetic Effects in Shock-Driven Inertial Confinement Fusion Implosions at OMEGA and the NIF and Magnetic Reconnection Using Laser-Produced Plasmas at OMEGA," Ph.D. thesis, Massachusetts Institute of Technology, 2014.
14. C. J. Waugh, "Improved Methods for Measuring the Absolute DD Neutron Yield and Calibrating Neutron Time-of-Flight Detectors in Inertial Confinement Fusion Experiments," M.Sc. thesis, Massachusetts Institute of Technology, 2014.
15. D. Orozco, "Implementation of Scattering Pinhole Diagnostic for Detection of Fusion Products on CR-39 at High Particle Fluence," B.Sc. thesis, Massachusetts Institute of Technology, 2014.
16. M. J. Rosenberg, C. K. Li, W. Fox, I. Igumenshchev, F. H. Séguin, R. P. J. Town, J. A. Frenje, C. Stoeckl, V. Glebov, and R. D. Petrasso, "A Laboratory Study of Asymmetric Magnetic Reconnection in Strongly-Driven Plasmas," submitted to *Nature Communications*.
17. H. G. Rinderknecht, M. J. Rosenberg, C. K. Li, N. M. Hoffman, G. Kagan, A. B. Zylstra, H. Sio, J. A. Frenje, M. Gatu Johnson, F. H. Séguin, R. D. Petrasso, P. Amendt, C. Bellei, S. Wilks, J. Delettrez, V. Yu. Glebov, C. Stoeckl, T. C. Sangster, D. D. Meyerhofer, and A. Nikroo, "Ion Thermal Decoupling and Species Separation in Shock-Driven Implosions," submitted to *Physical Review Letters*.
18. M. J.-E. Manuel, "Rayleigh–Taylor-Induced Electromagnetic Fields in Laser-Produced Plasmas," Ph.D. thesis, Massachusetts Institute of Technology, 2013.
19. M. J.-E. Manuel, C. K. Li, F. H. Séguin, J. Frenje, D. T. Casey, R. D. Petrasso, S. X. Hu, R. Betti, J. D. Hager, D. D. Meyerhofer, and V. A. Smalyuk, *Phys. Rev. Lett.* **108**, 255006 (2012).
20. M. J.-E. Manuel, C. K. Li, F. H. Séguin, N. Sinenian, J. A. Frenje, D. T. Casey, R. D. Petrasso, J. D. Hager, R. Betti, S. X. Hu, J. Delettrez, and D. D. Meyerhofer, *Phys. Plasmas* **20**, 056301 (2013).
21. C. K. Li, F. H. Séguin, J. A. Frenje, J. R. Rygg, R. D. Petrasso, R. P. J. Town, P. A. Amendt, S. P. Hatchett, O. L. Landen, A. J. Mackinnon, P. K. Patel, V. A. Smalyuk, T. C. Sangster, and J. P. Knauer, *Phys. Rev. Lett.* **97**, 135003 (2006).
22. D. R. Farley *et al.*, *Phys. Rev. Lett.* **83**, 1982 (1999).
23. D. D. Ryutov *et al.*, *Phys. Plasmas* **20**, 032703 (2013).
24. P. B. Radha, T. J. B. Collins, J. A. Delettrez, Y. Elbaz, R. Epstein, V. Yu. Glebov, V. N. Goncharov, R. L. Keck, J. P. Knauer, J. A. Marozas, F. J. Marshall, R. L. McCrory, P. W. McKenty, D. D. Meyerhofer, S. P. Regan, T. C. Sangster, W. Seka, D. Shvarts, S. Skupsky, Y. Srebro, and C. Stoeckl, *Phys. Plasmas* **12**, 056307 (2005).
25. T. Bartal *et al.*, *Nat. Phys.* **8**, 139 (2012).
26. M. E. Foord *et al.*, *Phys. Plasmas* **19**, 056702 (2012); B. Qiao *et al.*, *Phys. Rev. E* **87**, 013108 (2013).
27. L. Gao, P. M. Nilson, W. Theobald, C. Stoeckl, C. Dorrer, T. C. Sangster, D. D. Meyerhofer, L. Willingale, and K. M. Krushelnick, *Bull. Am. Phys. Soc.* **55**, 377 (2010); and G. Fiksel, Laboratory for Laser Energetics, private communication (2014).
28. M. Wei, R. Mishra, S. Chawla, A. Sorokovikova, F. N. Beg, C. Chen, H. Chen, R. Fedosejevs, J. Jaquez, L. C. Jarrott, G. Kemp, M. Key, J. Kim, A. Link, H. McLean, A. Morace, V. M. Ovchinnikov, P. K. Patel, Y. Ping, B. Qiao, H. Sawada, Y. Sentoku, C. Stoeckl, W. Theobald, and R. B. Stephens, in *Proceedings of the 24th IAEA Fusion Energy Conference* (IAEA, Vienna, 2013), Paper IFE/P6–06.

29. M. Wei, "Fast Electron Generation and Transport in High Intensity Laser Solid Target Interaction Using Fast Ignition Relevant Kilojoule 10-ps OMEGA EP Laser," presented at the 13th International Workshop on the Fast Ignition of Fusion Targets, Oxford, UK, 14–18 September 2014.
30. M. S. Wei, R. Stephens, R. Mishra, A. Sorokovikova, J. Peebles, C. McGuffey, L. Jarrott, F. Beg, Y. Sentoku, H. McLean, P. Patel, and W. Theobald, *Bull. Am. Phys. Soc.* **58**, 373 (2013).
31. See Eq. (127) in G. H. Miller and T. J. Ahrens, *Rev. Mod. Phys.* **63**, 919 (1991).
32. H. Chen, S. C. Wilks, J. D. Bonlie, E. P. Liang, J. Myatt, D. F. Price, D. D. Meyerhofer, and P. Beiersdorfer, *Phys. Rev. Lett.* **102**, 105001 (2009).
33. H. Chen, S. C. Wilks, D. D. Meyerhofer, J. Bonlie, C. D. Chen, S. N. Chen, C. Courtois, L. Elberson, G. Gregori, W. Kruer, O. Landoas, J. Mithen, J. Myatt, C. D. Murphy, P. Nilson, D. Price, M. Schneider, R. Shepherd, C. Stoeckl, M. Tabak, R. Tommasini, and P. Beiersdorfer, *Phys. Rev. Lett.* **105**, 015003 (2010).
34. H. Chen, G. Fiksel, D. Barnak, P.-Y. Chang, R. F. Heeter, A. Link, and D. D. Meyerhofer, *Phys. Plasmas* **21**, 040703 (2014).
35. O. V. Gotchev, J. P. Knauer, P. Y. Chang, N. W. Jang, M. J. Shoup III, D. D. Meyerhofer, and R. Betti, *Rev. Sci. Instrum.* **80**, 043504 (2009).
36. H. Chen, D. D. Meyerhofer, S. C. Wilks, R. Cauble, F. Dollar, K. Falk, G. Gregori, A. Hazi, E. I. Moses, C. D. Murphy, J. Myatt, J. Park, J. Seely, R. Shepherd, A. Spitkovsky, C. Stoeckl, C. I. Szabo, R. Tommasini, C. Zулuck, and P. Beiersdorfer, *High Energy Density Phys.* **7**, 225 (2011).
37. P. Y. Chang, G. Fiksel, M. Hohenberger, J. P. Knauer, R. Betti, F. J. Marshall, D. D. Meyerhofer, F. H. Séguin, and R. D. Petrasso, *Phys. Rev. Lett.* **107**, 035006 (2011).
38. M. Tabak *et al.*, *Phys. Plasmas* **1**, 1626 (1994).
39. S. Ivancic, D. Haberberger, H. Habara, T. Iwawaki, K. S. Anderson, R. S. Craxton, D. H. Froula, D. D. Meyerhofer, C. Stoeckl, K. Tanaka, and W. Theobald, "Channeling Multikilojoule High-Intensity Laser Beams in an Inhomogeneous Plasma," submitted to *Physical Review Letters*.
40. D. H. Froula, R. Boni, M. Bedzyk, R. S. Craxton, F. Ehrne, S. Ivancic, R. Jungquist, M. J. Shoup, W. Theobald, D. Weiner, N. L. Kugland, and M. C. Rushford, *Rev. Sci. Instrum.* **83**, 10E523 (2012).
41. D. Haberberger, S. Ivancic, S. X. Hu, R. Boni, M. Barczys, R. S. Craxton, and D. H. Froula, *Phys. Plasmas* **21**, 056304 (2014).
42. J. Zhang *et al.*, *Phys. Rev. A* **54**, 1597 (1996).
43. R. Betti, C. D. Zhou, K. S. Anderson, L. J. Perkins, W. Theobald, and A. A. Solodov, *Phys. Rev. Lett.* **98**, 155001 (2007).
44. R. Nora, W. Theobald, F. J. Marshall, D. T. Michel, W. Seka, B. Yaakobi, M. Lafon, C. Stoeckl, J. A. Delettrez, A. A. Solodov, A. Casner, C. Reverdin, X. Ribeyre, A. Vallet, J. Peebles, F. N. Beg, M. S. Wei, and R. Betti, "Gigabar Spherical Shock Generation on the OMEGA Laser," submitted to *Physical Review Letters*.
45. G. Kagan and X.-Z. Tang, *Phys. Lett. A* **378**, 1531 (2014).
46. N. L. Kugland, D. D. Ryutov, P. Y. Chang, R. P. Drake, G. Fiksel, D. H. Froula, S. H. Glenzer, G. Gregori, M. Grosskopf, M. Koenig, Y. Kuramitsu, C. Kuranz, M. C. Levy, E. Liang, J. Meinecke, F. Miniati, T. Morita, A. Pelka, C. Plechaty, R. Presura, A. Ravasio, B. A. Remington, B. Reville, J. S. Ross, Y. Sakawa, A. Spitkovsky, H. Takabe, and H. S. Park, *Nat. Phys.* **8**, 809 (2012).
47. N. L. Kugland, J. S. Ross, P. Y. Chang, R. P. Drake, G. Fiksel, D. H. Froula, S. H. Glenzer, G. Gregori, M. Grosskopf, C. Huntington, M. Koenig, Y. Kuramitsu, C. Kuranz, M. C. Levy, E. Liang, D. Martinez, J. Meinecke, F. Miniati, T. Morita, A. Pelka, C. Plechaty, R. Presura, A. Ravasio, B. A. Remington, B. Reville, D. D. Ryutov, Y. Sakawa, A. Spitkovsky, H. Takabe, and H. S. Park, *Phys. Plasmas* **20**, 056313 (2013).
48. J. H. Nguyen and N. C. Holmes, *Nature* **427**, 339 (2004).
49. R. Briggs *et al.*, *J. Phys.: Conf. Ser.* **377**, 012035 (2012).
50. S.-N. Luo and T. J. Ahrens, *Phys. Earth Planet. Inter.* **143–144**, 369 (2004).
51. J. R. Rygg, J. H. Eggert, A. E. Lazicki, F. Coppari, J. A. Hawreliak, D. G. Hicks, R. F. Smith, C. M. Sorce, T. M. Uphaus, B. Yaakobi, and G. W. Collins, *Rev. Sci. Instrum.* **83**, 113904 (2012).
52. D. K. Bradley *et al.*, *Phys. Rev. Lett.* **102**, 075503 (2009).
53. R. F. Smith *et al.*, *Nature* **511**, 330 (2014).
54. Y. Ping, D. G. Hicks, B. Yaakobi, F. Coppari, J. Eggert, and G. W. Collins, *Rev. Sci. Instrum.* **84**, 123105 (2013).
55. J. Edwards *et al.*, *Phys. Rev. Lett.* **92**, 075002 (2004).
56. P. K. Patel *et al.*, *Phys. Rev. Lett.* **91**, 125004 (2003).
57. S. C. Wilks *et al.*, *Phys. Plasmas* **8**, 542 (2001).
58. R. F. Heeter, S. B. Hansen, K. B. Fournier, M. E. Foord, D. H. Froula, A. J. Mackinnon, M. J. May, M. B. Schneider, and B. K. F. Young, *Phys. Rev. Lett.* **99**, 195001 (2007).
59. F. Pérez, G. E. Kemp, S. P. Regan, M. A. Barrios, J. Pino, H. Scott, S. Ayers, H. Chen, J. Emig, J. D. Colvin, M. Bedzyk, M. J. Shoup, A. Agliata, B. Yaakobi, F. J. Marshall, R. A. Hamilton, J. Jaquez, M. Farrell, A. Nikroo, and K. B. Fournier, *Rev. Sci. Instrum.* **85**, 11D613 (2014).
60. D. Besnard *et al.*, Los Alamos National Laboratory, Los Alamos, NM, Report LA-12303-MS (1992).
61. K. Falk, C. A. McCoy, C. L. Fryer, C. W. Greeff, A. L. Hungerford, D. S. Montgomery, D. W. Schmidt, D. G. Sheppard, J. R. Williams, T. R. Boehly, and J. F. Benage, *Phys. Rev. E* **90**, 033107 (2014).
62. K. Falk *et al.*, *Phys. Rev. Lett.* **112**, 155003 (2014); K. Falk *et al.*, *Phys. Plasmas* **21**, 056309 (2014).

- 63. M. D. Knudson and R. W. Lemke, *J. Appl. Phys.* **114**, 053510 (2013).
- 64. L. Disdier, A. Rouyer, D. C. Wilson, A. Fedotoff, C. Stoeckl, J. L. Bourgade, V. Yu. Glebov, J.-P. Garçonnet, and W. Seka, *Nucl. Instrum. Methods Phys. Res. A* **489**, 496 (2002).
- 65. L. Disdier, A. Rouyer, A. Fedotoff, J.-L. Bourgade, F. J. Marshall, V. Yu. Glebov, and C. Stoeckl, *Rev. Sci. Instrum.* **74**, 1832 (2003).
- 66. L. Disdier, R. A. Lerche, J. L. Bourgade, and V. Yu. Glebov, *Rev. Sci. Instrum.* **75**, 2134 (2004).
- 67. A. Rouyer, *Rev. Sci. Instrum.* **74**, 1234 (2003).
- 68. L. Disdier, A. Rouyer, I. Lantuéjoul, O. Landoas, J. L. Bourgade, T. C. Sangster, V. Yu. Glebov, and R. A. Lerche, *Phys. Plasmas* **13**, 056317 (2006).
- 69. T. Caillaud, O. Landoas, M. Briat, B. Rosse, I. Thfoin, F. Philippe, A. Casner, J. L. Bourgade, L. Disdier, V. Yu. Glebov, F. J. Marshall, T. C. Sangster, H. S. Park, H. F. Robey, and P. Amendt, *Rev. Sci. Instrum.* **83**, 10E131 (2012).
- 70. T. Caillaud, O. Landoas, M. Briat, S. Kime, B. Rossé, I. Thfoin, J. L. Bourgade, L. Disdier, V. Yu. Glebov, F. J. Marshall, and T. C. Sangster, *Rev. Sci. Instrum.* **83**, 033502 (2012).

